

APPLIED PHYSICS REVIEWS—FOCUSED REVIEW

Laplace-transform deep-level spectroscopy: The technique and its applications to the study of point defects in semiconductors

L. Dobaczewski

Institute of Physics, Polish Academy of Sciences, al. Lotnikow 32/46, 02-668 Warsaw, Poland

A. R. Peaker

Centre for Electronic Materials, Devices and Nanostructures, University of Manchester Institute of Science and Technology, P.O. Box 88, Manchester M60 1QD, United Kingdom

K. Bonde Nielsen

Department of Physics and Astronomy, University of Aarhus, Ny Munkegade, DK 8000 Århus C, Denmark

(Received 6 February 2004; accepted 19 July 2004)

We present a comprehensive review of implementation and application of Laplace deep-level transient spectroscopy (LDLTS). The various approaches that have been used previously for high-resolution DLTS are outlined and a detailed description is given of the preferred LDLTS method using Tikhonov regularization. The fundamental limitations are considered in relation to signal-to-noise ratios associated with the measurement and compared with what can be achieved in practice. The experimental requirements are discussed and state of the art performance quantified. The review then considers what has been achieved in terms of measurement and understanding of deep states in semiconductors through the use of LDLTS. Examples are given of the characterization of deep levels with very similar energies and emission rates and the extent to which LDLTS can be used to separate their properties. Within this context the factors causing inhomogeneous broadening of the carrier emission rate are considered. The higher resolution achievable with LDLTS enables the technique to be used in conjunction with uniaxial stress to lift the orientational degeneracy of deep states and so reveal the symmetry and in some cases the structural identification of defects. These issues are discussed at length and a range of defect states are considered as examples of what can be achieved in terms of the study of stress alignment and splitting. Finally the application of LDLTS to alloy systems is considered and ways shown in which the local environment of defects can be quantified. © 2004 American Institute of Physics. [DOI: 10.1063/1.1794897]

TABLE OF CONTENTS

I. INTRODUCTION.....	4690	2. Dangling-bond levels.....	4698
A. Carrier capture and emission of carriers at deep states.....	4690	3. The vacancy-oxygen center.....	4699
B. Processing of emission transients.....	4691	B. Separation of capture rates.....	4700
C. Principles and limitations of deconvolution methods.....	4691	C. Minority carrier capture and emission.....	4701
II. THE IMPLEMENTATION OF LAPLACE DLTS..	4693	D. Spatial separation of defect centers.....	4701
A. Hardware and technical requirements.....	4693	E. Inhomogeneous and homogeneous broadening phenomena.....	4702
B. Deconvolution algorithms and mathematical limitations.....	4694	1. Local strain.....	4702
C. State of the art performance.....	4696	2. Electric-field effects.....	4704
III. APPLICATION TO CHARACTERIZATION OF DEEP CENTERS WITH SIMILAR EMISSION RATES.....	4696	IV. APPLICATIONS OF LAPLACE DLTS WITH UNIAXIAL STRESS.....	4705
A. Separation of levels.....	4696	A. Introduction.....	4705
1. The gold acceptor and the $G4$ gold-hydrogen complex in silicon.....	4696	B. Interpretation of stress data.....	4705
		1. General formulas.....	4705
		2. Defect symmetry from level splitting.....	4706
		3. Piezospectroscopic parameters from alignment studies.....	4707
		4. Piezospectroscopic parameters from level splitting.....	4707
		5. Stress dependence of preexponential factors.....	4708
		C. Early DLTS stress work.....	4708

^aElectronic mail: peaker@manchester.ac.uk, dobacz@ifpan.edu.pl

1. Hydrostatic pressure applications.	4708
2. Band-edge deformation potentials and absolute pressure derivatives.	4710
3. Effects of band splitting on the capture process.	4710
4. Uniaxial-stress applications.	4711
D. Uniaxial stress with Laplace DLTS.	4713
1. Defect symmetry from level splitting...bond-center hydrogen, H_{BC}	4713
2. Piezospectroscopic parameters from alignment and splitting: The VO and VOH centers.	4714
3. Dynamic properties: The H_{BC} , V_2 , VO, and VOH centers.	4716
4. Uniaxial stress and the preexponential factor: The VO center.	4719
V. ALLOY EFFECTS.	4720
A. III-V alloys: The DX centers in AlGaAs.	4720
B. Alloys of SiGe.	4722
1. Indiffused Au and Pt, the alloy splitting effect and siting preference.	4722
2. Bond-centered hydrogen: Trapping in local strain.	4724
VI. SUMMARY AND OUTLOOK.	4725

I. INTRODUCTION

Thermal emission of current carriers from defects in semiconductors has been used as a characterization technique for over 50 years. One of the most significant early publications was by Sah *et al.*¹ in which he reviewed his own and earlier work on a quantitative basis. Sah and a few other groups working in the late 1960s focused on the measurement of deep state properties within the depletion region of a p-n junction or Schottky diode. This represented a very significant advance compared to measurements on bulk or highly compensated material that had often been used in early experiments. The fundamentally important point in relation to depletion layer methods is that they provide an environment where the occupancy of the deep state can be manipulated with relative ease. In general they also have the advantage of providing much greater sensitivity than bulk methods. Sah described many techniques utilizing depletion methods and in this paper we deal exclusively with depletion measurements. Sah, and subsequently many others using thermal emission measurements to study deep states, repeatedly drew attention to the difficulty of separating the time constants of exponential emission transients from different defect states. In this paper we review the issues involved in measuring closely spaced carrier ionization energies of deep states and focus on how major advances have been made in separating thermal emission transients using a Laplace-transform method.

A. Carrier capture and emission of carriers at deep states

A deep level almost always changes its electron occupancy via carrier transitions between the level and the bands.

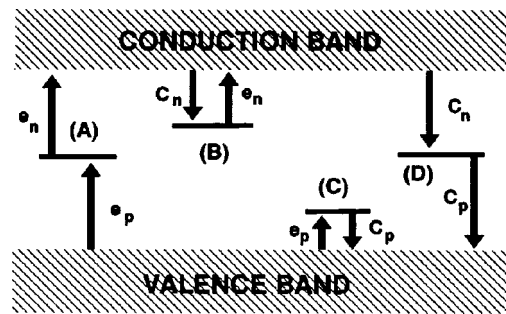


FIG. 1. Schematic representation of transitions of carriers between deep states and the valence- and conduction-band transfer between deep levels is neglected. (A) Carrier generation, (B) electron trapping, (C) hole trapping, (D) recombination. The arrows show the effective direction of electron transfer for both hole and electron process.

The four most common processes are illustrated in Fig. 1. Electron transfer between deep levels is neglected.

In relation to the measurement of deep state properties it is almost invariably the processes (B) and (C) which are used to derive deep state parameters. The arrows illustrating the various transitions in Fig. 1 show the appropriate direction of electron transfer. The kinetics of charge transfer, which are ultimately used to analyze deep-level experimental data, are described using the Schokley-Read-Hall² (SRH) model. This model is developed within a framework of thermal equilibrium (or near equilibrium). Deep-level detection experiments are generally performed by introducing perturbations to the carrier density or to the occupancy of the deep states involved and observing the return to equilibrium. Taking electron emission as an example, the electron emission rate as a function of temperature is given by

$$e_n(T) = \sigma_n \langle v_n \rangle \frac{g_0}{g_1} N_c \exp \left(- \frac{E_c - E_t}{k_B T} \right), \quad (1)$$

where $E_c - E_t$ is the energy separation of the deep state from (in this case) the conduction band. The degeneracy terms g_0 and g_1 refer to the state before and after electron emission, respectively. The parameter σ_n is the electron capture cross section which may or may not be temperature dependent as will be discussed later. In these equations the thermal velocity of electrons $\langle v_n \rangle$ and the density of conduction-band and states N_c are temperature dependent,

$$\langle v_n \rangle = \left(\frac{3k_B T}{m^*} \right)^{1/2} \quad (2)$$

and

$$N_c = 2M_c \left(\frac{2\pi m^* k_B T}{h^2} \right)^{3/2}, \quad (3)$$

where M_c is the number of conduction-band minima. The $N_c v_n$ product has a T^2 dependence therefore a plot of e_n/T^2 as a function of T^{-1} is a straight line with activation energy E_{na} and preexponential factor defined by σ_{na} if a temperature-dependent capture cross section is allowed for of the form³

$$\sigma(T) = \sigma_{\infty} \exp \left(-\frac{\Delta E_{\sigma}}{k_B T} \right) \quad (4)$$

and

$$\sigma_{na} = \frac{g_0}{g_1} \sigma_{\infty}. \quad (5)$$

Experimentally, it is found that data for most traps fit an equation of this form over many orders of magnitude of e_n , although considerable care is required in the physical interpretation of E_{na} and σ_{na} . In the formulation presented here E_{na} can be identified with $(E_c - E_t) + \Delta E_{\sigma}$. It does not give the energy level of the trap directly. Furthermore, this identification only holds if $(E_c - E_t)$ is itself temperature independent. σ_{na} is the apparent capture cross section and as derived here is identified with $(g_0/g_1)\sigma_{\infty}$; it is not equal to the directly measured capture cross section. This is an issue that is discussed at great length in the literature and often expressed in thermodynamic terms.⁴ It is a subject of importance when energies derived from thermal emission measurements are compared with other methods, for example, optical absorption or photoluminescence and increases in importance in relation to Laplace deep-level transient spectroscopy (LDLTS) due to the higher resolution available. The topic is revisited in this review in relation to uniaxial-stress measurements in Sec. IV B 1.

B. Processing of emission transients

In 1974, Lang⁵ introduced a simple form of signal processing to display the temperature-dependent emission transients from deep states. This method produced a sequence of peaks as the temperature was scanned, each of which could be interpreted as relating to an electrically active defect. This technique was named deep level transient spectroscopy (DLTS) and was, in essence, a simple analog filtering method in which a peak was produced when the emission rate matched the filter “rate window.” In general thermal emission transients from deep states are often small and superimposed on a background potential that changes slowly as the temperature is scanned. In consequence a fundamental requirement for any DLTS like system is a rejection of this background level either as an intrinsic feature of the filter or as a separate “dc restoration” step. As the emission transient signal is often quite small, sensitivity or, in reality, signal-to-noise considerations are of crucial importance.

As discussed earlier the use of depletion methods provides a dramatic increase in detectivity compared to the bulk methods of the very early investigations but beyond that there are system engineering considerations affecting detectivity (which will be discussed later) and the efficiency of filtering method chosen. The latter is a very complex issue and is central to this review. At this stage it is worth generalizing in the sense that the signal-to-noise performance of a system will degrade as the bandwidth of the filter decreases. This means that in the limit the ability to separate closely spaced transients is only likely to be achieved at the expense of sensitivity to defect concentration. The problem of separating closely spaced transients has been repeatedly identified

as the major deficiency of the DLTS technique as in most experimental cases a number of deep states are present simultaneously and sometimes these have very similar emission characteristics.

DLTS is unlike optical spectroscopy which when conducted at low temperatures can provide very sharp lines. DLTS always produces broad, relatively featureless spectra that are difficult to interpret in terms of precise energetic relationships. In reality Lang had chosen (perhaps unwittingly) a filter that has proved to be a very good compromise between energy selectivity and concentration detectivity. In consequence Lang’s work popularized deep-level measurements by eliminating the tedious graphical analysis techniques normally used by the few specialists in the field working in the 1960s and early 1970s. DLTS provided a technique that produced the form of output much appreciated by scientists, namely, a sequence of peaks which, in favorable circumstances, could be attributed to specific impurities or structural defects. The filter design (referred to as a “double boxcar”) also had the important attribute of intrinsic dc rejection so that in normal circumstances if no defect was present the filter output was zero.

The time constant resolution of conventional DLTS is too poor for studying fine structure in the emission process. The reason for this is the choice of filter rather than thermal broadening. The end result is that even a perfect defect, with no complicating factors, produces a broad line on the DLTS spectrum due to instrumental effects. Any variation of time constant present in the defect emission results in an additional broadening of the peak, so this structure is practically impossible to resolve unless the time constants are well separated. Some improvement in resolution is possible simply by changing the filter characteristic and many papers have been published on this topic and also on methods to achieve better energy resolution at the expense of detectivity.

Lang’s system generated peaks in which the area under the curve was proportional to the charge exchange, which in the simplest (and most usual) case is proportional to the defect concentration. Because, in most cases, the peak half width is primarily dependent on the filter design rather than on some physical property of the defect (other than its energy) the height of the peak rather than its area is commonly used as the parameter to measure concentration. If higher energy resolution is achieved this approximation breaks down. It then becomes necessary to determine the area under the peak rather than its height as a measure of charge exchange and hence of concentration of the defect.

C. Principles and limitations of deconvolution methods

Many approaches have been applied to try to separate exponential transients. In DLTS there have been two broad categories of methodologies, which can be classed (perhaps somewhat simplistically) as analog and digital signal processing. All analog signal processing is undertaken in real time as the sample temperature is ramped, picking out only one or two decay components at a time. Some form of filter produces an output proportional to the amount of signal that they see within a particular time constant range. Most fre-

quently this is done by multiplying the capacitance meter output signal by a time-dependent weighting function, a concept generalized by Miller, Ramirez, and Robinson.⁶

Several different weighting functions were investigated in these analog systems, e.g., the double boxcar used in Lang's original DLTS work,⁵ the square wave (lock-in) system,^{7,8} exponential,⁹ and multiple boxcar.¹⁰ A major concern in all of this early work has been to try to improve or at least retain the signal-to-noise performance of Lang's original double boxcar system or at least to "optimize" the sensitivity versus resolution trade-off. The exponential correlator provides the greatest sensitivity but the worst resolution. Higher order filters provide the highest selectivity but the best that can be achieved in practice with these systems is an improvement of a factor of 2–3 in resolution at a substantial cost in terms of noise performance.

The topic had been revisited by Istratov¹¹ who pointed out that all weighting functions proposed prior to 1997 used nonsymmetrical rate windows which provide a higher order low pass band (filtering out slow transients) but lower order at the high-frequency edge. This results in mediocre filtering of the transients faster than the peak response. This is a contributory factor to the well-known peak shape in conventional DLTS where the low-temperature side of the curve is steep (low-frequency filter) while the high-temperature side is broad. Istratov calculates that a third order weighting function can, in principle, resolve two transients with a time constant ratio $\tau_1/\tau_2 \sim 8$. Our experience indicates that even this is rather difficult to achieve in practice and where two states of quite different concentrations are concerned it often requires interpretation of a shoulder on the larger peak... a particularly difficult issue if the smaller peak falls on the high-temperature side of the dominant feature.

In practice the majority of the world's DLTS systems are still simple analog processors based on Lang's original double boxcar design or a lock-in (square wave correlator) principle. The resolution performance of these is worse than higher order systems and can probably only distinguish transients with a time constant ratio τ_1/τ_2 of ~ 12 or ~ 15 , respectively.

One of the reasons for adopting this rather simplistic approach in commercial versions of DLTS systems is that complex (higher order) analog correlators are difficult to implement and extremely difficult to maintain in a state which gives optimum performance. However if the transient is digitized it is relatively easy to implement almost any correlation function or indeed more complex signal processing. The critical components are then the transducer and related circuitry used to monitor the occupancy of the state (usually a capacitance meter and pulse generator) and the analog to digital converter. The analog transient output of the capacitance meter is sampled and many digitized transients averaged to reduce the noise level. Assuming Poisson statistics the improvement obtained in signal-to-noise ratio using this procedure is $N^{0.5}$, where N is the number of transients averaged. All of the accessible decay time constants are then picked out of the acquired wave from by software.

This task of separating multiple, closely spaced, decaying exponential components in measured data is a general

scientific problem and has exercised the minds of many prominent mathematicians for at least two centuries. Essentially the problem of extracting multiple closely spaced decaying exponentials is fundamentally ill posed and so in the presence of noise there is no unique solution. Any practical method has to consider what might constitute a realistic answer to the problem and this process will be considered in detail later in respect of the Laplace transform. It is referred to as the regularization process.

The problem of what algorithm to use to extract the components in a digital system is difficult because of the very large number of possibilities at least in general terms. Looking specifically at the DLTS requirement there are some experimental factors, which narrow the field of acceptable options very considerably. In DLTS experiments the baseline to which the exponential transient decays is not known with any degree of precision so this must be taken as a variable in the analysis. The transients can be of either polarity and in some circumstances both polarities may be present simultaneously. An essential feature is that any algorithm must provide accurate amplitude as well as rate information in relation to each transient component.

However, perhaps the most difficult issue is that in DLTS not all states are expected to provide ideal exponential decays. The Poole-Frenkel effect (see, e.g., Ref. 12) results in an increased emission rate with increasing field and so in the range of fields within a depletion region the emission from a specific defect will change continuously within defined limits. Similarly inhomogeneous strain can produce a continuum of emission rates associated with a specific defect. It is highly desirable that the deconvolution algorithm recognizes that such phenomena exist and presents this information in a graphical form to the users ideally as a meaningful broadening of the δ function, which would otherwise represent the ideal monoexponential solution.

Many of these issues have been considered previously in the literature. Within the specific context of DLTS using digitized transients various schemes have been published and various degrees of success reported. Among the range of approaches that are of importance is the method of moments technique as exemplified by Ikossi-Anastasiou and Roenker.¹³ Nolte and Haller¹⁴ used an approximation the Gaver-Stehfest algorithm to effect a Laplace transform although achieving a substantial increase in resolution found the approach to be unstable in the presence of experimental noise levels. Eiche *et al.*¹⁵ use Tikhonov regularization to separate the constituent exponentials in a photoinduced current transient spectroscopy signal with an approach very similar to that which has been adopted for the work described in this review. Although many other methods have been used it is not intended to give a comprehensive treatment of the relative merits of the vast range of mathematical techniques here because the problem has been reviewed recently in considerable detail by Istratov and Vyvenko.¹⁶ This can be used as a reference on which to base the description of the implementation presented in the following section.

II. THE IMPLEMENTATION OF LAPLACE DLTS

A. Hardware and technical requirements

A Laplace DLTS system consists of a cryostat in which the sample is mounted, a transducer that monitors the thermal carrier emission after excitation by a pulse generator, and a data collection system for the averaging of transients. The averaged transient is then delivered to a computer which implements the Laplace transform and displays a representation of the deep-level spectrum.

It is quite evident from the discussions in Sec. I and references therein that to achieve high resolution in the separation of emission rates, the overriding issue must be the signal-to-noise ratio (SNR) of the processed transients. Temperature instabilities, lack of digitizing resolution pickup of 50/60 Hz signals, and $1/f$ fluctuations all constitute noise with different spectral characteristics and different significance in the Laplace transform. However for expediency the SNR is defined here as the ratio of the peak voltage of the measured transient to the rms noise voltage over the system bandwidth. In the following discussion the SNR of the transient stored for analysis is considered and also the SNR of the measured transient as it appears at the output of the transducer (usually a capacitance meter). These two SNRs are, in general, not the same because the SNR of the analyzed transient can be improved by averaging or in some cases degraded by digitization noise.

In order to provide a benchmark for the hardware requirements it is useful to consider that, using Tikhonov regularization algorithms, from fundamental considerations a SNR greater or equal to 10^3 is required in order to resolve signals of similar magnitude with a time constant ratio of 2. This value refers to the processed (averaged) transient. The detailed effects of SNR and measurement conditions are exemplified in the next sections for specific algorithms.

In selecting a measurement emission rate of around 10^3 s^{-1} (i.e., $\sim 1 \text{ kHz}$), Lang in his original DLTS experiments chose a part of the spectrum that is relatively noise free. This range escapes the worst effects of $1/f$ noise in semiconductor measurements and radio frequency pickup problems. It is also consistent with the probe frequency of 1 MHz commonly used in capacitance meters. In consequence emission rates in the range $5 \times 10^2 - 10^4$ are an appropriate working range for Laplace DLTS, although constraints on temperature and trap depth may necessitate operating well outside these rates.

A consequence of averaging a large number of transients is an increase in the measurement time. This will not necessarily improve the SNR if the system does not have a stable cryostat. Temperature shift of the sample is a particularly insidious source of noise and is more critical for shallow states. For a 100 meV state a stability of $\pm 50 \text{ mK}$ over the longest measurement period is required. The considerations above, which define the required signal-to-noise and the part of the spectrum in which the system will be operational, establish to a large degree the specification of many of the components of the system and place limitations on the type of semiconductor sample that can be measured.

Noise is introduced in the digitization process. An 8 bit A to D converter operating on a signal with no noise will limit the SNR to 250 and a 12 bit converter to 3000. This assumes that all the bits will be available for conversion of the transient. This is not always the case because of dc offset and the need to accommodate negative as well as positive signals. Allowing for measuring transients of both polarities and taking into account the practicalities of having some offset potential, it would seem a safe design target to select a 16-bit converter with 32 bits of memory for each point of the accumulated transient.

The ultimate noise limit is defined by the noise from the sample itself, but there are practical limits in what can be achieved in the transducer, which monitors the emission of carriers. In general, it is highly desirable to measure capacitance rather than current because this enables majority and minority carrier emission to be distinguished and, in practice, the vast majority of DLTS systems are based on capacitance meters. By far the most popular device for the measurement of capacitance transients is the Boonton model 72 B, which was designed over a quarter of a century ago. Although much more sensitive capacitance meters exist,¹⁷ the Boonton is an extremely usable device in the sense that it has an excellent rejection ratio of capacitance to ground as a result of a three terminal measurement system and uses only a small ac test signal (15 or 100 mV rms dependent on the model). It has an adequate response speed for most measurements (0.05 ms with minor modifications). In consequence, most Laplace DLTS systems use the Boonton model 72 B with an ac test signal of 100 mV at 1 MHz. When using the 10 pF range, the output noise level referred to the input is $\sim 1 \text{ fF rms}$.

Any modulation of the voltage supply to the test diode also provides a modulation of the capacitance and hence noise. For an abrupt junction diode or a Schottky barrier, $1/C^2 \propto V$ and so the noise on the power supply is amplified by a factor of 2 because of the dependence of the sample capacitance on voltage. Considering the limiting case, with 1 fF noise and requiring a transient for analysis with a SNR of 10^3 and averaging 100 transients, a SNR in the capacitance meter output of 10^2 (assuming white noise) enables a capacitance transient of 100 fF to be measured. For a quiescent capacitance of 10 pF (fairly typical for a DLTS sample) a power supply stability of $\pm 3 \times 10^{-5}$ would be required which on a 5 V supply is $\pm 0.15 \text{ mV}$. In practice the overall performance of an excitation circuit with a typical sample and a Boonton capacitance meter working on the 10 pF range is a noise level referred to the input of less than 0.5 fF rms.

A very obvious and pertinent question is how long should the transient be sampled for and how many samples should be taken? The first question is relatively simple to deal with. The proportionate difference between two exponential decays of similar time constants increases with time. For two transients with decay rates e_1 and e_2 the ratio of the amplitudes is

$$\exp \{(e_1 - e_2)t\}. \quad (6)$$

In practice this means that the sampling should continue until the noise level is reached for the longest transient. If, as

discussed above, a SNR at the capacitance meter of 10^2 is required then it is necessary to sample for about five times its time constant.

The decision which needs to be made in relation to the number of points to be sampled in a transient and subsequently analyzed is much more complicated. Istratov and Vyvenko¹⁶ draw attention to the fact that if one is analyzing a transient with three or four exponentials, in principle, something like 20 points is probably the optimum as the addition of more points merely increases the bandwidth of the system thus making the Laplace transform less stable. Ideally samples should be unequally spaced in time^{18,19} with smaller time spacing being used at the beginning of the transient (equispacing on a logarithmic time scale). In practice the real situation is rather different. A conventional A-D converter samples at a constant rate with a fixed sample time. It is of course possible to introduce some supplementary processing to provide logarithmic spaced sample times through mathematical fitting of groups of measured points. This process works very well for a single exponent, however in practice there are a number of exponential decays present during each DLTS measurement transient. In consequence the algorithm for optimizing the sampling and the precalculation of the samples depends on the solution, so that an iterative process is necessary and the whole procedure becomes so unwieldy that it is unusable in practical work. Another issue is the fact that the actual sampling time (the time data is averaged over in order to determine the value) of commercially available A-D converters is fixed so that there is no averaging between widely spaced digitized points. In reality this effective “averaging” is set by the system bandwidth so that there is a noise penalty in taking a small number of samples for the calculation.

Given that practical considerations require an equal sampling rate about 50 samples are needed for the monoexponential case. However as there will be a range of decay rates in the experimental data typically spanning three decades something of the order of 5000 samples are typically needed per measurement. The numerical routines referred to above provide a stable solution with this level of sampling.

B. Deconvolution algorithms and mathematical limitations

The spectral function is obtained from the measured transient by solving the integral:

$$f(t) = \int_0^{\infty} F(s)e^{-st} ds. \quad (7)$$

This equation is of a Fredholm-type, which means that, as discussed previously, the problem is fundamentally ill posed. As a result, an approximate spectral function can be obtained only from complex numerical approximation methods. The Tikhonov regularization method²⁰ is very effective for the LDLTS case. In general, in this method an oscillatory character of the spectral function, which could be a result of a simple least-square fitting procedure when the number of peaks (monoexponential components) is not constrained, is suppressed by an additional constraint imposed on the sec-

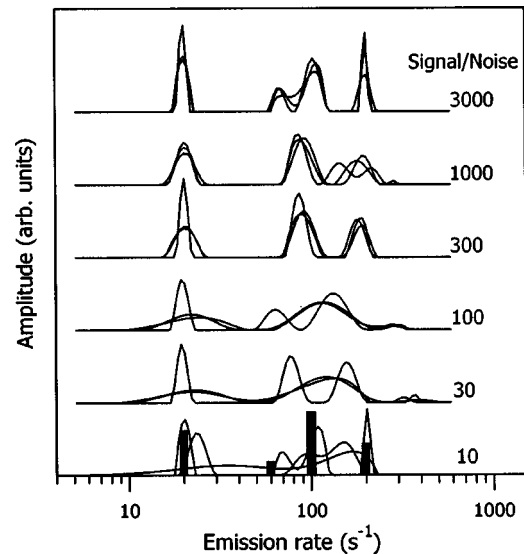


FIG. 2. Results of numerical tests demonstrating a role of the noise on the resolution of the methods implemented in the system described in this work. The bar diagram depicts the emission rates and amplitudes of four monoexponential components assumed in the simulated transients. For a given noise level three different numerical routines have been used.

ond derivative of the spectral function. In order to determine how much this second derivative has to be suppressed it is necessary to use a numerical method based on a statistical analysis of the magnitude and spectral distribution of the noise within the experimental data. Additionally all numerical methods employed in the Laplace DLTS system attempt to find a spectral function with the least possible number of peaks, which is consistent with the data and experimental noise; a procedure referred to as the principle of parsimony. This approach has the consequence that the computed spectra obtained are “noise free” in a sense that peaks having amplitudes around the noise level are removed from the spectra by the numerical procedures.

In our experimental manifestation of the Laplace DLTS system three different software procedures are used for the numerical calculations. All of them are based on the Tikhonov regularization method, however they differ in the way the criteria for finding the regularization parameters are defined. The first one²¹ (CONTIN) is in the public domain and has been obtained from a software library²² and modified in order to integrate it with our system. The outline code of the second one²³ (FTIKREG) is distributed by the same library but it has been substantially modified by the original authors for operation within our LDLTS system. The last one²⁴ (FLOG) has been specifically developed for the system. The parallel use of three different software packages substantially increases the level of confidence in the spectra obtained. Additionally, for preliminary data analysis a discrete (multiexponential) deconvolution method can be used.²⁵ This method is based on a simple integration procedure.²⁶

Many numerical tests have been performed using these software procedures in order to establish their reliability and performance in “difficult” cases. Some numerical tests have been published in the first presentation of the method²⁷ which we supplement here with some further detailed illustrative examples. Figure 2 shows the results of numerical

tests where the role of noise on the resolution of the three different methods is demonstrated. The bar diagram depicts the emission rates and amplitudes of four monoexponential components assumed in the simulated transients. The emission rate ratio between the two outer components is 10, which is slightly better than the resolution limit for conventional DLTS. The ratio of emission rates between two right-hand side components is 2 which is what is usually assumed as the LDLTS resolution limit for essentially noise-free transients. The two rates at the center of the diagram have a ratio of 1.7 and very different magnitudes.

The depicted results demonstrate typical instabilities when the numerical routines are used to analyze closely spaced exponentials in the presence of noise. The incorporation of the principle of parsimony in the software means that there is a tendency to approximate with a simpler spectrum (fewer components) than the real spectrum. It is seen that for a SNR worse than 300 the different numerical procedures do not produce the same result. This is a very clear indication that they cannot cope with the combination of resolution and noise level. For a SNR of 300 one obtains agreement between the solutions but the two middle components with an emission ratio of 1.7 stay unresolved. Only for the very high SNR of 3000 (which in most cases is unrealistic experimentally) are all components properly revealed in terms of the emission rates and amplitudes.

For many physical problems the Tikhonov regularization enables an approximation to the spectral function that agrees with *a priori* knowledge. However, by necessity, specific assumptions have to be made in order to obtain these spectra, which impose important limitations. Each spectrum is calculated with one unique regularization parameter. This means that all peaks on the spectrum will have a similar curvature (the second derivative). This is a direct consequence of the fact that the value of the second derivative of the spectral function is one of the constraints. As a result, physical problems, which are represented by strongly asymmetrical peaks or by two peaks where one is narrow and the other broad, will not be analyzed properly. Figure 3 demonstrates one aspect of this effect. The spectra shown by solid lines were calculated (using the CONTIN method) from simulated transients, which were generated from the spectra shown dotted. The amplitudes and emission rates for the centers of gravity for the two peaks for all the examples are equal, only the width of the peaks is different. In practice broadening of the emission peaks (representing a continuum of rates) can be observed in LDLTS. This can be due to the Poole-Frenkel effect (enhancement of the emission rate due to an electric field), inhomogeneous strain or in some cases alloying effects.

It is evident from Fig. 2 and 3 that as long as the broadening does not cause overlapping peaks, the calculated spectra reflect the true broadening. When the peaks gradually merge then the calculated spectra underestimates the broadening. Eventually when the overlap becomes substantial the calculated result begins to look more like one asymmetric peak and finally reaches the applicability limit of the Tikhonov regularization method. At this limit the numerical software has a tendency to force the spectrum to oscillate and

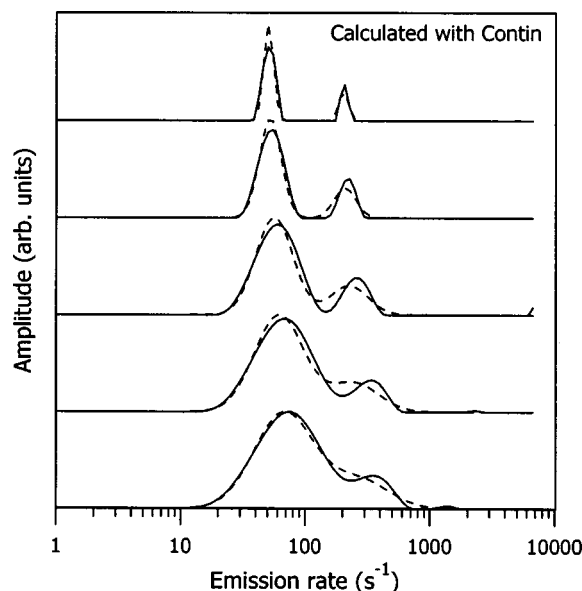


FIG. 3. Numerical tests calculated with the Contin procedure (solid lines) for the transient generated for the spectral functions are shown by dashed lines. These tests show a tendency of the Tikhonov regularization method of force a peak to be more symmetric than in reality.

attempts to create a number of narrower peaks. When the separation between peaks becomes even smaller then the numerical method approximates a true asymmetric structure by one broad and symmetric peak. In such uncertain situations different numerical methods behave differently which is a clear indication that the level of confidence in the calculated spectra should be low. For a single physically broadened peak with no other peaks nearby the broadening is revealed properly.

These issues are central to the degree of confidence in the results obtained from Laplace DLTS and are discussed in relation to specific systems in the following sections of this paper. It is very difficult to generalize in relation to what can and cannot be measured with the technique. Certainly point defects in elemental semiconductors are ideal candidates and the effect of uniaxial stress on such defects provides clear unambiguous data. In dilute alloys (SiGe with Ge < 8% is reported in detail in this review) it is possible to discern the effects of the local environment at the first-nearest neighbor level and in ideal experimental conditions broadening due to second-nearest neighbor effects can be seen. However at significantly higher Ge content the separate components cannot be revealed. In compound semiconductors much less dilute alloys have been studied by Laplace DLTS but the broadening is system specific. In highly dislocated material or material with inhomogeneous strain the technique is not viable. In GaN and its alloys, for example, Laplace DLTS results obtained to date are ambiguous, presumably because of the profound effect of inhomogeneities on the carrier emission properties of the defects.

Another area where Laplace DLTS techniques have to be used with great caution is in relation to extended defects and particularly ion implant damage. The defects near the end of the ion implant range comprising clusters are very important technologically. Several studies of such damage in silicon

appear in the literature and some are discussed in this paper but it is very difficult to decide if the spectra represent specific defect clusters and much more work is needed to resolve this issue.

C. State of the art performance

It must be evident from the previous discussion that the actual performance achieved with Laplace DLTS depends on many factors of which one of the most important is the noise in the transient quantified as the SNR. In the preceding section we have considered what are likely to be the fundamental limits to resolution of the software in terms of separating exponentials with similar time constants with simulated SNRs. In practice the performance achieved approaches this in a well-engineered system. What this means is that noise sources extraneous to the transient must be made negligible (e.g., temperature drift, digitization noise, and bias supply stability). Essentially if a sample with a trap concentration $\sim 1\%$ of the shallow dopant concentration and a quiescent capacitance ~ 10 pF is studied the SNR requirement ~ 1000 in the averaged transient is readily achievable. This is necessary in order to resolve signals of similar magnitude with a time constant ratio of 2. To give some idea of the effect of noise it should be possible to resolve two exponentials with a time constant ratio of 3 if the SNR is 100 and a ratio of 5 for a SNR of 30. These can generally be regarded as limits in the presence of white noise, strong coloration of the noise is usually detrimental.

If transients with similar emission rates but different magnitudes are studied accurate separation is more difficult to achieve. For a case of SNR=1000, an emission rate ratio of 2, and a magnitude ratio of >3 , significant errors in the determination of the rate and magnitude of the smaller transient occur. For the case where the magnitude ratio is >10 the smaller transient is invariably lost. The situation recovers if the emission rate ratio is larger.

In situations where there are a number of transients with closely spaced emission rates the results are in general unreliable. It is difficult to quantify limits but for the case of SNR=1000 and component transients of similar magnitude any solution which indicated more than four components within the range $10\text{--}1000\text{ s}^{-1}$ must be suspect.

In many semiconductor measurement techniques broadening of the line shape is a valuable guide to underlying physical phenomena. In conventional DLTS instrumental broadening is so large that it masks all but very gross broadening due to the defect physics. In Laplace DLTS this is not the case and line broadening is potentially important in the interpretation of the spectra. Consequently it is desirable that the software be designed so that in the ideal case (a single transient with no others observed with similar rates) the calculated broadening accurately reflects the true broadening. However, it is important to note that if a spectrum contains a broadened line and a narrow line (e.g., donor like deep state in n-type exhibiting a pronounced Poole-Frenkel effect and an acceptorlike state in the same spectrum which is not

broadened) both lines will appear broad in the calculated spectrum. This is a fundamental feature resulting from Tikhonov regularization.

In the following three sections we present some experimental studies of various defect systems, which illustrate the issues discussed above.

III. APPLICATION TO CHARACTERIZATION OF DEEP CENTERS WITH SIMILAR EMISSION RATES

A. Separation of levels

Perhaps the most obvious application of Laplace DLTS is to separate states with very similar emission rates. The poor resolution of conventional DLTS has been a recurring theme in the literature and resulted in considerable confusion over the "identity" of particular DLTS fingerprints. These problems became very evident when compilations of the Arrhenius plot data were published in various reviews (see, e.g., Refs. 28–31). Using conventional DLTS, it is sometimes possible to separate states with very similar emission rates, provided they have different activation energies, by conducting the DLTS experiment over a very wide range of rate windows. However, this produces no advantage if the activation energies are also very similar. Occasionally states appearing with very similar emission rates have very different capture properties. In these cases the deep state with the smaller capture cross section can be eliminated by reducing the filling-pulse width and so some measure of separation is achieved. Another method which has been used with conventional DLTS is to examine the peak shift as a function of electric field. Again, occasionally, it is possible to separate a state, which exhibits a strong Poole-Frenkel effect from one which does not.

Unfortunately, these tricks cannot be generally applied and have only been successful in a few specific cases. Essentially there is no substitute for higher resolution. In this section, we examine a number of specific cases where defects have very similar emission rates and prior to the application of Laplace DLTS it has been very difficult (or impossible) to separate their properties. In the following section, we consider the gold acceptor and the gold hydrogen complex G4. We then examine levels, which are associated with dangling bonds and then a variant on the vacancy-oxygen complex or A center.

We then move on to demonstrate how methodologies used in conventional DLTS can be applied within Laplace DLTS measurement to determine detailed properties of closely spaced defects. First, we consider the use of varying filling-pulse widths to establish the capture rate, then the use of the Laplace technique to study minority carrier capture and emission and then an example of a spatial profiling using Laplace DLTS. Finally, in this section, we look at inhomogeneous broadening phenomena resulting from local strain and then electric-field effects.

1. The gold acceptor and the G4 gold-hydrogen complex in silicon

A very good example of states which are distinctly different structurally but have very similar activation energies

and emission rates in silicon are the gold acceptor and a gold-hydrogen complex referred to as G4. There has been much work in recent years on hydrogen reactions with impurities and defects in silicon. Initially work concentrated on the electrically inactive reaction products resulting from the passivation of shallow impurities,³² but it is also well known that hydrogen is implicated in a wide range of reactions with defects in silicon which produce electrically active species.³³ In particular the effect of hydrogenation of gold in silicon has been studied in some detail.

It has been reported that there are four electrically active deep levels (referred to as G1, G2, G3, G4) resulting from the formation of Au-H complexes of which it is believed that G1, G2, and G4 are different charge states of the same Au-H pair.^{34–36} It is generally accepted that gold (without hydrogen) forms an acceptor which acts as a majority carrier trap in n-type silicon. The G4 level appears to be very close in energy to the gold acceptor and has almost identical electron emission characteristics. Consequently it is not possible to characterize the G4 level using conventional DLTS because of the limitations of resolution. However, an apparent temperature shift of the gold acceptor DLTS peak after wet chemical etching has been observed^{34,35} and careful deconvolution suggested that this peak consists of two contributions in hydrogenated silicon, one from isolated gold acceptors and the other from the G4 center. LDLTS has been used to resolve two distinct levels in the region of the gold acceptor G4 electron emission rate and enables the activation energy and capture cross section of G4 to be determined.³⁷

Samples were prepared from phosphorus doped Czochralski silicon by gold diffusion at $\sim 900^\circ\text{C}$ after which hydrogen was introduced by wet etching in CP4 ($\text{HNO}_3:\text{HF}:\text{CH}_3\text{COOH}$ in the ratio 5:3:3). Gold Schottky diodes were fabricated to enable the LDLTS measurements to be made.

Figure 4 shows a comparison of the LDLTS and DLTS spectra obtained from the same Si: Au, H sample. Both spectra were taken with 5 V reverse bias and a 1 ms filling pulse of 0 V. The 50 s^{-1} rate window DLTS spectrum shown as the inset consists of the typical broad featureless peak in the region of 260 K as reported previously.^{34,35} The LDLTS spectrum shown in the main part of Fig. 4 reveals that there are two separate and quite distinct bound to free electron emission rates at the measurement temperature of 260 K. This confirms unambiguously that the conventional DLTS peak at the Au-acceptor position in hydrogenated silicon consists of two contributions.

Figure 5 shows the effect of a low temperature anneal (250°C for 5 min) on the LDLTS spectra measured at 296 K. It can be seen that the lower emission-rate peak diminishes significantly with annealing while the higher rate peak increases. There is strong evidence from previous work^{34,35} that the DLTS peak at around 120 K (referred to as G1) is another charge state of the same AuH complex as G4. Measurements of the G1 Laplace DLTS signal from the same sample show that this peak also diminishes with the above anneal schedule. From this it is concluded that the lower

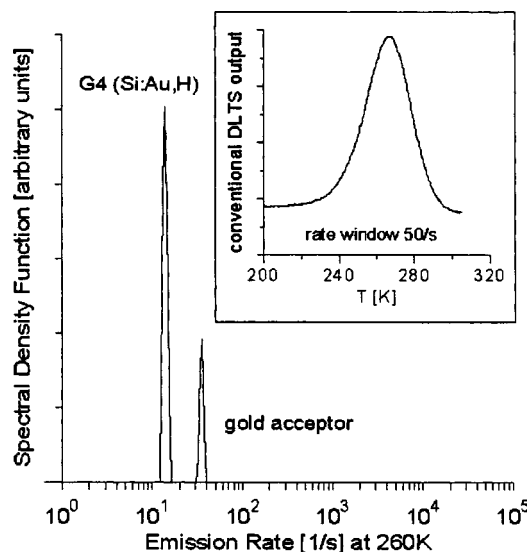


FIG. 4. Reproduced from Deixler *et al.* (Ref. 37) DLTS and LDLTS spectra of hydrogenated silicon containing gold. The conventional DLTS spectrum is shown as an inset at the top right of the figure. The broad peak centered at 260 K is attributed to electron emission from the gold acceptor and G4. The main spectrum uses the Laplace technique and clearly separates the gold-acceptor level and the gold-hydrogen level G4.

emission-rate peak is due to the gold-hydrogen complex G4 while the higher emission rate peak is due to the gold acceptor.

Repeating the LDLTS at temperatures in the range 245–300 K enables the Arrhenius plot shown in Fig. 6 to be constructed. Samples with different carrier concentrations and different orientations gave results, which were indistinguishable within the accuracy of the measurement. From the upper line in Fig. 6 an activation energy of 558 meV is obtained, and for the lower line 542 meV. The annealing measurements enable us to assign the 558 meV energy to the gold acceptor and the 542 meV to G4. It is known that the

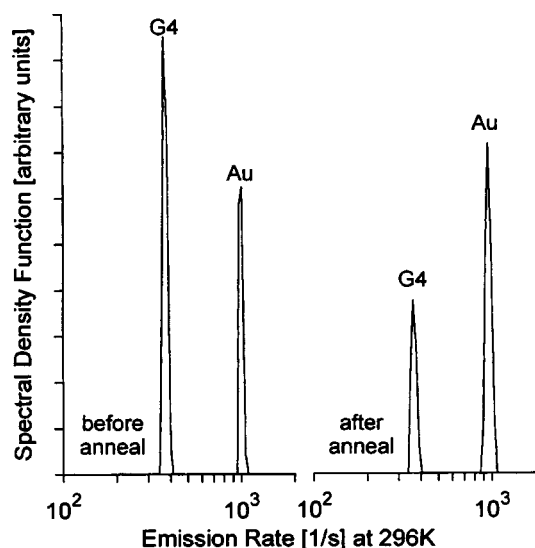


FIG. 5. Reproduced from Deixler *et al.* (Ref. 37). Comparison of Laplace spectra of the G4 and gold-acceptor level taken (left) and after (right) annealing at 250°C for 5 min. The results of the two measurements are presented on the same scale. It can be seen that the G4 peak is reduced substantially while the gold-acceptor peak shows a small increase.

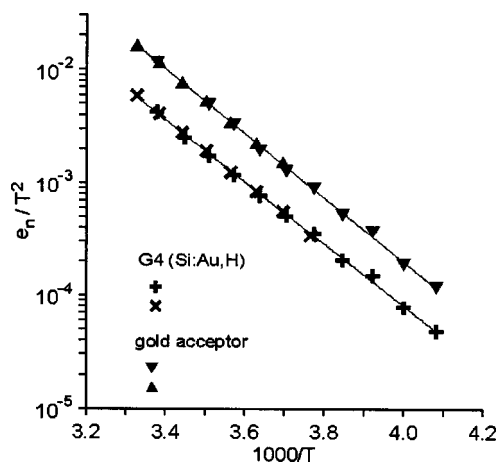


FIG. 6. Reproduced from Deixler *et al.* (Ref. 37). Arrhenius plots, obtained DLTS measurements, of the thermal emission rates for the gold-hydrogen level G4 and the gold-acceptor level. The different symbols on each line represent measurements taken in different laboratories on different samples. Activation energies derived from the slope of the least mean square fit are 542 meV (G4) and 558 meV (gold acceptor).

directly measured capture cross section for electrons into the gold acceptor is essentially temperature independent over the range 80–300 K (Refs. 38–40) and so the 558 meV represents the enthalpy of the gold acceptor. Consideration of the scatter on the data and the possible errors in the determination of sample temperature and calculation of emission rate put a maximum error of ± 8 meV on these values. Most previous measurements of the enthalpy of the gold acceptor lie in the range 550–560 meV.^{38–41} This provides further evidence in support of the assignment of the lower emission rate to the gold-hydrogen complex G4, and the higher emission rate to the gold acceptor.

2. Dangling-bond levels

A particular class of deep levels can be associated with defects that possess an unsatisfied bond in the bulk semiconductor. Generally speaking such dangling bonds will generate defects in the band gap that, depending on the “squeeze” of the dangling bond, may form classes with rather similar energy levels. Hence, the level position is predominantly a property of the dangling bond and has only a weak dependence on the detailed structure of a specific defect. The origin of dangling bond levels can be traced back to the formation and decoration of lattice vacancies in the semiconductor crystal. For example, when Si is subjected to ionimplantation a rather dense concentration of vacancy clusters will be generated with the consequence that several close lying acceptor-type dangling-bond levels appear rather deep in the upper half of the band gap. Even with the Laplace method these multilevel structures are hardly resolvable (see discussion in Sec. II), and consequently the average over level energies may equally well (or better) be obtained with conventional DLTS. However, when only two or possibly three dominant close levels are present the application of Laplace DLTS offers the advantage that reliable individual level positions and defect abundances can be obtained.

We illustrate this by comparison of Laplace data obtained for the similar dangling-bond acceptor levels

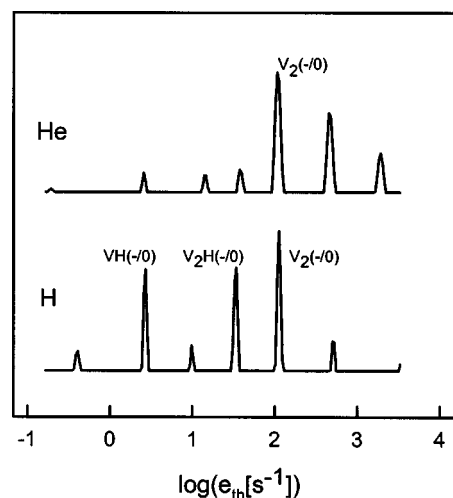


FIG. 7. Laplace DLTS obtained at 225 K. Lower plot, hydrogen-implanted sample ($\sim 10^{10}$ cm $^{-2}$); upper plot, helium-implanted sample ($\sim 10^9$ cm $^{-2}$). The samples have been implanted at 60 K and subsequently reverse-bias annealed at 400 K. (Ref. 44).

VH(–/0), V_2 H(–/0), and PV(–/0). The similarity of the electronic structures of these centers has been established by electron paramagnetic resonance (EPR) Bech Nielsen *et al.*⁴² and Stallings *et al.*⁴³ The neutral charge state of the three defects (VH^0 , V_2H^0 , and PV^0) has very similar EPR spectral parameters, indicating that the wave functions of the odd electron are indeed very similar. The acceptor level of these centers originate from the emission of an electron from the dangling-bond orbital to the conduction band leaving the orbital singly occupied, and consequently the level energies are also expected to be similar. The Laplace spectra depicted in Fig. 7 as reproduced from Bonde Nielsen *et al.*⁴⁴ compare proton- and helium-implanted samples after reverse-bias annealing at 400 K to remove the phosphor-vacancy E center. As can be seen two prominent vacancy-hydrogen related levels are revealed together with the V_2 (–/0) level. The assignment of these levels as VH(–/0) and V_2 H(–/0) are based on the comparison of annealing properties with the EPR data of Refs. 42 and 43. It should be noted that Andersen⁴⁵ recently has shown that the Laplace DLTS signal ascribed to VH(–/0) is generated with large intensity when electron-irradiated silicon is subjected to hydrogen-plasma treatments. This could indicate that the signal should perhaps be interpreted as V_2 H(–/0) formed in direct capture of hydrogen at the double vacancy V_2 . However, this ambiguity cannot be settled easily as it would require further quantification of the mechanisms of the injection of hydrogen in plasma treatments. The similarity of the V_2 H(–/0) and VH(–/0) levels is easily rationalized. The divacancy V_2 (–/0) level may be qualitatively understood as originating from two weakly interacting elongated dangling bonds. In V_2H^0 hydrogen terminates one of these bonds leaving the other practically undisturbed. The presence of the V_2 (–/0) level in the same energy range supports this qualitative picture. In VH^0 hydrogen breaks the unsaturated bond structure of the monovacancy generating a structure consisting of one dangling bond, a Si–Si bridge, and a hydrogen terminated bond. The annealing removed the strongly interfering PV(–/0) signal. The simi-

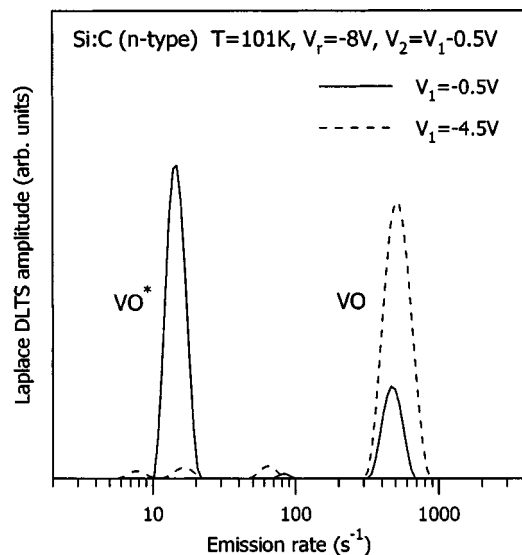


FIG. 8. The Laplace DLTS spectra taken in the differential mode for the silicon sample irradiated with electron at low temperature and measured *in situ*. The spectra show that the metastable configuration of the VO complex (VO^*) is observed only close to the sample surface (solid line) due to the fact that at this region the annealing process of the defect occurs in the conditions of a low position of the Fermi level.

larity of this with $VH(-/0)$ shows that the Si-H fragment of VH^0 may be regarded as a “pseudo Group-V impurity” as far as giving rise to a very similar dangling-bond level when binding to a lattice vacancy.

3. The vacancy-oxygen center

A typical procedure to create the vacancy-oxygen complex (the A center) in n-type silicon is to irradiate the crystal with electrons at room temperature. The appropriate dose of electrons creates vacancies in the material which at this temperature are very mobile and thus can be trapped by interstitial oxygen atoms. Obviously, when the irradiations are undertaken at low temperatures where vacancies are immobile the VO complexes are formed only in very small concentrations. We have examined the creation process of the VO complex by irradiating diodes at low temperature (around 60 K) and subsequently monitoring the growth of the VO center by Laplace DLTS in a sequence of isochronal annealing steps.⁴⁶ We find that prior to VO creation some other metastable form of VO (labeled here as VO^*) is present which converts one-to-one to the stable form of VO. This transformation process depends on the position of the Fermi level. For the bias-off annealing (the Fermi level is close to the conduction band) this occurs at around 130 K while for annealing with bias-on the transformation is observed at 250 K.

Figure 8 shows LDLTS spectra of a carbon-doped n-type sample of silicon irradiated with electrons at low temperature and subsequently annealed at 200 K for 10 min with an applied bias of -3 V. Annealing with a moderate reverse bias results in two families of annealed defects. Those that were within and those that were outside the space charge region during annealing corresponding to low and high Fermi level positions, respectively. The spectra depicted in Fig. 8 have been measured in the differential mode of DLTS, i.e., two

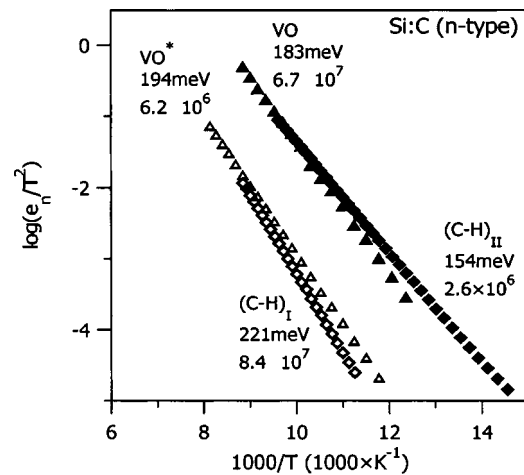


FIG. 9. Arrhenius plots of the $(C-H)_I$, $(C-H)_{II}$, VO^* , and VO defects measured at exactly the same experimental conditions. The plots demonstrate differences between the emission characteristics of the carbon- (square) and oxygen-related defects (triangles) in the stable (full symbols) and metastable (open symbols) configurations.

filling pulses of different voltages have been applied with the difference between the transients following each of the pulses used for analysis. Both spectra have been obtained with the same value of the reverse bias. The voltages of the filling pulses were chosen so that the spectrum depicted by the solid line originates from the region annealed with low Fermi level while the dashed line represents the spectrum measured for the defects annealed with high Fermi level. As a result of this procedure, VO^* closer to the sample surface has not been completely converted to VO whereas VO^* outside of the space charge region (dashed line) converted completely to VO. Hence, because of this particular annealing history, the signal of VO^* configuration originates from close to the sample surface.

The assignment of VO^* to some alternative configuration of the VO pair is not straightforward due to the fact that this particular crystal contains a high concentration of carbon. Moreover, the described conversion has a close resemblance to the $(C-H)_I$ to $(C-H)_{II}$ conversion phenomenon investigated in Ref. 47 both in terms of annealing behavior and emission rates. It is possible that the electron irradiation releases some of the hydrogen hidden in the crystal in the form of molecules or attached to other defects/dopants. The released hydrogen atoms could subsequently be trapped by carbon. However, this possibility has been ruled out by a careful analysis of the annealing procedure, and further conclusive arguments for the existence of VO^* have been obtained from the Arrhenius analysis of the emission characteristics depicted in Fig. 9. For this analysis, two samples placed in the cryostat at the end of the accelerator line have been irradiated at low temperature. One sample was irradiated with electrons and one was implanted with hydrogen as in Ref. 47. In the hydrogen implanted sample the $(C-H)_I$ and E3' (the isolated bond-centered hydrogen) signals are present as implanted and both signals convert after annealing to the $(C-H)_{II}$ signal. The figure compares the Arrhenius plots of $(C-H)_I/(C-H)_{II}$ with those of VO^*/VO observed in the electron irradiated samples. It has to be stressed that both samples have

been studied under exactly the same experimental conditions and hence the analysis presented in Fig. 9 enables the conclusion that neither of the defects revealed by in the spectra of Fig. 8 involve carbon and/or hydrogen.

This conclusion underlines the potential for the realization of accurate Arrhenius analyses with the Laplace DLTS system. Although the emission characteristics for the metastable and stable oxygen and carbon-related complexes are similar, the Arrhenius plots could be clearly separated. This is because of the way the Arrhenius analysis with the Laplace technique is realized. In LDLTS the emission time constants are measured isothermally at a very stable and precisely known temperature. This is unlike conventional DLTS where the temperature gradients on the sample holder during the temperature ramping procedure (necessary during the measurement) can be as large as several kelvin. A good cryostat can stabilize the temperature with an accuracy much better than 0.1 K. As a result, in LDLTS each capacitance transient can be acquired in meaningful 1 K steps or less if necessary. For a defect with an activation energy around 200 meV and the emission measured around 100 K an increase of the sample temperature by 1 K speeds up the emission approximately by 30%. Thus using 1 K steps one obtains around 30 points on the Arrhenius curve to cover a three decade range of emission rates. For a good signal-to-noise ratio the error of the emission rate calculation is typically better than 5% thus even smaller temperature steps are justified.

In Fig. 9 the data points for the individual defects follow straight lines almost exactly which makes the parameters obtained from the linear regression procedure very accurate. The values of activation energies given in this figure have errors less than 1 meV. One may argue that for this type of absolute experimental accuracy it is necessary to eliminate all possible sources of errors (e.g., the sensor anchoring and calibration) thus the derived activation energies may have additional systematic errors. However, the comparative studies presented demonstrate that the isothermal transient acquisition in combination with the Laplace analysis can be a very efficient tool for defect identification.

B. Separation of capture rates

Direct measurement of the capture process provides valuable information regarding the nature of the defect, essentially because the dominant factor in the capture rate is the Coulombic term, so that attractively charged defects have large capture cross sections and repulsively charged defects have small capture cross sections. In conventional DLTS, the capture cross section of a majority trap is measured by reducing the width of the filling pulse and observing the change of amplitude of the DLTS peak. The details of majority carrier capture measurement and application to minority cross sections are discussed elsewhere (e.g., in Ref. 4). By plotting the log of the proportion of traps unfilled against the filling-pulse length the majority carrier cross section can be determined from the slope of the line and the value of the free carrier concentration of the semiconductor. An identical approach can be taken in Laplace DLTS with the advantage that traps with very closely spaced emission rates can be

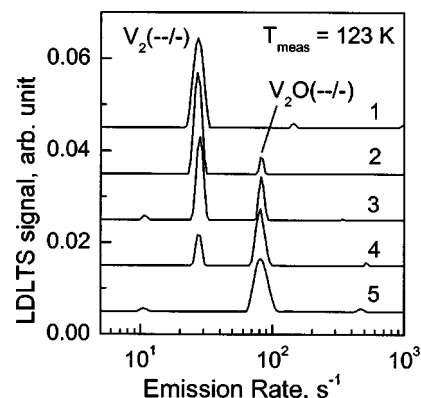


FIG. 10. Reproduced from Markevich *et al.* (Ref. 48). Development of Laplace DLTS spectra measured at 123 K for an electron-irradiated Cz-Si sample with an initial resistivity of 5 Ω cm upon 30 min isochronal annealing with temperature increments of 25°C. The spectra were measured after anneals at (1) 150, (2) 200, (3) 225, (4) 250, and (5) 275°C. Measurement setting were bias $-5 \rightarrow -0.2$ V and pulse duration 1 ms.

separated, but with the disadvantage that the reduced sensitivity of Laplace in terms of concentration means that a smaller dynamic range of occupancy can be covered. A very good example of the use of Laplace to study capture has been presented recently by Markevich *et al.*⁴⁸ In this work, n-type silicon was studied which had been irradiated with 4 MeV electrons. During a low-temperature anneal (225–350°C) it was observed that the divacancy disappeared, but this was correlated with the appearance of two other traps which were believed to be charge states of V_2O . Figure 10 shows the Laplace spectra of the double acceptor state of these two defects measured at 123 K after various anneal times. Using conventional DLTS, these two defects cannot be separated. However, by the application of the reduced filling-pulse technique during the Laplace measurement, the capture cross section of the defects can be determined independently. The measured cross sections are shown in Fig. 11 as a function of temperature. The electron capture cross section of the acceptor state of the divacancy follows the relationship $5.7 \times 10^{-16} \exp(-0.017 \text{ eV}/kT)$, while the cross section of the acceptor state of the V_2O defect follows the relationship $4.3 \times 10^{-16} \exp(-0.01 \text{ eV}/kT)$.

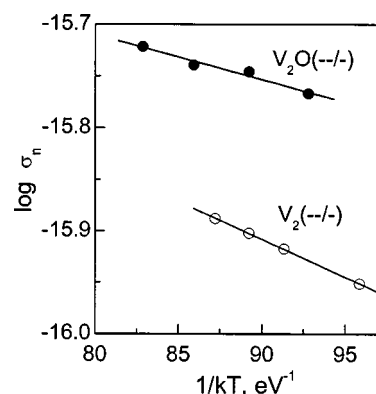


FIG. 11. Reproduced from Markevich *et al.* (Ref. 48). Temperature dependencies of electron capture cross sections for the double acceptor levels of the V_2 and V_2O in silicon. Solid lines are calculated ones on the basis of the equation $\sigma_n = \sigma_\infty \exp(-E_\sigma/kT)$ with parameters determined from least-square fits of experimental data.

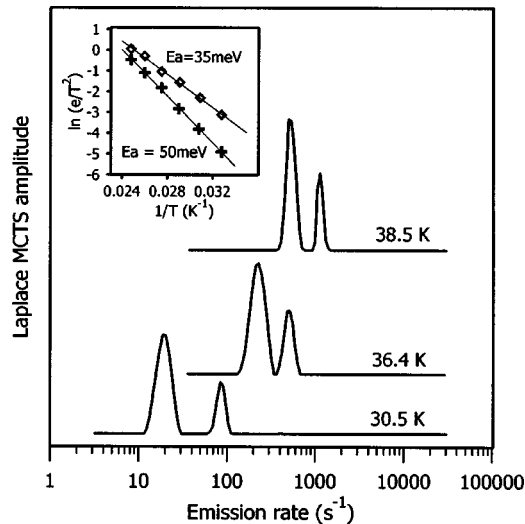


FIG. 12. Adapted from Gad and Evans-Feeman (Ref. 52). Laplace minority carrier transient spectra of hole emission from two point defects measured in *n*-type strained Si/Si_{0.855}Ge_{0.145}/Si quantum wells between 30.5 and 38.5 K. Arrhenius plots of the two states are shown in the inset.

C. Minority carrier capture and emission

Techniques to study minority carrier capture were first described in detail by Sah *et al.*¹ The methodology is very similar to majority carrier measurements with the exception that the occupancy is perturbed by the capture of minority carriers. In Lang's original paper on DLTS,⁵ this was done by forward biasing a p-n junction, but it can be done much more controllably in indirect band-gap semiconductors by using a filling pulse of above band-gap light shone into the semiconductor either through the back face or through a transparent Schottky barrier.⁴⁹ If the light has a photon energy near the band gap of the semiconductor being studied (hence the extinction depth is long) and the diffusion length is long, the carrier flux through the depletion region will consist almost entirely of minority carriers and so the analysis of the results becomes relatively simple and is known as minority carrier transient spectroscopy (MCTS).⁵⁰ These techniques have been used in Laplace DLTS to study minority carrier capture by gold and gold-hydrogen defects,^{51,52} and also shallow electron traps in p-type SiGe and trapping in silicon Si/SiGe/Si quantum wells.⁵² In this work the layers studied were grown by gas source molecular-beam epitaxy (MBE) and consisted of ten strained Si_{0.855}Ge_{0.145}/Si quantum wells grown on a Si substrate, with a Si buffer 100 nm thick. The well thickness was 5.7 nm, and the barrier thickness was 55 nm. The layer was n-type phosphorus doped at $1 \times 10^{16} \text{ cm}^{-3}$. Above band-gap light with an extinction depth greater than the depletion region width was used to create electron-hole pairs by illumination through a semitransparent Schottky diode. Because majority carriers are repelled from the depletion region predominantly minority carriers are available for capture in the depletion region. Figure 12 shows the Laplace signal derived from hole emission associated with two closely spaced shallow traps in n-type SiGe with the Arrhenius derived from the LMCTS data inset. These two defects exhibited almost perfect exponential fill-

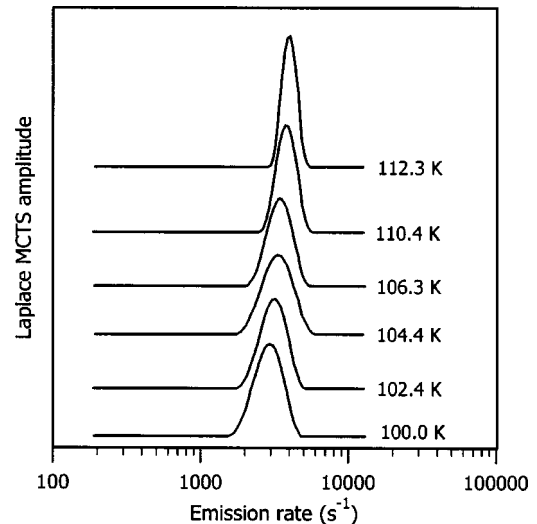


FIG. 13. Reproduced from Gad and Evans-Feeman (Ref. 52). The LMCTS spectra of thermally assisted hole tunneling from strained Si/Si_{0.855}Ge_{0.145}/Si quantum wells between 100 and 112.3 K.

ing behavior during the capture phase and consequently can be attributed to point defects, although the physical nature is unknown.

The composition and dimensions of these strained Si/SiGe/Si quantum wells would result in a valence-band offset of 117 meV with the deepest confined hole state at about 110 meV. In consequence, it would be expected that in this n-type material some of the holes emanating from the optical excitation would be trapped in the wells. Figure 13 shows a minority carrier Laplace DLTS measurement of hole emission from the quantum well. It can be seen that the emission rate is only slightly temperature dependent, a feature which is attributed to the tunneling component.⁵² Such data are very difficult to extract from conventional DLTS because of the proximity in emission of other defects in typical SiGe structures.

D. Spatial separation of defect centers

Electrical measurement techniques based on depletion measurement such as CV and DLTS enable properties to be measured as a function of depth simply by changing the voltage range in which the measurement is done. In DLTS there are numerous possibilities for doing this. It is possible to change the reverse bias with a fixed filling-pulse voltage, to fix the reverse bias and change the filling pulse, or to change both simultaneously. A very effective methodology is the double DLTS technique, which is essentially a differential technique using different filling-pulse magnitudes.

Analog of all these methods can be used with Laplace DLTS and indeed we have already cited an example of the use of the double LDLTS technique in Sec. III A 3. However the correct interpretation of deep-level profiles is fraught with difficulties due to the role of the Debye tail in the capture and emission kinetics and in some cases due to the effect of the changing electric field. These issues are discussed in detail elsewhere, but are equally applicable to Laplace measurements of deep state profiles as to conventional DLTS.

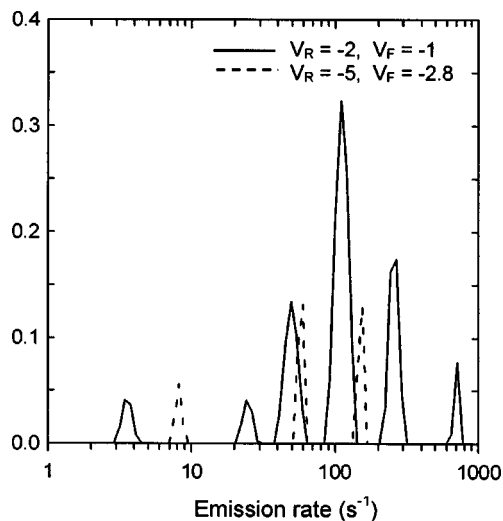


FIG. 14. Reproduced from Abdelgader and Evans-Freeman (Ref. 55). LDLS spectra measured at 225 K, reproduced from the vacancy-rich region and the interstitial-rich regions after annealing a self-implanted Si sample at 180 °C for 20 min. The solid line shows the emissions rates present in the capacitance transient due to trap capture and the thermal emission in the vacancy-rich region. The dashed line shows the emission rates present in the capacitance transient due to trap capture and thermal emission in the interstitial-rich region.

In recent years, perhaps one of the most important areas to which deep-level profiling has been applied has been that of ion implantation damage. When an impurity is introduced into a semiconductor using ion implantation, vacancy interstitial pairs are created along the ion track. Most of these intrinsic defects recombine or are annihilated at the surface and interfaces; some form pairs or clusters and some react with impurities to form stable defects. In the case of silicon implanted at room temperature, the region between the semiconductor surface and the concentration peak of the implanted species tends to be vacancy rich, whereas the region beyond the peak tends to be interstitial rich. During high-temperature annealing, these populations equilibrate with the excess of interstitials escaping to the surface or accumulating near the end of the ion range to form extrinsic stacking faults.⁵³ The detailed kinetics of this process are critically important because during equilibration the diffusing interstitials can react with substitutional species with important technological consequences. The best known is probably the enhancement of boron diffusion, due to the release of interstitials during annealing.⁵⁴

Unfortunately, many defect species are involved in these reactions and it has proved extremely difficult to track the behavior experimentally by any technique, including conventional DLTS. Laplace DLTS offers some advantage in this regard because of its ability to separate different species.

Figure 14 shows some results that have been obtained in studying self-implanted silicon with Laplace DLTS.⁵⁵ In this diagram, the electron emission from defects is shown after annealing 2 Ω cm silicon implanted with a low dose (10^{19} ions cm^{-2}) of 800 keV silicon after annealing at 180 °C for 20 min. The peak of the implanted silicon is 1.2 μm from the surface and the measurement conditions for the vacancy-rich spectrum (solid line) were -1 V fill and -2 V reverse

bias pulse (spanning the region 0.82–1.1 μm from the surface) and for the interstitial-rich region (dashed line) -2.8 V fill and -5 V reverse bias (1.28–1.68 μm). These depths are based on the depletion approximation.

Although it is not as yet possible to interpret these spectra in terms of defect species, the difference between the two regions is clearly evident and can be seen to evolve on further annealing.

E. Inhomogeneous and homogeneous broadening phenomena

1. Local strain

The local strain in the crystal can modify the electronic levels of a defect in the same way as the effect of the external stress discussed in the following section. Basically, this strain can be invoked by any macroscopic inhomogeneity of the crystal such as large defect clusters, extended crystal damage caused by implantation, dislocations, etc. This effect may cause the electronic level of the defect to broaden which is virtually impossible to analyze. Sometimes in the literature quantitative statements referring to the inhomogeneous broadening of the level can be found. The Laplace DLTS method usually fails to give conclusive results in cases where the broadening is substantial. The numerical methods used for the spectra calculations do not give stable and reproducible solutions when applied to broadened spectra, which is the fundamental condition for reliability of the measurement. Many such cases have been observed, in particular when the samples have been subjected to heavy implantation damage.

Point defects studied in the epitaxial layers can be subjected to almost homogeneous strain originating from the lattice mismatch between the layer and the substrate. In the epitaxial layer the lattice mismatch causes a two-dimensional planar strain parallel to the interface. This strain is equivalent to hydrostatic pressure applied to the layer combined with uniaxial stress of the opposite sign and perpendicular to the interface.⁵⁶ If the lattice constant of the layer is larger than that of the substrate then for the layer the hydrostatic component of the strain is compressive and the uniaxial component is tensile.

Figure 15 shows the spectra obtained for the gold acceptor $\text{Au}(-/0)$ state in two different SiGe (2% of Ge) samples grown by MBE on a silicon substrate (see Ref. 57 for the growth details). For one of the samples the misfit strain has been partially released by growing a thick buffer with graded alloy composition. The other one has been grown without such a buffer, however, the layer thickness is below the critical thickness for this alloy composition, i.e., the strain has not been released by misfit dislocations. The samples have been mounted and measured together in the same cryostat to minimize the temperature error⁵⁸ and for both recorded spectra the pattern of peaks is the same and can be attributed to the effects of alloying (see Sec. V for further details).⁵⁹ All peaks of the strained sample are shifted towards higher emission rates and this cannot be explained by a temperature error which would have to be of the order of 9 K and this is impossible with the experimental setup. Samara and Barnes⁶⁰ using conventional DLTS have demonstrated that the appli-

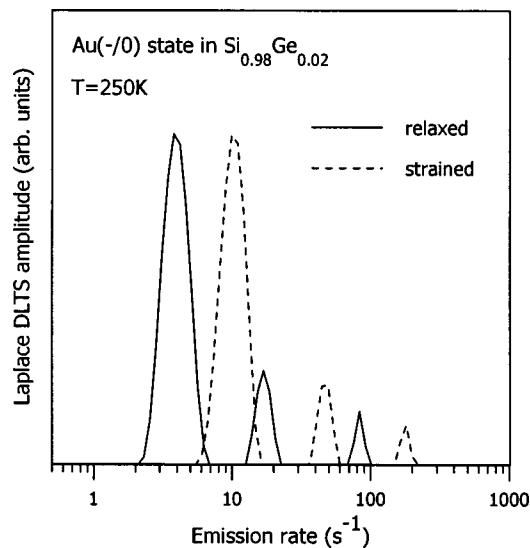


FIG. 15. Two spectra demonstrating the alloy splitting effect for the Au(-/0) acceptor state in SiGe (2% of Ge) for the relaxed (solid line) and strained (dashed line) MBE-grown layer (Ref. 58).

cation of hydrostatic pressure reduces the activation energy for the thermal emission process for the Au(-/0) level in silicon with the pressure coefficient of 26 meV/GPa with the pressure having practically no influence on the capture process. Analogously, in the present case if the peak shift is caused by the planar strain then assuming negligible influence on the capture cross section the observed shift corresponds to a reduction of the activation energy for emission of 20 meV. According to the elasticity theory for cubic defects in diamond-structure crystals⁶¹ only 2/3 of the strain is used for the volume compressibility. Consequently, combining results it is easy to show that the measured peak shift corresponds to the linear stress of 0.58 GPa, which using the linear compressibility of silicon ($3.4 \times 10^{-3} \text{ GPa}^{-1}$), translates to the linear strain of 1.8×10^{-3} .

In comparison, Vegard's law predicts using the lattice parameters of silicon and germanium that for a 2% SiGe alloy the lattice constant should be larger than for the pure silicon by a factor of 8.5×10^{-4} . The epitaxial growth of a strained 2% SiGe alloy layer on a silicon substrate implies that the lattice of the layer is subjected to this strain. The estimation of the strain from the shift of the Au(-/0) level is larger than that derived from Vegard's law by a factor of 2. This apparent discrepancy may be explained by the preference of Au to occupy a site near germanium in the random alloy (see Sec. V B 1 for details). The overpopulation amounts to about a factor of 2 for diffusion at 800 °C, which means that locally around gold the germanium content is twice the alloy average. Although one cannot conclude unambiguously that this alloy fluctuation converts directly to locally increased strain, it seems justified to conjecture that the gold atoms sitting in more germanium-rich regions may experience a larger average strain than that predicted from Vegard's law.

Figure 16 shows a different example of the effect of strain on the thermal emission process.⁶² The figure shows the Laplace DLTS spectra obtained for three Si and SiGe

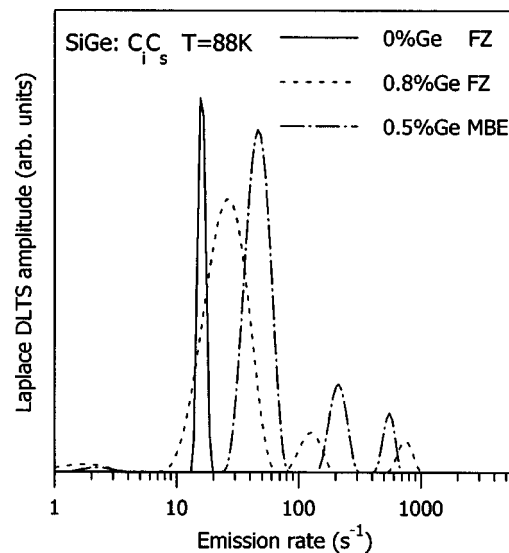


FIG. 16. The Laplace DLTS spectra of the C_i-C_s pair observed in the FZ silicon (solid line), FZ SiGe (0.8% of Ge) (dashed line), and the MBE-grown strained SiGe (0.5% of Ge) (dotted-dashed line) samples (Ref. 62).

n-type carbon-rich samples irradiated with 2 MeV electrons at 60 K. After irradiation the samples were annealed for 10 min at 300 K. It is known that this procedure leads to formation of the carbon (interstitial)-carbon (substitutional) (C_i-C_s) pair in silicon.^{63,64} A similar pair formation has also been observed for SiGe alloys.⁶⁵ The (C_i-C_s) defect has two different configurations and the spectra presented in the figure correspond to the stable configuration of the pair.⁶⁴ The samples used for these measurements were a slice of float-zone (FZ) grown silicon and a slice cut from a FZ ingot of SiGe (0.8% Ge), the third sample was a SiGe strained layer (0.5% of Ge) grown by MBE on a silicon substrate. In each of the alloy spectra there is one main peak and some subsidiary peaks. For the two bulk crystal samples the main peaks are shifted slightly relative to each other with clear broadening observed for the SiGe alloy. The shift is due to the band-gap modification by alloying. The MBE SiGe sample contains less germanium than the SiGe FZ crystal. However the main peak does not appear between the main peaks of the bulk samples. It is shifted towards higher emission rates. Note that both SiGe samples were measured in the cryostat side by side to avoid any possible temperature differences so the shift is real. We infer that strain in the MBE SiGe sample is the reason for the main peak shift.

Unfortunately, for this case a quantitative strain analysis is not possible. First, data of the C_i-C_s level hydrostatic pressure dependence is not available. Second, this defect in the stable configuration has monoclinic symmetry⁶⁴ which means that the hydrostatic compressive strain combined with the tensile uniaxial strain perpendicular to the interface (the $\langle 100 \rangle$ direction) will not only shift the main peak of the MBE sample but will cause splitting as well. The fact that much larger secondary peaks are observed for the MBE sample than for the FZ sample could possibly result since peak splitting overlaid the alloying effect.

2. Electric-field effects

The charge state of a defect cannot be determined directly by the DLTS technique although it can sometimes be inferred from the magnitude of the capture cross section. For defects in the space charge region the emission process of electrons or holes occurs in the presence of the electric field. The field may enhance the emission process and the presence and strength of this enhancement may depend on the defect charge state. A number of theoretical models has been developed to help the quantitative analysis of this effect, if present.^{66–71} In practice, the thermal emission enhancement process is discussed within two different types of models depending, basically, on the value of the electric field. In the low- (around 10^3 V/cm) and medium-electric-field regimes the effect is discussed in terms of the three-dimensional^{67,68} and one-dimensional Poole-Frenkel model,^{66,69} respectively. For very strong electric fields (larger than 10^5 V/cm) it was found that a direct or phonon-assisted^{68,69,71} tunneling process can dominate.

In the space charge region of an ideal Schottky or *p-n* junction the electric field is not homogeneous and changes linearly from a maximum value at the junction to zero at the space charge edge. Thus defects investigated by the DLTS technique experience different electric fields depending on their position in the space charge region. When the emission process is field dependent then the rate constant is not a unique feature and even conventional DLTS peaks may show broadening.

The common way to minimize this broadening is to observe the emission process only from a narrow region of the space charge region. In this case two filling pulses of different voltages are applied and the signals following each of them are subtracted (see, e.g., Ref. 72 for an example of this approach). If the difference between the pulse heights is small the observed defects are in a fairly constant electric field. In many cases this so-called differential or double DLTS method enables a quantitative analysis of the influence of the electric field on the emission process.

Figure 17 shows results obtained with the differential method when applied in combination with Laplace DLTS.⁷³ The samples were GaAs:Si n-type crystals irradiated with alpha particles. Two main irradiation-related defects assigned as Ea3 and Ea4 are observed in the samples. The Ea3 center exhibit metastability as shown previously by conventional DLTS.⁷⁴ It has also been found that the electric-field affects the emission process of the two centers differently,⁷⁵ the LDLTS data clearly confirm this very directly.

The differential mode does not assure that the electric field is perfectly homogeneous in the space from where the LDLTS signals originate, and presumably for this reason the main peaks in the spectra of Fig. 17 are still broadened. The markers show the positions on the emission-rate scale of the main peaks' centers of gravity. Clearly, when the spectra are taken with the defects at a high electric field (large filling-pulse voltage) the Ea4 emission peak shifts towards higher emission rates, whereas the Ea3 peak does not shift. These different responses to the electric field clearly demonstrate that the observed shift is a genuine effect related to the defect structure and, hence, not sample dependent as has been dem-

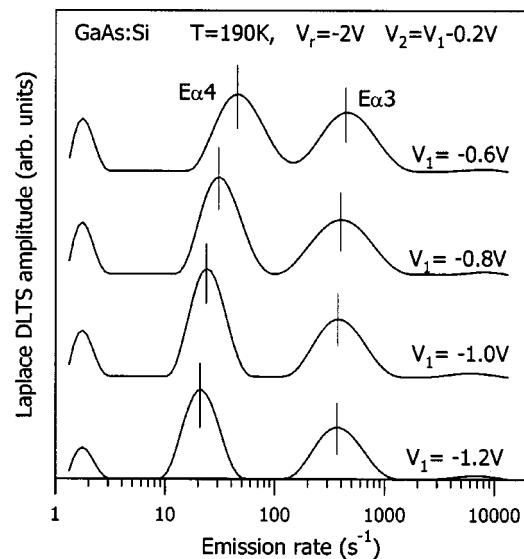


FIG. 17. A series of the Laplace DLTS spectra taken at different electric fields (in the differential mode) for the α -particle irradiated sample of GaAs:Si. The electric field (it is the lowest for the bottom spectrum) increases the emission rate for the Ea4 defect, while for the Ea3 defect the effect is very weak (Ref. 73).

onstrated in Ref. 76 for other cases as well. Similar unequal behavior of different defects observed in the same sample has been demonstrated also with the use of conventional DLTS for cases (E3 and EL2 in GaAs) where the signals could be easily resolved.⁷⁷

The problem of the space charge electric-field gradient is less severe when the investigated defects are localized in a narrow strip parallel to the junction. This is typical for defects formed when the atoms of small mass are implanted directly into a diode structure. The implants penetrate the crystal to a depth that depends on the implantation energy and are concentrated in the straggling region at a well-defined distance from the sample surface. This procedure has been used to study defect related to the low-temperature low-energy implantation of hydrogen into Schottky diodes deposited on germanium crystals.⁷⁸ In this case the straggling is about $0.25\ \mu\text{m}$ with the consequence that hydrogen related defects generated in the space region experience almost the same electric field. As a result, the inhomogeneous broadening associated with an electric-field enhancement of emission rates will be minimal.

Figure 18 shows shifts of the LDLTS peak originating from bond-center hydrogen in germanium H(BC) for spectra taken with increasing reverse bias. The inset shows the capacitance-voltage profile for the sample where the depth scale (*x* axis) is replaced by the bias voltage. The dashed line represents the profile before the implantation and the solid line depicts the situation immediately after implantation. The induced defects partially compensate the shallow donors, which results in the appearance of a dip in the carrier profile. In the case shown the dip is located at a distance of $2.8\ \mu\text{m}$ from the crystal surface (the implantation energy was 580 keV) and the apparent width is around $0.4\ \mu\text{m}$. This distance corresponds to a sample bias of -2.5 V. When the filling voltage is kept at to -2 V and the reverse bias is

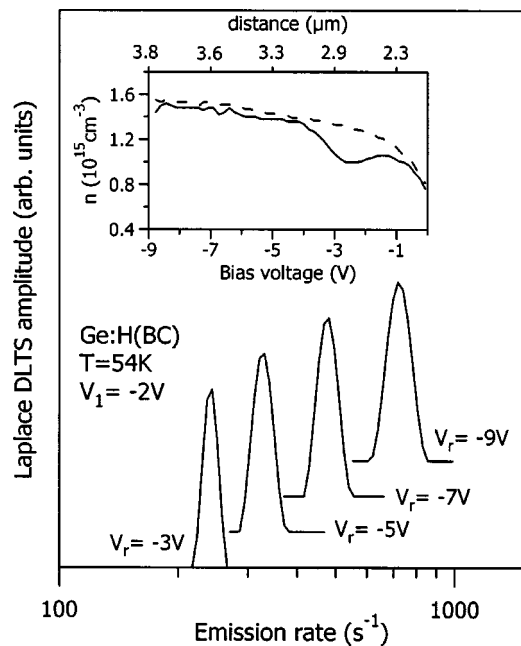


FIG. 18. A shift of the Laplace DLTS peak attributed to the bond-centered hydrogen in germanium. The spectra were taken at different reverse biases. The inset shows the CV profiling of the sample shallow donors before (dashed line) and immediately after (solid line) the hydrogen implantation of the sample with the energy of 580 keV. The dip in the profile indicates that hydrogen atoms are localized in a narrow region of the space charge region. (Ref. 78).

increased from -3 to -9 V then all defects located $2.8 \mu\text{m}$ from the junction experience the same increasing electric field. The depicted emission-rate increase is characteristic of the Poole-Frenkel effect for a singly charged deep donor. Note that the overall shift of the H(BC) peak corresponds to an increase of emission rate by only a factor of 3, which is well within the width at half maximum of a conventional DLTS peak.

The introduction of defects at a well-defined spatial position in the space charge region, which translates to a specific electric field, can in principle be used for tracking the diffusion of defects. The Laplace DLTS peaks shown in Fig. 18 are rather narrow demonstrating that the initial spatial spread is small, and the electric field therefore is almost constant. A subsequent diffusion process will result in an increased spread and, in consequence, broadening of the emission peak. This application of Laplace DLTS is demonstrated and discussed in detail in Ref. 79 for the case of H(BC) in silicon.

IV. APPLICATIONS OF LAPLACE DLTS WITH UNIAXIAL STRESS

A. Introduction

The current standing of deep-level transient spectroscopy as one of the major tools for studies of electrically active defects in semiconductor materials has been attained not least because of the high sensitivity of the technique. As discussed previously the major deficiencies are the lack of structural information and limited spectral resolution. As a consequence structural and compositional characterization of

a deep-level defect must rely on the correlation of formation and annealing properties of the defect with data obtained with other spectroscopic techniques such as electron paramagnetic resonance (EPR) and infrared absorption (IR). Both these structure-sensitive techniques have been combined with uniaxial stress to elucidate structural properties in further detail. Good examples are the study of reorientation kinetics after stress alignment in EPR and the distinction between alternative defect configurations by local-mode IR spectroscopy under stress. The total number of defects needed (and allowed) in DLTS is for a typical case several orders of magnitude less than the corresponding number needed in EPR and IR. With such large span in defect density it may often be ambiguous or even impossible to establish the geometric and electronic structure of a particular deep-level defect by just relying on comparison of annealing data. In this perspective it would obviously be of great advantage to make DLTS provide structural information in its own right. Recording the thermal emission while uniaxial stress is applied along specific crystal directions can accomplish this because the imposed external force on the crystal causes the emission to split into components and thereby exposes the latent anisotropy associated with the orientational degeneracy of the defect.

This possibility of obtaining the local-symmetry information by the combination with uniaxial stress was realized to some extent in the early years of deep-level transient spectroscopy. However, only a few studies that actually revealed structural information have been carried out with the application of conventional DLTS. A reason for this may be found in the rather limited emission-rate resolution. The key issue is to achieve separation of the individual emission-rate components and with limited resolution the separation can be achieved only in favorable cases. With the implementation of Laplace DLTS this resolution restriction has been lifted to a certain degree and the number of cases accessible for studies increased correspondingly. In Sec. IV D we shall discuss a selection of such studies in some detail in order to demonstrate the potential for combination of DLTS with uniaxial stress but also to expound limitations and pitfalls. However, first we shall review in Sec. IV C some related (earlier) stress work where the limited resolution was not a major concern. These works include DLTS measurements under hydrostatic pressure and include also uniaxial-stress measurements designed to study the effect of stress on band edges and therefore relying on test cases with negligible splitting. To establish a framework for discussions we shall begin with a brief outline in Sec. IV B of the basic principles for interpretation of DLTS stress data.

B. Interpretation of stress data

1. General formulas

Rigorously, the position of an electronic band-gap level relative to either the conduction-band edge (c) or the valence-band edge (v) is defined as the energy difference

$$\Delta E_{c,v} = E(F, Q_F) + E(e_{c,v}) - E(I, Q_I), \quad (8)$$

where $E(F, Q_F)$ and $E(I, Q_I)$ are the total energies of the defect in its final and initial charge states, respectively, expressed in terms of the generalized equilibrium lattice coordinates Q_F and Q_I , and where $E(e_{c,v})$ is the energy of either an electron at the bottom of the conduction band or a hole at the top of the valence band. In DLTS the determination of ΔE_c or ΔE_v for a particular level relies on measuring the rate of thermal carrier emission from the level, e_n or e_p , respectively. Lang *et al.*⁴¹ showed on the basis of work of van Vechten and Thurmond⁸⁰ and Engström and Alm⁸¹ that the proper forms of the well-known detailed balance equations (introduced in Sec. I A) combining thermal capture and emission are

$$e_{n,p} = \sigma_{n,p} \langle v_{n,p} \rangle N_{c,v} \exp(-\Delta G_{c,v}/k_B T). \quad (9)$$

In this equation $\sigma_{n,p}$, $\langle v_{n,p} \rangle$, and $N_{c,v}$ are capture cross sections, mean thermal velocities, and the effective density states for the pertinent carriers and bands. The term $\Delta G_{c,v}$ occurring in the Boltzmann factor is the change in Gibbs free energy associated with the emission and is related to the level energy $\Delta E_{c,v}$ of Eq. (8) by the standard thermodynamic relation $\Delta G = \Delta E + p\Delta V - T\Delta S = \Delta H - T\Delta S$. It is ΔH , the change in enthalpy, that can be determined from an Arrhenius plot and a rigorous determination of an energy level therefore requires knowledge of the volume change of the defect as a result of the emission. In practice the distinction between ΔH and ΔE is seldom made because the $p\Delta V$ term is extremely small except for very high pressures (~ 10 meV at 1 GPa). Nevertheless ΔV contains important structural information and may be derived from stress measurements.

Equations (8) and (9) show that only the energy level and possibly the capture cross section may be obtained from a standard DLTS measurement subject to the limitations discussed in Sec. I A. No information with regard to the symmetry of the wave function is imparted. This limitation of DLTS can be removed (at least in principle) when measurements are carried out with samples subjected to uniaxial stress. The stress deformation potential may be taken to be linear in relation to the applied force and consequently also linear in relation to the imposed strain on the defect. Mathematically the effect of applied stress therefore may be expressed in terms of partial strain derivatives that are related in accordance with Eq. (8) by expressions of the form:

$$\begin{aligned} \partial \Delta E / \partial \epsilon_{ij} = & \partial E(F, Q_F) / \partial \epsilon_{ij} + \partial E(e_{c,v}) / \partial \epsilon_{ij} \\ & - \partial E(I, Q_I) / \partial \epsilon_{ij}. \end{aligned} \quad (10)$$

In these expressions the right side middle terms are the constants entering in the band-edge deformation potential. For the definition of the strain tensor $\{\epsilon_{ij}\}$ and further details regarding deformation potentials see, e.g., the review by Ramdas and Rodrigues.⁸²

2. Defect symmetry from level splitting

As Eq. (10) indicates that the measured shifts in level energies involve band-edge terms and consequently a complete absolute piezospectroscopic analysis of the stress re-

sponse of the individual defect charge states is usually prohibited. This is true even when possible stress dependencies of the preexponential factors of Eq. (9) can be neglected. What can usually be determined rather directly by the application of uniaxial stress is the structural symmetry i.e., the point symmetry associated with the different possible spatial orientations of an individual anisotropic defect center. Without stress the anisotropy remains latent because of the orientational degeneracy, ensured by the overall random distribution of the center throughout the host crystal. The stress exposes the latent asymmetry by lifting the orientational degeneracy shown as a splitting of the thermal emission into a characteristic pattern from which the point group symmetry of the particular defect may be derived. It is to be understood that unless the point symmetry of the initial and final state is identical it is the initial-state symmetry that is determined (see further discussions in Sec. IV B 4). This is in contrast to stress splitting of optical transitions where the splitting of both initial and final states may be revealed. The only requirement for successful determination of the initial-state symmetry is sufficient emission-rate resolution and the possibility of choosing the measurement temperature so that thermal jumps between different orientational configurations of the defect do not occur when stress is applied. In this case the number of emission-rate components, with their (saturated) relative intensities in accordance with purely statistical population of the individual orientations of the defect, uniquely determines the initial-state point symmetry. Even when the intensities of the stress split components do not appear with proper statistical weights this does not necessarily impede the determination of the symmetry. This is because the departure from random population only indicates that some preferential alignment occurs at the measurement temperature at a rate slow compared to the rate of carrier emission. However, care must be exercised to make sure that no component is entirely missing. Note also in this context that the revealed symmetry could in principle be an apparent symmetry. This would happen when a swift thermally stimulated ionic reconfiguration of a defect generates an “effective” symmetry element. In this case when the reconfiguration rate is much larger than the emission rate [Eq. (13)] the point symmetry will appear to be higher than the true “ionic” symmetry at low temperature.

So far we have neglected the possibility that emission-rate patterns may be influenced by, or even originate from the lifting of a possible electronic degeneracy associated with the defect level in question. This presents the problem of distinguishing, from the emission data, between the electronic degeneracy characteristic of a defect with high symmetry and the orientational degeneracy characteristic of a defect of low symmetry. The key to achieve this lies in the difference in the dynamical behavior in the two cases. As discussed above, when stress is applied to an orientational degenerate system the populations initially attain the statistical weights of the unstressed system. These may then slowly (i.e., hindered by impeding thermal barriers) approach and eventually reach the Boltzmann populations of a system in thermal equilibrium for the given stress splitting (see Sec. IV B 3 for further details). In practical work the temperature

may often be chosen so low that the initial populations are maintained during measurement. This is entirely different from what is expected for an electronically degenerate system. Here the Boltzmann populations corresponding to the stress splitting would be attained rapidly and since the range of resolvable splitting typically encompass the Boltzmann energy $k_B T$ of the measurement the population changes as a function of stress should readily reveal the effects of electronic degeneracy.

Taking the precautions listed into account it is straightforward to obtain the point symmetry of a deep-level center with the carrier in its bound state. In this perspective alone uniaxial-stress DLTS becomes a valuable tool for structural identification of electrically active semiconductor defects. All the specific examples given later in this chapter on the application of Laplace DLTS deal with orientational degenerate systems.

3. Piezospectroscopic parameters from alignment studies

It is obvious from inspection of Eqs. (8)–(10) that the inference of independent stress derivatives for either of the two charge states of the defect cannot be obtained even if the contributions involving the band edge can be dealt with properly. We shall return to this matter later on. In this paragraph we limit the discussion to analyzing the prospects for drawing conclusions about the stress derivatives from alignment studies. First we introduce the basic concepts for piezospectroscopic analysis of stress data for which the work of Kaplyanskii⁸³ laid the theoretical foundation. The deformation potential U_a , labeled according to the orientation of the defect with respect to the stress direction, is expressed either in terms of the piezospectroscopic stress or strain tensors $\{A_{ij}\}$ or $\{B_{ij}\}$ as

$$U_a = \sum A_{ij} \sigma_{ij} = \sum B_{ij} \varepsilon_{ij}, \quad (11)$$

where $\{\sigma_{ij}\}$ and $\{\varepsilon_{ij}\}$ are bulk stress and strain tensors, respectively. See, e.g., Refs. 61 and 82 for details. From inspection of Eq. (10) it follows that B_{ij} for the initial and final charge state of a defect correspond to $\partial E(F, Q_F)/\partial \varepsilon_{ij}$ and $\partial E(I, Q_I)/\partial \varepsilon_{ij}$, respectively. In an alignment study samples are directionally stressed at a high temperature to attain equilibrium populations of the individual defect orientation under stress and then rapidly quenched to low temperature to freeze this population. In this way the deviation from the random population can be utilized to partly determine either of the two piezospectroscopic tensors, $\{A_{ij}\}$ or $\{B_{ij}\}$. This result follows from pairwise comparison of the populations n_a and n_b via the Boltzmann relation

$$n_a/n_b = \exp - (U_a - U_b)/k_B T. \quad (12)$$

In this expression the hydrostatic (trace) component of the piezospectroscopic tensor always cancels, hence only the shear (traceless) part of the tensor can be obtained. Any kind of measurement technique where Eq. (12) can be utilized can help in modeling a defect. Among the first successful applications were the celebrated modeling by Watkins and Corbett⁸⁴ and Corbett *et al.*⁸⁵ of vacancy-oxygen center (VO)

in silicon by EPR and local-mode IR spectroscopy. The center was studied also in early applications of hydrostatic and uniaxial-stress DLTS by Samara⁸⁶ and by Meese, Farmer, and Lamp,⁸⁷ respectively. The comparison of VO stress data from different experimental techniques reveals features in analysis and interpretation that may be considered as textbook examples. We shall review the VO material as such in Sec. IV D and address in particular an additional bonus that can be drawn from alignment studies, namely, the exploration of saddle points for reorientation processes utilizing Laplace DLTS.⁸⁸ A particular useful feature of uniaxial-stress DLTS as compared to other techniques is the simple property that alignment may be achieved in either of the two charge states involved [see Eq. (8)] just by carrying out the alignment procedure with or without bias applied to the diode.

4. Piezospectroscopic parameters from level splitting

It follows from Eqs. (8)–(10) that when the applied stress lifts orientational degeneracy and thereby causes the emission signal to split according to the number of non-equivalent defect orientations the stress derivatives may, in principle, be obtained from the slope $\ln(e_{n,p})$ versus pressure. There are limitations, which we shall now discuss.

First we consider the ideal situation when the stress dependence of the preexponential factor can be neglected. We further assume identical symmetry of the initial and final states. In this case the shear components of the piezospectroscopic “difference” tensors, $\{A_{ij}^F - A_{ij}^I\}$ or $\{B_{ij}^F - B_{ij}^I\}$, are the quantities obtained. As long as we are not concerned with the hydrostatic part of the tensors the band-edge derivatives need not be considered as they are common to the members of the split pattern for a given applied stress direction. It has to be understood that, depending on the defect symmetry, data for two or three stress directions (typically $\langle 100 \rangle$, $\langle 110 \rangle$, and $\langle 111 \rangle$) are needed for a complete determination of the shear components.

To determine the hydrostatic component one has to rely on the extraction of the absolute shifts of individual split emission lines or preferably extract the hydrostatic shift from measurement under hydrostatic pressure. However, for making these extractions one must know the deformation potential of the band edge in question. Whereas the shear parameters of this potential are often available the hydrostatic parameter is normally known only for the band gap and not for individual bands. One may further envisage cases where the initial and final states have a different symmetry. In this case the concept of a “difference tensor” becomes inconvenient or even meaningless and the analysis obviously becomes much more complicated. Furthermore, the implied lattice relaxations may suggest that stress dependencies of the capture cross sections could be significant.

We mentioned earlier that the symmetry read from split patterns could be misleading and represent an effective symmetry caused by rapid ionic relaxations. If, for example, in a monoclinic center an ion can jump between two positions in the symmetry plane an effective orthorhombic center may result when the jump rate is larger than the emission rate. Still one would from an electronic point of view say that the

true symmetry is monoclinic because the stress response must be evaluated as an average over two monoclinic orientations rather than a center with the jumping ion in its average position. To treat a situation like this one may introduce the effective emission rate e_{eff} determined by DLTS and relate it to the stress derivatives. Denoting the rate constants for jumps between the two orientations (a) and (b) by λ_a and λ_b we get

$$e_{eff} = [e_a(1 + \lambda_a/\lambda_b)^{-1} + e_b(1 + \lambda_b/\lambda_a)^{-1}], \quad (13)$$

under the condition $\lambda_{a(b)} \gg e_{a(b)}$ and quasidetached balance $\lambda_b N_b(t) = \lambda_a N_a(t)$. Using this formula “theoretical emission rates” may be derived from the calculated stress derivatives for direct comparison with experimental rates.

5. Stress dependence of preexponential factors

In the previous discussion we neglected the possible role that stress dependence of the preexponential factor may play. There are several causes for such dependencies. The most obvious one is that the capture matrix element may have a direct stress dependence. Then, in the framework of the deformation-potential concept, it is justified to assume linearity to first order with the consequence that the imposed effect on the emission rate [Eq. (9)] would be rather weak. The argument for this is that the cross section enters as a logarithmic term as compared to the energy shift unless the capture process is thermally activated, in which case a linear response of the barrier to stress will contribute on the same footing as the level shifts. The modeling of capture barriers is very complicated, and even more so for capture under stress. Henry and Lang³ developed a semiclassical model for thermally activated multiphonon capture. However, as pointed out by Ridley⁸⁹ the absence of a barrier does not imply that multiphonon capture is not the dominating process. Quantum modeling shows that multiphonon processes may occur without the presence of a thermal barrier. Hence multiphonon processes may be active at all temperatures even when the semiclassical approach fails. Basically, the only way to deal fully satisfactorily with the interpretation of the stress-induced emission-rate shifts in terms of level shifts is to actually measure the full stress dependence of the capture cross section. This is particularly important when it is suspected that a large lattice relaxation may be linked with the emission process. The fingerprint of this would be the presence of a capture barrier at zero stress and possibly the induction of a capture barrier by the stress itself. However, even when the absence of any barrier indicates that the direct impact of the capture process may be neglected capture-rate phenomena related to the lifting of degeneracy of band-edge extremes under stress cannot always be disregarded. This is because the emission constant [Eq. (9)] separates into components with individual and possibly very different preexponential factors.

A phenomenon of this kind related to the splitting of the light-and heavy-hole valence bands was discussed by Nolte and Haller.⁹⁰ In this case the significance of the effect is caused by the large difference in the effective masses of the two bands. Another somewhat analogous phenomenon could arise if the matrix element for capture into a highly aniso-

tropic defect of a fixed orientation with respect to the cubic axes of the semiconductor crystal would depend on which k -space valley the capture originates from. It would be thought that this would appear to be rather insignificant for a deep level, as one would expect such valley dependence of capture matrix elements to be minute because of the extension of the wave function in k space. However, as we shall discuss further in Sec. IV D 4, this kind of the anisotropic capture may explain the anomalous nonlinear stress dependence of the emission from the vacancy-oxygen center VO.

C. Early DLTS stress work

1. Hydrostatic pressure applications

With reference to the outline in Sec. IV B we may consider the application of hydrostatic pressure as equivalent to simultaneous application of equal stress along the three cubic axes [100], [010], and [001] of the semiconductor crystal causing a volumetric change of the defect. Obviously no orientational splitting (or for that matter any lifting of electronic degeneracy) can be observed. The implication is that only the trace in the piezospectroscopic tensor, $\{A_{ij}\}$ or $\{B_{ij}\}$, is obtained under this condition. A substantial number of hydrostatic-pressure DLTS studies have been reported in the literature. Because only line shifts are involved the need for high resolution is important only in the case of unresolved emission signals in conventional DLTS. Such cases are undoubtedly plentiful. However, we shall restrict ourselves in this review to discuss a few selected examples which serve to illuminate basic concepts of DLTS stress measurements, or which relate to the specific Laplace DLTS studies reviewed in Sec. IV D.

Among the early hydrostatic-pressure studies are the work of Jantsch *et al.*⁹¹ who measured the pressure coefficients of the A and B levels in silicon of S, Se, and Te and found values comparable to those of the energy gap and about 100 times larger than those expected for effective-mass shallow levels. The authors pointed out that the size of the pressure coefficient may be taken as an alternative (or better) criterion for classification of a level as being deep as opposed to shallow. The point made was that the short-range defect potential imparts a localization of the trap wave function that is not necessarily reflected in the level energy.

A detailed hydrostatic-pressure investigation of the VO-acceptor level in silicon was reported by Samara⁸⁶ and Samara and Barnes⁹² following up on earlier work by Keller.⁹³ In the context of the present review we take a particular interest in the work of Samara, which contributes important information to our understanding of the physical properties of the VO center. We duplicate some of the figures presented in Ref. 86 for further consideration in Sec. VI D in conjunction with the interpretation of VO uniaxial-stress data. Figure 19 depicts the pressure dependence of the activation enthalpy ΔH indicating the relative position of the level in the gap as pressure increases. Figure 20 demonstrates the independence of the capture cross section of temperature and pressure, and Fig. 21 depicts the derivation of the volumetric compression accompanying the electron emission from the VO acceptor.

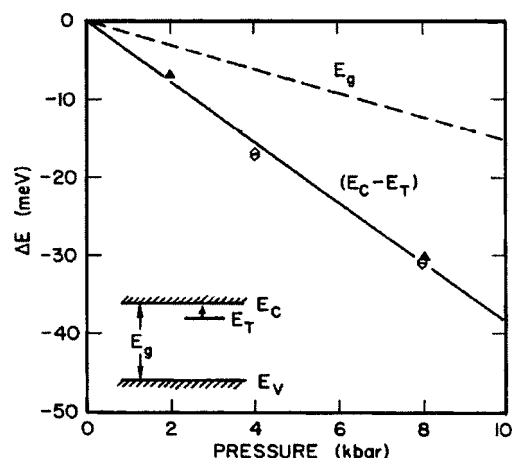


FIG. 19. Reproduced from Samara (Ref. 86). Hydrostatic pressure dependence of the activation energy $E_c - E_T$ (or ΔH) for the vacancy-oxygen center VO in silicon compared with that of the energy gap E_g . The insert depicts the fact that the VO level moves closer to the conduction band (and farther from the valence band) with pressure. From the graphs it can be deduced that E_T moves away from the valence-band edge at a rate of 24 meV/GPa.

In addition transition-metal levels have been subjected to extensive pressure studies, Li *et al.*,⁹⁴ Stöffler and Weber,⁹⁵ and Samara and Barnes.⁶⁰ The celebrated $E_c - 553$ meV mid-gap acceptor of Au in silicon was studied under hydrostatic pressure in Refs. 60 and 94. Figure 22 is reproduced from Ref. 60 and illustrates the experimental determination of $(\partial \Delta G / \partial p)_T = \Delta V$ analogous to the VO case. The work of Ref. 60 further includes a comparison of the Au stress derivatives with measured derivatives for the shallow level of the As-doped sample with results that fully corroborates the analogous results of Ref. 91. Reference 95 reported the hydrostatic pressure coefficients for the $E_c - 235$ meV acceptor and $E_v + 320$ meV donor levels of substitution-site Pt in silicon. The negative sign of the two pressure coefficients shows

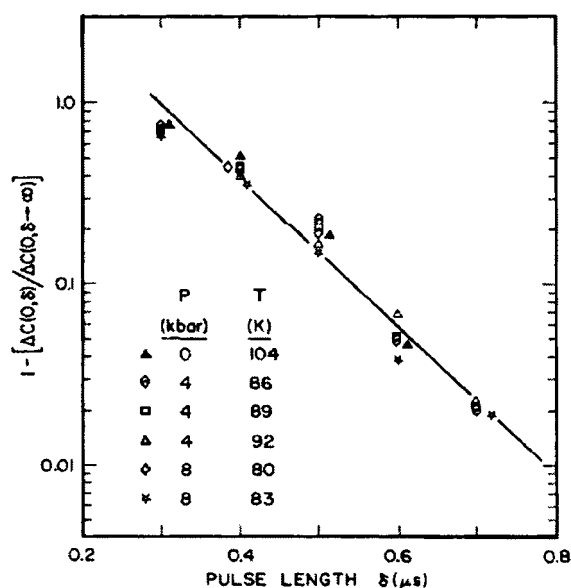


FIG. 20. Reproduced from Samara (Ref. 86). Demonstration of temperature and pressure independence of electron capture to the VO acceptor level in silicon. The initial capacitance amplitude as a function of filling-pulse duration is shown.

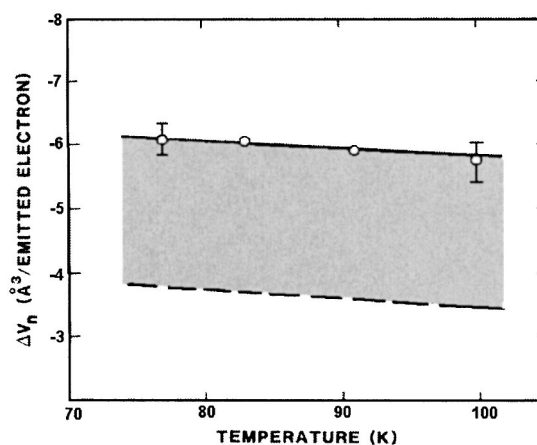


FIG. 21. Reproduced from Samara (Ref. 86). Demonstration of the inward volumetric lattice relaxation accompanying electron from the VO acceptor level in silicon. The upper bound corresponds to the limit where the pressure-induced shift of the gap is taken up entirely by the valence-band edge with the conduction-band edge remaining fixed. The lower bound corresponds to the reverse situation. The average magnitude of the volumetric relaxation corresponds to an inward relaxation of the near-neighbor Si atoms to the VO pair of 0.07 Å. This estimate is based on the assumption that the relaxation is taken up by the first shell of Si atoms alone and therefore represents an upper limit.

that both levels shift towards their respective reference bands highlighting the deep-level character that the wave functions of the bound carrier are not composed of the wave function of the reference band. Remarkably, then the pressure coefficient of the $(0/+)$ donor level is very close to that of the band gap indicating that the level shifts almost parallel to the edge of the conduction band. Whether this is fortuitous or not it accentuates that a wealth of structural information is embedded in stress data.

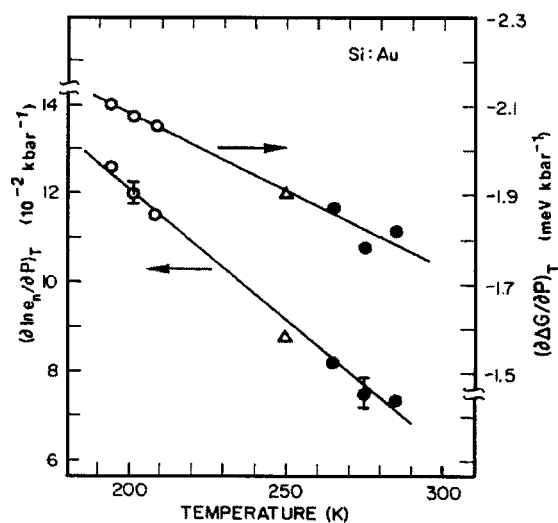


FIG. 22. Reproduced from Samara and Barnes (Ref. 60). Temperature dependence of the logarithmic pressure derivative of the emission rate and the pressure derivative of the Gibbs free energy ΔG needed to emit an electron from the Au acceptor level in silicon. When corrected for the contribution from the band edge. (cf. Fig. 21) the isothermal pressure derivative of ΔG measures the breathing mode lattice relaxation of the defect which accompanies the emission.

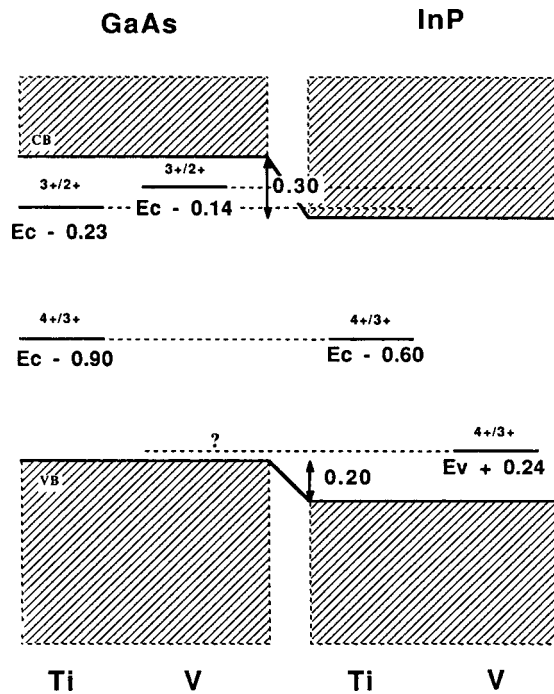


FIG. 23. Reproduced from Nolte, Walukiewicz, and Haller (Ref. 96). The figure illustrates the basic concept for obtaining individual band edge deformation potentials. The line up of the transition-metal levels across the band-gap offset between GaAs and InP is shown. By analogy a similar offset will occur across a strain-induced homojunction in which case the individual shifts of band edges are directly proportional to the corresponding deformation potentials. The conduction-band potential was obtained from measured stress derivatives of the $(3+/2+)$ Ti and V levels in bulk GaAs and the $(4+/3+)$ Ti level in bulk InP. The valence-band potentials were derived by subtraction of band-gap potentials.

2. Band-edge deformation potentials and absolute pressure derivatives

In general the hydrostatic pressure derivative of a defect level cannot be discerned from the derivative of the pertinent reference band since only derivatives for the band gap can be obtained by direct spectroscopic means. Hence, experimental determinations of band-edge deformation potentials must rely on model-dependent analysis of experimental data. Nolte, Walukiewicz, and Haller⁹⁶ carried out such analysis for GaAs and InP. Their analysis rests on suggestions by Caldas, Fazzio, and Zunger⁹⁷ and Langer and Heinrich⁹⁸ that transition-metal deep levels can be used as the stable reference that lines up across an interface between two isovalent semiconductors.

An analogous lineup holds also for a strain-induced homojunction where the band offsets at the interface are directly proportional to the band-edge deformation potentials. As a consequence it was conjectured that measuring the stress derivative of the transition-metal defect level is, in fact, a direct measurement of the stress derivative of the pertinent band-edge deformation potential of the bulk material. Figure 23 reproduced from Ref. 96 indicates the essentials of the experimental analysis. The stress derivatives of Ti($4+/3+$) and V($4+/3+$) levels were obtained by DLTS under uniaxial stress and found to be essentially equal yielding for GaAs the pressure derivatives (per unit strain) $a_c = -9.3 \pm 1$ eV for the conduction band, and by subtracting

the band gap the corresponding value for valence-band $a_v = -0.7 \pm 1$ eV. For InP the corresponding values $a_c = -7 \pm 1$ eV and $a_v \approx 0.6$ eV were obtained from the stress dependence of the Ti($4+/3+$) donor level. The application of uniaxial stress to obtain the hydrostatic stress derivatives implies that small and unresolved shear stress contributions to energy shifts have to be neglected in the analysis. However, the deformation potential values so obtained corroborates theoretical results by Van de Walle and Martin.⁹⁹ The foundation for the use of transition-metal levels as reference levels for obtaining band offsets has been substantiated further by subsequent theoretical work of Hamera *et al.*¹⁰⁰

Taking advantage of these derived band-edge potentials Nolte, Walukiewicz, and Haller¹⁰¹ obtained absolute values for the change in stress derivatives under carrier emission for the EL2 and EL6 centers in GaAs. This work is a perfect example of the potential for (but also the difficulties in) deriving structural information from uniaxial-stress measurements. For $(0/+)$ EL2 ($E_c - 820$ meV) it was concluded that the electron-lattice interactions must be large with the four nearest neighbors to explain the large change in isotropic strain upon electron emission (~ 90 meV/GPa), yet the strength of the interaction with the individual neighbors must be small to explain the lack of strain anisotropy (< 5 meV/GPa). More recently Bliss *et al.*¹⁰² extended the uniaxial-stress work to the second ionization level of $(++/+)$ EL2 ($E_v + 520$ meV) observed in p -type GaAs and found a pressure derivative that is more than a factor of 2 less than that of the $(0/+)$ level with no orientational dependence. In order to compare the stress derivatives for the two cases in a consistent way one has to consider that the contributions from capture barriers may differ significantly. For the $(++/+)$ level no significant dependence of the hole capture barrier was found whereas for the $(0/+)$ level mutually inconsistent results have been reported. Dobaczewski and Sienkiewicz¹⁰³ found no barrier and Dreszner and Baj¹⁰⁴ found a substantial barrier. If the latter result is utilized to extract the pressure dependence of the $(0/+)$ equilibrium level this dependence turns out to be very similar to that of the $(++/+)$ level in accordance with the expectations for a simple As_{Ga} antisite defect. The complexity of the EL2 case underlines two major problems in obtaining reliable stress analyses, namely, to evaluate the influence of stress on capture barriers and for hole traps to include possible effective mass effects even when the capture matrix elements are stress independent. The effective mass problem will be reviewed in the following section in further detail.

3. Effects of band splitting on the capture process

As Eq. (9) shows the emission probability measured in DLTS as defined through detailed balance includes the density of states in the band and the thermal velocities of the carriers. Hence, for uniaxial-stress applications it is crucial to understand how the thermal emission of carriers to a stress-split conduction or valence band is affected. The case of thermal electron emission from defects to the conduction-band minima in the indirect-band-gap n -type semiconductors is fairly simple to treat because the minima represents truly independent bands with well-defined density of states and

carrier effective masses, which to first order are not altered by the application of stress. Under this condition the band minima can be treated as individual noninteracting bands that displace rigidly with changing stress. In general, the band splitting affects the thermal capture process.

Consider an anisotropic defect in one of its possible orientations with respect to the cubic axes of the host crystal. The total probability for thermal emission of carriers from such defect to multiple bands, whether degenerate or not, is the sum of various independent emission probabilities with the consequence that the standard detailed balance expression [Eq. (9)] for the emission rate has to be modified. Nolte and Haller discussed this in detail in Ref. 90 for the case of the silicon valence band. The total probability of emission to two bands split under uniaxial pressure is given by

$$e_n(p) = cT^2 \{ \eta_1 \sigma_1(P) m_1^*(P) \exp[-\Delta G_1(P)/k_B T] + \eta_2 \sigma_2(P) m_2^*(P) \exp[-\Delta G_2(P)/k_B T] \}. \quad (14)$$

In this formula c is a proportionality constant and the quantities $m_1^*(P)$ and $m_2^*(P)$ are averaged effective masses arising from the combination of the density-of-state mass and the thermal velocity mass for each band. The parameters η_1 and η_2 denote the degeneracy factors of the two bands and $\sigma_1(P)$ and $\sigma_2(P)$ the carrier capture cross section of the deep center from each individual band. The terms $\Delta G_1(P)$ and $\Delta G_2(P)$ contain the shift in Gibbs free energy of the deep state for the chosen orientation and the band energy shifts. As indicated both capture cross sections and effective masses may in principle depend on the applied pressure. However, even when this is not the case the difference between m_1^* and m_2^* and a possible difference between σ_1 and σ_2 will cause a significant nonlinearity in the stress response of the position of the energy level of the deep state when derived as $\Delta E(P) = kT \times \ln[e_n(P)/e_n(0)]$.

Nolte and Haller⁹⁰ carried out a detailed analysis for the rather subtle and complicated case of hole emission in p -type material. In this case nonlinearity may originate from the difference in effective masses whereas it is reasonable to assume that $\sigma_1 = \sigma_2$. Even for zero stress it is not possible to determine an effective mass tensor uniquely because the energy surfaces are shaped as warped spheres far from being elliptical or spheroidal. As a consequence approximate average effective heavy- and light-hole masses are conveniently introduced. Nolte and Haller treated the stress dependence of the emission rate in an approximate independent-band model combining the stress shift band-edge energies and then included the additional warping of the energy surfaces in terms of changes in the average effective masses describing the density of states and the thermal velocities.

The applicability of the model was demonstrated successfully for p -type silicon in studies using the iron-aluminum pairs Fe-Al-1 and Fe-Al-2 as reference levels. It should be noted that the model becomes rigid in the high-stress regime where well-defined effective mass tensors can be invoked. Only the stress dependence coming from the coupling to the split off band survives and causes stress dependence of the principal values of the density-of-state tensor whereas the average thermal inverse effective mass is inde-

pendent of the coupling to the split off band as discussed by Hasegawa.¹⁰⁵ Hence, two rigidly displaced independent bands accurately describe the valence band under large stress. We may assume also that (for low enough temperature) the emission occurs to the upper member of the stress split bands implying that in the high stress limit only one of the two terms in Eq. (14) survives and any remaining stress dependence in the capture rate must be ascribed to an explicit stress dependence of either the capture cross section or effective mass. In contrast to this we may assume that when nonlinear stress dependence of the emission from a deep level is encountered at low stress it is likely to originate from the change in the weight of the two terms of Eq. (14).

The situation is somewhat simpler for electron emission to the conduction band. See Balslev¹⁰⁶ and Laude, Pollak, and Cardona¹⁰⁷ for numerical data for the Si and Ge cases, and Ref. 82 for a review of basic concepts regarding the splitting of indirect bands under stress. For silicon the displacements lift the degeneracy at the Δ -point valleys for $\langle 100 \rangle$ and $\langle 110 \rangle$ stress in such a way that the k_z energy lowers for $\langle 100 \rangle$ and increases for $\langle 110 \rangle$ whereas the k_x and k_y valleys stay degenerate. For $\langle 111 \rangle$ stress all three Δ -point valleys stay degenerate. However, since the effective mass is the same for all three valleys there will be no effect of different weighting of the valleys coming from the mass terms in this case and if we further assume that the bands displace rigidly the effective mass cancels in the relative stress dependence of the emission rate. Yet it has been found by Yao, Mou, and Qin¹⁰⁸ and Mou, Yao, and Qin¹⁰⁹ that the emission from and capture to the vacancy-oxygen center is strongly stress dependent at low stress in particular for stress applied along a $\langle 100 \rangle$ direction.

In contrast to this, Samara found in Ref. 86 as reviewed in the preceding section no dependence of the VO level position under hydrostatic pressure indicating that the stress does not affect the capture matrix elements directly. In the light of Eq. (14) this (seemingly conflicting) evidence points to a significant anisotropy in the matrix elements governing the capture from k_z and the k_x or k_y valleys, respectively. In Sec. IV D reviewing the more recent LDLTS results of Dobaczewski *et al.*⁸⁸ we address this problem in further detail.

4. Uniaxial-stress applications

The first successful application of uniaxial stress to determine the symmetry of a deep-level defect was carried out by Meese, Farmer, and Lamp.⁸⁷ Figure 24 reproduced from this work demonstrates the split of the DLTS emission peak of the vacancy-oxygen center obtained in a conventional temperature scan. The splitting under $\langle 111 \rangle$ and $\langle 100 \rangle$ stress in each case into two components of 2:2 and 2:1 intensity ratios, respectively, is consistent with the orthorhombic- I C_{2v} symmetry of the center in accordance with the structure deduced by Watkins and Corbett from EPR and IR measurements (Refs. 84 and 85). Similarly, Henry, Farmer, and Meese¹¹⁰ and independently Kimerling¹¹¹ found the symmetry associated with the 140 meV thermal donor emission consistent with D_{2d} . However, this apparent high symmetry is probably a result of either thermal averaging or just insuf-

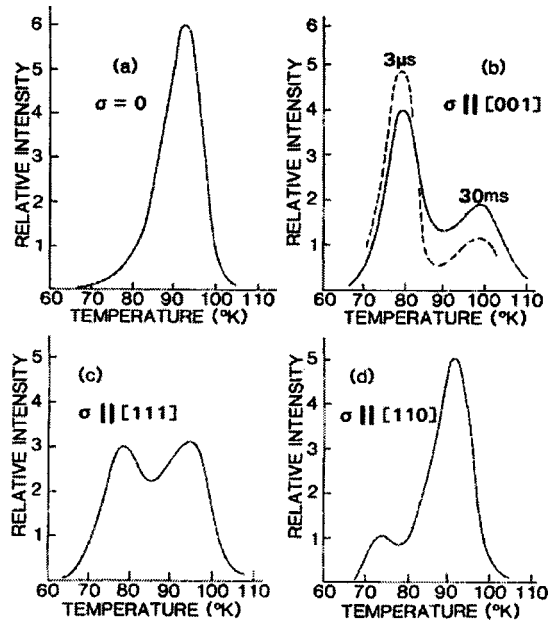


FIG. 24. Reproduced from Meese, Farmer, and Lamp (Ref. 87), the first reported application of uniaxial-stress deep-level transient spectroscopy. The lifting of orientational degeneracy is demonstrated for the A center (VO) by the (partly resolved) splitting of the DLTS peaks obtained in conventional temperature scans of samples under stress. The directions of the applied force relative to the crystal orientation are indicated in the figure.

ficient resolution to resolve the true symmetry (C_{2v}) as determined from IR and EPR studies by Stavola¹¹² and Wagner *et al.*,¹¹³ respectively. In a recent review Stavola¹¹⁴ showed that all available piezospectroscopic data comply with an effective mass type model in which the electronic structure of the thermal-donor states are selectively constructed from wave functions of pairs of aligned k valleys. This model is obviously consistent with the DLTS data when the splitting associated with symmetry lowering $D_{2d} \rightarrow C_{2v}$ is unresolved, or if a thermal broadening of the defect structure averages the symmetry on the time scale of the emission process.

Hartnett and Palmer¹¹⁵ performed conventional DLTS measurements combined with the uniaxial-stress technique on the E1, E2, and E3 irradiation-induced defects in n -GaAs. It has been evidenced previously that these defects are produced by the initial displacement of one atom from its lattice site and it has been proposed¹¹⁶ that the E1 and E2 defects are different charge states of the single arsenic vacancy V_{As} and that the E3 defect is an arsenic Frenkel pair $V_{As}-As_i$. From peak broadening and splitting Hartnett and Palmer concluded that the local symmetry of each of these defects is trigonal C_{3v} which does not agree with postulated T_d symmetries for E1 and E2.

To our knowledge, the first attempt to apply higher resolution DLTS techniques (by a fitting procedure) in conjunction with uniaxial stress to determine symmetry was presented by Yang and Lamp¹¹⁷ who examined the stress dependence of EL2 (0/+) emission in order to resolve an existing ambiguity regarding the symmetry of the center, basically whether it is T_d or C_{3v} distinguishing between the isolated arsenic antisite As_{Ga} or the axial interstitial-pair $As_{Ga}-As_i$. The result of a meticulous least-squares analysis is shown in Fig. 25 as reproduced from Ref. 117. The revealed

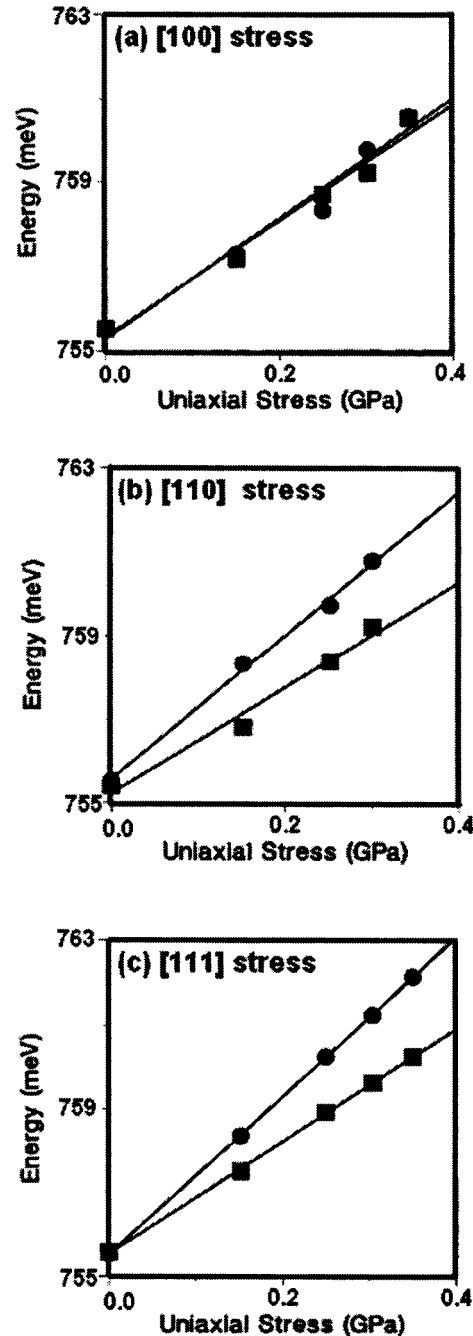


FIG. 25. Reproduced from Yang and Lamp (Ref. 117), the first reported attempt to maximize the separation of emission-rate signals in uniaxial-stress DLTS. The orientational splitting of the EL2(0/+) level is resolved by least-squares decomposition of digitized capacitance transients. The revealed split patterns comply with the C_{3v} symmetry expected for an axial interstitial pair $As_{Ga}-As_i$.

splitting patterns are consistent with trigonal symmetry of the center in accordance with an interstitial pair of C_{3v} symmetry. Obviously the orientational line splitting is very small in accordance with a weak bonding between the arsenic antisite and the arsenic interstitial. Hence, in the light of the difficulty of successfully applying high uniaxial stress to GaAs, it would have been virtually impossible with standard rate window DLTS to resolve the line splitting. The work of Nolte *et al.*¹⁰¹ corroborates this conclusion.

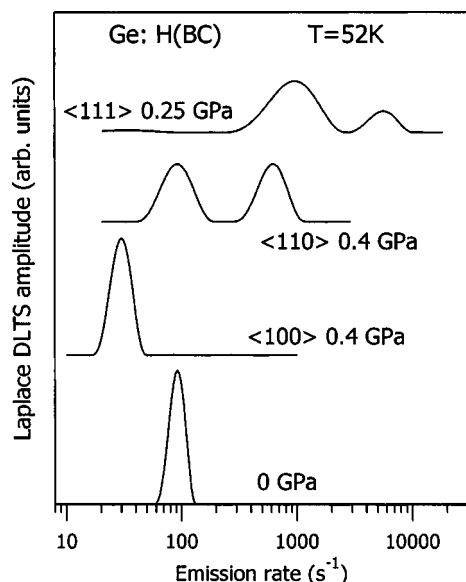


FIG. 26. Reproduced from Dobaczewski *et al.* (Ref. 78). Demonstration of the trigonal symmetry of bond-center hydrogen in Germanium from the splitting of emission peaks under uniaxial stress applied along $\langle 100 \rangle$, $\langle 110 \rangle$ and $\langle 111 \rangle$ crystal directions.

D. Uniaxial stress with Laplace DLTS

In this section we shall review a series of recent results obtained with Laplace DLTS in conjunction with uniaxial stress. Our main purpose is to present some examples that serve to illustrate the type of problems that can rewardingly be addressed. In addition we shall have the opportunity to exemplify the problems of spectroscopic interpretation in the light of the general outline given in Sec. IV B and IV C.

1. Defect symmetry from level splitting...bond-center hydrogen, H_{BC}

As the first example we consider bond-center hydrogen (H_{BC}) in silicon. From its structure with hydrogen located at the axis of a stretched Si-Si bond this center must have C_{3v} symmetry. The center is unstable at room temperature but is the dominating hydrogen defect formed by low-temperature implantation of hydrogen into silicon. It was originally recognized by Holm, Bonde Nielsen, and Bech Nielsen¹¹⁸ as a bistable center by *in situ* application of conventional DLTS to proton-implanted samples at 77 K. The assignment as H_{BC} came from an analysis of the annealing properties and correlation with EPR data, Gorelkinskii and Nevinnyi,¹¹⁹ and Bech Nielsen, Bonde Nielsen, and Byberg.¹²⁰ With the application of uniaxial stress the trigonal character of the center has now been confirmed directly by Bonde Nielsen *et al.*,¹²² and very recently Dobaczewski *et al.*⁷⁸ have identified the analog center in germanium. As a demonstration of the resolved trigonal symmetry by Laplace DLTS we reproduce in Fig. 26 the split pattern for the case of Ge presented in Ref. 78.

It has been found that monoatomic hydrogen can migrate swiftly through a silicon crystal even at temperatures below 80 K. The swift migration occurs through the open areas in the silicon crystal and is initiated as a result of injection of monoatomic neutral hydrogen H^0 into an interstitial tetrahe-

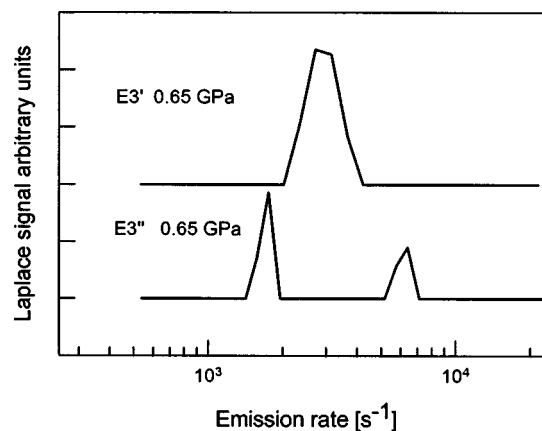


FIG. 27. Reproduced from Bonde Nielsen *et al.* (Ref. 122). Laplace spectra obtained under $\langle 100 \rangle$ stress to demonstrate the lowering of the trigonal symmetry of bond-center hydrogen in silicon (the $E3'$ signal). After the conversion $E3'$ to $E3''$ by annealing the emission peak splits in the ratio 2:1 corresponding to monoclinic symmetry.

dral site of the host crystal of hydrogen. The injection may be caused by annealing of neutral bond-center hydrogen H_{BC}^0 (Bonde Nielsen *et al.*¹²¹) or by electron emission from negatively charged tetrahedral interstitial hydrogen H_T^- (Bonde Nielsen *et al.*¹²²). The swift migration also would occur transiently, for example, after release of trapped hydrogen from a shallow donor impurity (Herring, Johnson, and Van de Walle¹²³), or by release from more complex hydrogen-related defects. In the course of its migration hydrogen may encounter the strain field of an inadvertent impurity like interstitial oxygen or substitution-site carbon, which in turn may slow down the migration.

As an example of this, the strain field around oxygen stabilizes the positive bond-center configuration H_{BC}^+ by about 0.3 eV. Remarkable then is the fact that the electronic properties (such as the position of the donor level of H_{BC}) are practically unaffected by the strain field to the extent that even with application of Laplace DLTS the emission from a strained center ($E3''$) cannot be discerned from the unstrained center ($E3'$) (see Ref. 122 for details). This has naturally caused some confusion in the past. However it has now been shown¹²² that the symmetry of the center does indeed lower from trigonal to (presumably) monoclinic in accordance with the presence of symmetry breaking nearby interstitial oxygen. We demonstrate this in Fig. 27, which compares the effect of uniaxial stress on the regular bond-center signal ($E3'$) and the strained bond-center signal ($E3''$). Despite its small size, the splitting of the $\langle 100 \rangle$ stressed $E3''$ is clearly seen with Laplace DLTS.

Similarly Laplace DLTS has helped disentangle the complex behavior of bond-center hydrogen perturbed by nearby substitution-site carbon. The interpretation of the behavior of this center known as E3 in the literature has caused a great deal of confusion. The center, with activation energy very close to that of ($E3'$) (and $E3''$), was originally observed by Endrös¹²⁴ in plasma treatment of carbon-rich silicon, and by Kamiura *et al.*¹²⁵ in wet chemical etching of regular float zone material. The signal was initially ascribed to a donor level of hydrogen forming a three-center bond Si-H-C_s thus

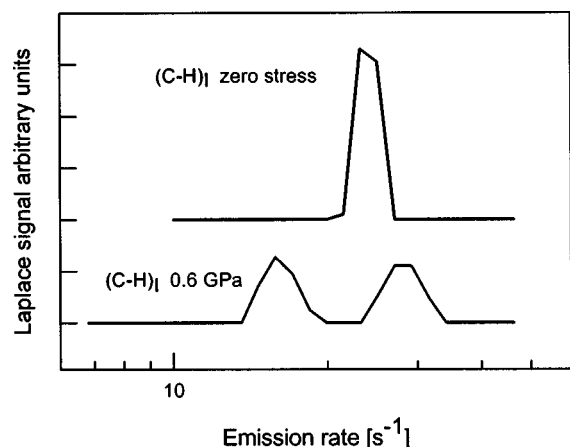


FIG. 28. Reproduced from Andersen *et al.* (Ref. 129). Laplace spectra to demonstrate lowering of symmetry when bond-center hydrogen is perturbed by next-neighbor substitution-site carbon [the $(\text{C-H})_{\text{I}}$ signal]. The carbon perturbation gives rise to the shifted Laplace signal which splits under $\langle 100 \rangle$ showing that the symmetry is now lower than trigonal. The two $(\text{C-H})_{\text{I}}$ spectra have been regenerated after hydrogen implantation and annealing by illumination with and without applied stress.

giving rise to a trigonal center in the silicon lattice. The trigonal character of E3 was later confirmed by Kamiura, Ishiga, and Yamashita¹²⁶ in uniaxial-stress measurements with conventional DLTS, and its dynamic properties discussed further by Fukuda, Kamiura, and Yamashita¹²⁷ and Kamiura *et al.*¹²⁸

In situ Laplace DLTS studies (Andersen *et al.*¹²⁹) showed that the center under certain conditions could be generated in carbon-rich material as an anneal product after low-temperature proton implantation and confirmed its trigonal character but concluded the center had to be an acceptor. In addition, Andersen *et al.*⁴⁷ carried out a detailed piezospectroscopic analysis of the experimental splitting patterns in comparison with theoretical modeling. From this, the center could indeed be identified as the Si-H- C_s bond-center defect as proposed initially. However, it is the acceptor level of this defect which is revealed by the E3 emission. The conclusion of the analysis is that substitution of carbon for silicon pulls this level into the band gap from above and with the further consequence that the donor level moves downward. Intuitively these shifts are the consequences of the asymmetry that the substitution with C_s imposes on the regular three-center Si-H-Si bond, thereby generating some dangling-bond character. A major breakthrough for the reassignment of E3 [denoted $(\text{C-H})_{\text{II}}$ in Ref. 47] was the identification of its precursor $(\text{C-H})_{\text{I}}$ observed directly after implantation at low temperature. This center could be identified as bond-center hydrogen Si-H-Si next to C_s . As in the case of oxygen-induced strain the carbon-induced strain should cause a lowering of the symmetry. This is demonstrated by the uniaxial-stress data shown in Fig. 28.

2. Piezospectroscopic parameters from alignment and splitting: The VO and VOH centers

A general scheme for piezospectroscopic analyses of the lifting of orientational degeneracy of a deep level under uniaxial stress were outlined in Sec. IV B 3 and IV B 4. As was em-

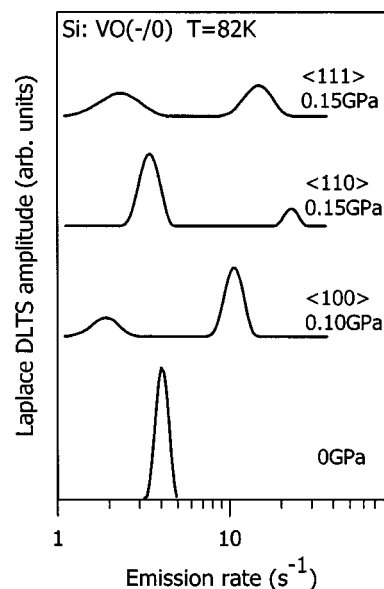


FIG. 29. Reproduced from Dobaczewski *et al.* (Ref. 88). Laplace spectra obtained for the orthorhombic-I VO center under uniaxial stress. Note that $\langle 110 \rangle$ stress should cause splitting into three emission peaks with the intensity ratio 1:4:1. Only two with intensity ratio 5:1 is observed. The true splitting is revealed for stress >0.6 GPa.

phasized the step from just determining the symmetries to extract properly the structure-dependent components of the piezospectroscopic tensor is far from trivial. We exemplify this by means of stress data from Laplace DLTS of the VO (Ref. 88) and VOH center (Coutinho *et al.*¹³⁰). The VO center is a very prominent defect in silicon indeed one of the best studied. The basics for the understanding of its structure were laid early in the history of defect physics by Watkins and Corbett,^{84,85} and as mentioned later supplemented with hydrostatic pressure results⁸⁶ and uniaxial-stress results.^{87,88} The VO center has orthorhombic-I (C_{2v}) symmetry as originally concluded from the EPR study of Ref. 84, and here demonstrated by the Laplace DLTS splitting pattern depicted in Fig. 29.

In contrast to this a recent EPR study of the VOH structure (Johannesen, Bech Nielsen, and Byberg¹³¹) has revealed its symmetry as monoclinic-I (C_{1h}). However, the two centers have much in common as indicated by the sketches shown in Fig. 30. The VOH forms when hydrogen breaks the elongated Si-Si bond, terminates one dangling bond and leaves the other free to capture an electron from the conduction band. In this way the original VO acceptor state is turned into dangling-bond type VOH state shifted downwards in the band. A comparison of the uniaxial-stress response of the VO and VOH acceptor levels is particularly useful to illustrate many of the problems that have to be considered in a thorough piezospectroscopic analysis. As it turns out the symmetry of VOH appear as C_{2v} when interpreted from the level splitting under uniaxial stress. This is, however, an artefact of the rapid jumps of hydrogen between the two equivalent sites as indicated in Fig. 30(b). We shall discuss this further in the following section addressing dynamic properties. Here we shall focus on the extraction of the piezospectroscopic tensor components combining alignment and level splitting. For VO the tensor components should comply with the piezospectro-

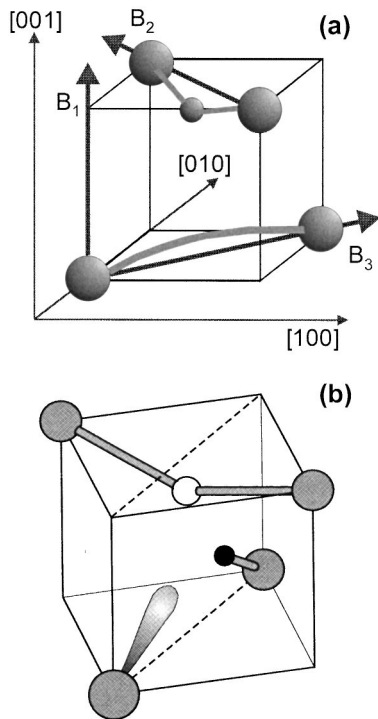


FIG. 30. (a) The geometric structure of the VO defect. The arrows indicate the principal axes of an orthorhombic-I piezospectroscopic tensor. The labels B_1 , B_2 , B_3 denote the corresponding eigenvalues. (b) The modification of the structure (a) when VO traps a hydrogen atom.

scopic EPR results of Ref. 84 and comparisons with these results may therefore serve as a check to evaluate the consistency of the piezospectroscopic analysis of the Laplace DLTS results. We present this comparison in Table I which also includes a comparison with recent theoretical results (Coutinho *et al.*¹³²). As can be seen from the table there is overall fair agreement considering the typical errors of ~ 0.5 eV ascribed to all experimental and theoretical values.

The Laplace data of Table I have been derived from comparison of the splitting of the emissions peaks (Fig. 29) as a function of the applied external pressure with the departures from the statistical intensity ratios compared to the intensity ratios of Fig. 29 after rapid cooling from a high temperature at which equilibrium alignment under stress had been achieved at the high temperature. As outlined in Sec. IV B 4 the level splitting records the influence of stress on

TABLE I. Piezospectroscopic tensor components for the vacancy-oxygen center. Comparison of theoretical and experimental results. The DLTS data are from alignment but consistent with the data obtained from splitting in the high-stress limit (cf. Fig. 30) and the discussion in Sec. IV D 4.

Tensor component	Theory ^a	EPR ^b	Laplace DLTS ^c
B_1^0	-9.8	-11.1	-11.4
B_2^0	5.5	6.1	5.7
B_3^0	4.5	4.9	5.7
B_1^-	-6.8	-8.4	-8.0
B_2^-	7.8	8.8	9.0
B_3^-	-0.5	-0.4	-1.0

^aReference 132.

^bReference 84.

^cReference 88.

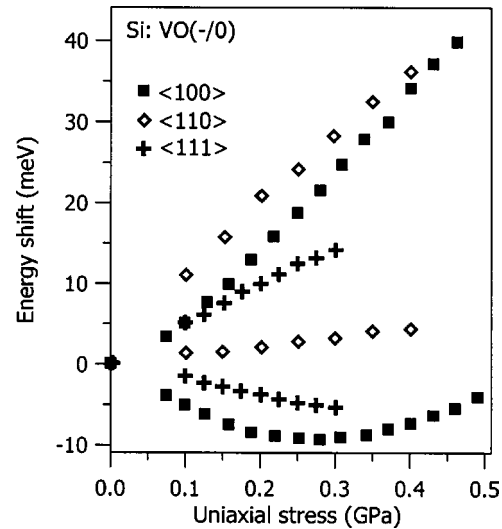


FIG. 31. The stress dependence of VO for the three major stress directions $\langle 100 \rangle$, $\langle 110 \rangle$ and $\langle 111 \rangle$ defined as $\Delta E = k_B T \times \ln[e_n(P)/e_n(P=0)]$, from Dobaczewski *et al.* (Ref. 88).

the ionization process $VO^- \rightarrow VO^0 + e_c^-$, and thereby contains information that depends on both charge states of VO simultaneously. Contrary to this the stress-induced alignment allows the energy shifts to be determined (see Sec. IV B 5) for the different orientations in the individual charge states VO^0 and VO^- . As an example of the interplay between these two approaches we compare the results obtained from stress applied along a $\langle 111 \rangle$ crystal direction. Here the stress coefficient determining the energy separation is given by $\alpha_{\langle 111 \rangle} = \pm s_{44}(B_2 - B_3)$, where s_{44} is a component of the silicon elastic compliance tensor, and $B_{2(3)}$ are eigenvalues of the defect strain tensor [see Fig. 30(a) and Ref. 88 for more details]. In this case the absence of any alignment in the neutral charge state shows that $B_2^0 \approx B_3^0$, to within a couple eV. However, the fact that a significant $\langle 111 \rangle$ splitting is observed then shows that B_2^- must be different from B_3^- reasonably consistent with the direct alignment result $B_2^- - B_3^- = 10 \pm 2$ eV and the splitting result $(B_2^- - B_2^0) - (B_3^- - B_3^0) = 15 \pm 2$ eV. Similar comparative analyses for the other stress directions then lead to the completion of Table I. In this regard it is important to emphasize that it is the linear splitting in the high stress regime that has to be compared with the alignment data. This is particularly true for the $\langle 100 \rangle$ case where a branch reveals very strong bending at low stress as shown in Fig. 31. We shall return to this problem in Sec. IV D 4.

The VOH center shows C_{2v} symmetry on average. However, as mentioned in Sec. IV B 4, when comparing experimental data with theory one should use averaged values calculated from the static C_{1h} structure as the electron is emitted while hydrogen is bound to one or the other of the two Si partners. Such a comparison is particularly simple for the $\langle 100 \rangle$ case because here the applied stress renders the two possible orientations of the Si-H bond energetically equivalent and no further splitting as compared to C_{2v} symmetry occur. The comparison has been done in Ref. 130. The experimental splitting of the fast and slow branch of the split pattern $\alpha_{\langle 100 \rangle}^{f(-/0)} - \alpha_{\langle 100 \rangle}^{s(-/0)} = 21$ meV/GPa where the su-

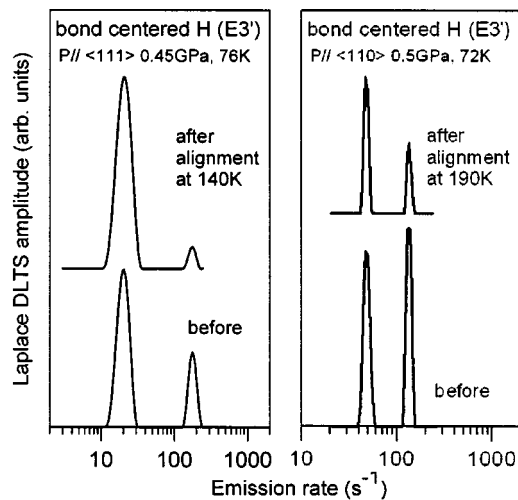


FIG. 32. The connection between alignment and diffusion illustrated by the E3' emission from bond-center hydrogen. The stress splitting of the Laplace DLTS line before and after an alignment process carried out at two different temperatures 140 and 190 K, from Dobaczewski *et al.* (Ref. 133).

perscript $(-/0)$ indicates ionization. Similarly for the neutral state the experimental figure is $\alpha^{f(0)}_{\langle 100 \rangle} - \alpha^{s(0)}_{\langle 100 \rangle} = 109 \text{ meV/GPa}$. The theoretical values (Ref. 130) for the same quantities are 24 meV/GPa and 96 meV/GPa, respectively, in fair agreement with the experimental values.

3. Dynamic properties: The H_{BC} , V_2 , VO , and VOH centers

We have already touched upon the role that dynamic effects may have on the interpretation of thermal uniaxial-stress data, and present here a number of examples from Laplace DLTS studies to illustrate more specifically various aspects related to dynamics.

Reorientation and diffusion. Obtaining the piezospectroscopic behavior from alignment studies, as discussed in the preceding section, relies on the control of the reorientation dynamics since the equilibrium populations have to be reached at the temperature of alignment and then instantly frozen at the temperature which the emission spectrum is actually recorded. This may limit the range in temperature that can actually be utilized to generate the alignment. We chose as an illustration the case of the E3'-donor emission of bond-center hydrogen. Figure 32, taken from Dobaczewski *et al.*,¹³³ depicts the uniaxial-stress split patterns before and after alignment measurements at low temperature. Before the alignment, when stress is applied along $\langle 111 \rangle$ or $\langle 110 \rangle$ the Laplace DLTS emission peak splits into two components, with the amplitude ratio 3:1 or 1:1, respectively whereas no splitting is observed for stress along $\langle 100 \rangle$, all in accordance with trigonal symmetry as outlined in Sec. IV D 1. When stress is applied to the biased sample at 140 K, i.e., with the defect in the positive charge state and well below the temperature where long-distance migration of hydrogen sets in the hydrogen can jump between different BC positions (see left-hand side of Fig. 32), the initial peak amplitudes are changed whereas the sum of their amplitudes remains constant. Hydrogen is expelled from the bonds having zero angles with the stress direction and recovered in one of the

other three equivalent bonds. This is a result of the stress counteracting the outward relaxation of the silicon atoms in the three center Si-H-Si bond. Hence, at 140 K H_{BC}^+ can jump between bond-center positions but the temperature is too low for the migrating ion (in the available time) to reach any trap in the crystal and form some other defect structure. When the alignment process is carried out at 190 K (Fig. 32, right) an analogous alignment occurs. In this case, however, the total amplitude is not maintained indicating that a fraction of the migrating hydrogen atoms have got time to reach trapping centers and form new defects.

A similar connection between reorientation and diffusion applies to the divacancy. The V_2 is relatively stable governed by a barrier of $\sim 1.4 \text{ eV}$ (Watkins and Corbett¹³⁴) and (Stavola and Kimerling¹³⁵) but whether its disappearance is due to diffusion as an entity or dissociation is not known. Whichever it is, the first step in the process should be a jump of a neighboring silicon atom to fill one of the adjacent vacancies. The two resulting vacancies are now in the second-nearest positions. If the next step in the process is a further jump of the silicon atom to fill the other vacancy then the net result is that the V_2 is simply reconfigured or returned to its original orientation in the lattice. Alternatively if the second jump involves a different silicon atom then the vacancies are further separated and the second jump may be considered as the first step in dissociation.

Under $\langle 111 \rangle$ stress the Laplace DLTS emission peak of the $V_2(-/-)$ level splits in the intensity ratio 3:1 indicating that the initial state has trigonal symmetry, see later for further discussion of this point. It is well established that V_2 is stable below $\sim 550 \text{ K}$. This high-temperature stage must refer to the neutral charge state of the defect, i.e., V_2^- and V_2^- are stable below the temperatures at which the Fermi level crosses the $(-/-)$ or $(-/0)$ levels, respectively. Annealing under stress shifts the annealing stage downwards. At 350 K a clear alignment effect shows in the Laplace spectrum when 0.5 GPa stress is applied along a $\langle 111 \rangle$ axis. The small line loses $\sim 70\%$ in amplitude essentially without any gain in the larger line.

This overall reduction shows that the reorientation is accompanied by dissociation and/or enhanced diffusion to traps. A simple explanation would be to assume that the barrier for a single jump $\text{Si} \rightarrow V_{\text{Si}}$ between two neighboring substitution like lattice sites is lowered by the stress. Under this condition it is easily conjectured that the defect reorients to avoid having the V - V axis aligned with the stress. In this argument we disregard that the charge state in which the defect anneals actually departs from trigonal symmetry and becomes monoclinic (see Ref. 134). The reorientation competes with dissociation into adjacent monovacancies. Hence, the loss in amplitude is accounted for qualitatively and the V_2 case provides a neat example of stress-induced annealing. For defect complexes, which are anchored by an immobile constituent, the alignment may occur at a much lower temperature than the diffusion onset. This has been shown to apply for H_{BC} next to interstitial oxygen (the E3'' center) and for VO and VOH as well.

The reorientation saddle point. The two examples of the preceding section provide intuitively reasonable, yet very

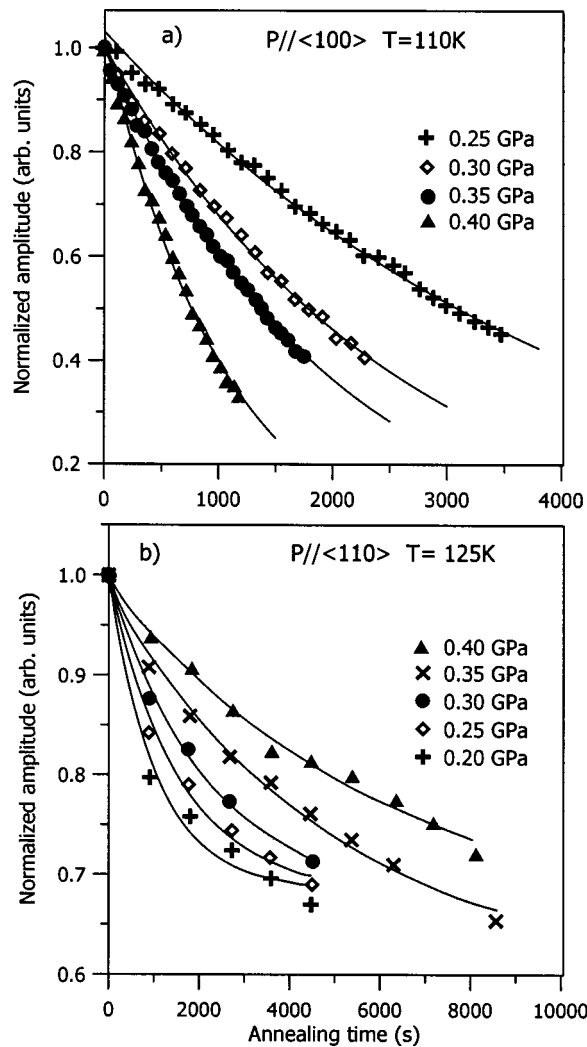


FIG. 33. Reproduced from Dobaczewski *et al.* (Ref. 88). The VO^0 reorientation kinetics measured from the change in amplitude of the stress-split Laplace DLTS peaks of Fig. 29 in a sequence of isochronal annealing steps at a fixed temperature. For $\langle 100 \rangle$ the reorientation time constant decreases with stress whereas for $\langle 110 \rangle$ the time constant increases with stress.

qualitative, modeling of reorientation and migration kinetics. For the VO center this modeling has been pursued further. The extensive Laplace DLTS work of Ref. 88 explores the influence of stress on the oxygen reconfiguration trajectory quantitatively. The geometrical structure of the center was shown previously [Fig. 30(a)]. Obviously, the position of the interstitial oxygen atom must have the option of switching to a position between two other equivalent Si atoms with a corresponding switch of the elongated Si-Si bond. The saddle point of this thermally activated switching may be considered as the precursor for an oxygen diffusion process where the migrating oxygen atom is accompanied by a vacancy. The concept of a migration trajectory with a saddle point implies that the process can be treated adiabatically and consequently that a saddle point can be determined from measurements of the stress dependence of reorientation barriers.

In accordance with this the reorientation kinetics for VO as a function of applied uniaxial stress were obtained in sequences of isothermal annealing steps. Figure 33 illustrates

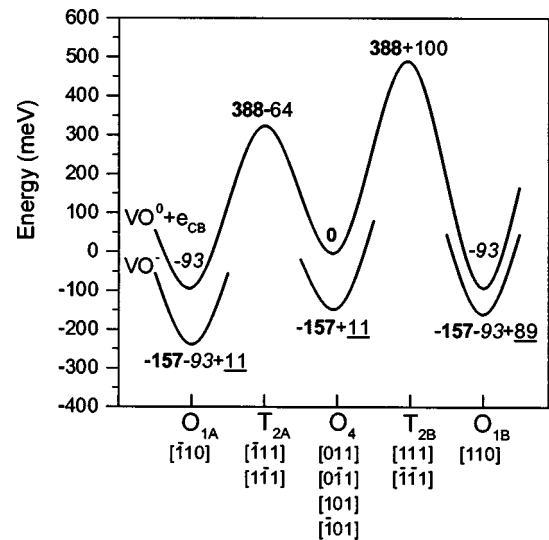


FIG. 34. Reproduced from Dobaczewski *et al.* (Ref. 88). The total energy diagram for the VO defect stressed along the $[110]$ direction showing the splitting of the T_2 saddle point under stress. Below each minimum the corresponding vectors parallel to the elongated Si-Si bond, according to Fig. 30, are given. For the maxima the vectors indicate orientations of the trigonal axes. The numbers in bold font are zero stress data. Italic and underlined fonts denote values obtained from alignment and peak splitting, respectively. All stress data are referenced to a stress of 1 GPa. The increase of the barrier at T_{2B} has been measured directly; the decrease at T_{2A} is estimated.

the results of such measurements for the neutral charge state VO^0 under $\langle 100 \rangle$ stress and $\langle 110 \rangle$ stress, respectively. As can be seen the application of stress speeds up the reorientation process in the former case and slows down the process in the latter case. The corresponding stress coefficients derived from the time constants are -84 ± 8 meV/GPa and 100 ± 3 meV/GPa, respectively. On the basis of these data in combination with the piezospectroscopic tensor components obtained from level splitting and alignment it has been possible to construct the total energy diagram for the VO pair stressed along a $\langle 110 \rangle$ axis which is depicted in Fig. 34 taken from Ref. 88.

The diagram visualizes the trigonal symmetry of the saddle point. For $\langle 110 \rangle$ stress the elongated Si-Si bond has three different orientations with respect to the stress, and these orientations are represented by the three minima in the diagram O_{1A} , O_{1B} and O_4 . For a saddle point of trigonal symmetry there have to be two different energy barriers separating these minima. These are marked T_{2A} and T_{2B} on the diagram where the fourfold degenerate O_4 minimum has been chosen as reference point for the energy scale. As can be seen the saddle barrier splits into two components. The increase of the T_{2B} barrier is measured directly, whereas the decrease in the T_{2A} barrier is estimated using the measured decrease under $\langle 100 \rangle$ stress (see Fig. 34) to estimate the hydrostatic component of the saddle-point piezospectroscopic tensor relative to the energy minimum. The doublet structure of the saddle point under $\langle 110 \rangle$ stress indicates that the saddle point has trigonal symmetry. Furthermore this symmetry is the only one that is consistent with the combined set of all available stress data. The VO case provides an excel-

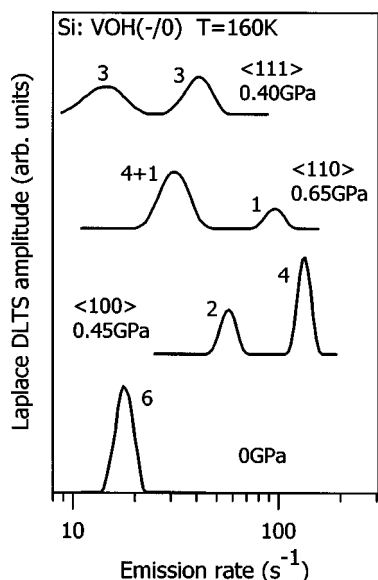


FIG. 35. Reproduced from Coutinho *et al.* (Ref. 130). Laplace DLTS spectra of VOH(-/0) recorded at 160 K at zero stress and under uniaxial stress along the three major crystallographic directions. The splitting pattern establishes the effective (i.e., thermally averaged) orthorhombic- I (C_{2v}) symmetry of (cf. Fig. 30).

lent example of the potential of high-resolution uniaxial-stress DLTS to obtain unique microscopic information on diffusion processes.

Thermal averaging of defect symmetry. We showed earlier [Eq. (13)] how under certain conditions rapid thermal ionic jumps (defect reconfigurations) may result in an apparent increase of the symmetry of a defect when determined by DLTS and revisited the problem briefly in our discussion of the piezospectroscopic analysis of the VOH center. We shall now consider the VOH example in further detail. Figure 35 depicts the Laplace spectra of VOH(-/0) taken from Ref. 130. The splitting pattern establishes the effective orthorhombic- I (C_{2v}) symmetry. However, the real symmetry is monoclinic- I (C_{1h}) as concluded from EPR measurements by Johannesen, Bech Nielsen, and Byberg (Ref. 131). From motional narrowing they also revealed the $C_{1h} \rightarrow C_{2v}$ conversion resulting from thermally activated jumps between the

two equivalent configurations [Fig. 30(b)]. Similarly these jumps are responsible for the C_{2v} symmetry found by DLTS because they may cause effective emission rates to be recorded in accordance with Eq. (13).

Figure 36 taken from Ref. 130 depicts a detailed theoretical model taking the averaging effect into account. The figure serves to illustrate how the averaging causes an apparent increase in symmetry with the net result that essentially one dominating component prevails in the averaged emission rate. Note for $\langle 110 \rangle$ that the fourfold degenerate (averaged) eightfold component is close in energy to one of the twofold components in agreement with the unresolved (4+1) emission peak of Fig. 35. The case of VOH is to our knowledge the best documented example on the role of thermal averaging in the interpretation of DLTS uniaxial-stress data. Obviously a lack of spectral resolution could be mistaken for thermal averaging and this emphasizes that care must be exercised in drawing conclusions about static symmetry from uniaxial-stress DLTS alone, in particular when the measurement requires data recording at a relatively high temperature. Hence, point-defect levels near midgap will typically not be accessible to the technique because thermal averaging may render the apparent symmetry isotropic irrespective of the underlying static symmetry.

Relaxation effects. Some defects are known to undergo charge-state controlled relaxations. The simplest consequence of this is the appearance of barriers in the capture cross section entering in the preexponential factor of the emission rate as recorded by DLTS. In a standard level splitting experiment the stress dependence of these barriers cannot be distinguished from those of the level energy. We conjecture that one may attempt to disregard the possible influence of stress on the data analysis when no barrier in the capture cross section is found at zero stress. Then in the linear approximation the effect should be small as argued in the general remarks of Sec. IV B 5. The test of this would be to measure the capture cross section directly (i.e., by changing the filling pulse width) as a function of stress and/or to check the internal consistency of data from level splitting and alignment. One should also be on the alert when significant deviations from a linear stress response are observed.

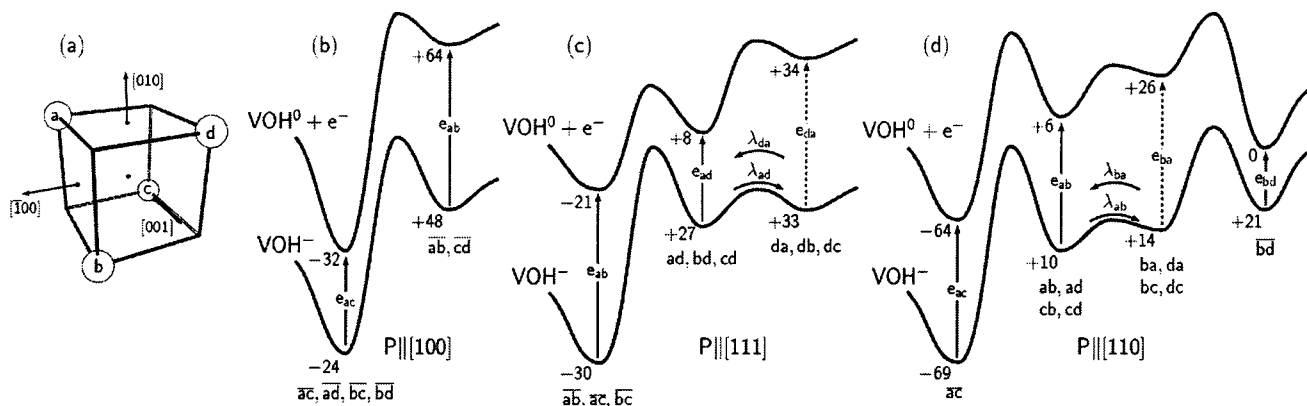


FIG. 36. Reproduced from Coutinho *et al.* (Ref. 130). Theoretical values for the various energy minima under stress for VOH assuming C_{1h} symmetry. The labeling scheme for the 12 different orientations in a cubic crystal is indicated in (a). Each orientation is labeled by an ordered letter pair denoting the site of H and the Si dangling bond and labels with bars represent doubly degenerate configurations. In (b), (c), and (d) schematic configuration coordinate diagrams for compressive stress of 1 GPa along the major crystal axes are given with energy shifts in meV. The averaging by reorientation is indicated by arrows.

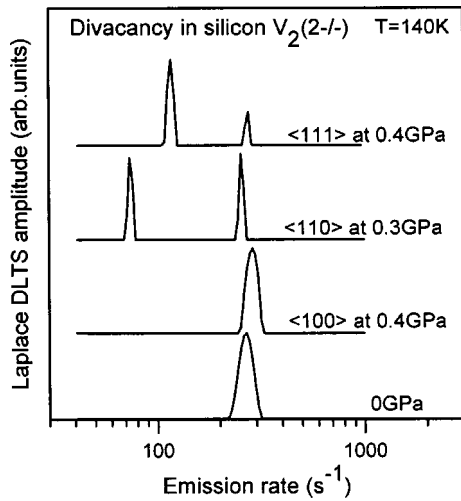


FIG. 37. Laplace DLTS spectra of the $V_2(2-/1-)$ level taken without stress and with stress applied along the three major crystallographic directions (Ref. 136). The $\langle 110 \rangle$ splitting is larger than the $\langle 111 \rangle$ splitting indicating an anomaly in the otherwise trigonal pattern.

This point will be addressed in more detail in the following section but first we will consider the double-acceptor emission $V_2(2-/1-)$ of the divacancy.

According to Watkins and Corbett¹³⁴ the symmetry of the V_2 center is reduced from trigonal D_{3d} to C_{2h} monoclinic when the odd electron is gained to form the negative charge state, i.e., from the symmetry of two empty sites surrounded by six substitutional atoms to a symmetry with a mirror plane parallel to the axis joining two empty sites. The driving force for this symmetry lowering is the Jahn-Teller effect. In contrast to this it would appear that the D_{3d} should be maintained in the V_2^{--} charge state because no Jahn-Teller driving force is present in this case. Hence, the possibility exists that the $V_2(2-/1-)$ emission should be accompanied by an instantaneous Jahn-Teller relaxation which should manifest itself in the uniaxial-stress split pattern.

Figure 37 (from Dobaczewski *et al.*¹³⁶) indicates a trigonal symmetry just by counting the number of components and noticing the relative intensities of the split emission lines. However for a true trigonal-to-trigonal transition the splitting under $\langle 111 \rangle$ stress should be 4/3 times larger than the splitting under $\langle 110 \rangle$ stress, which is in obvious contradiction to the experimental emission spectra. The detailed analysis of Ref. 136 shows that the data can be consistently analyzed under the assumption that the center undergoes the relaxation $D_{3d} \rightarrow C_{2h}$ in the ionization process. In this sense the V_2 case is unique as the only example we know of where a symmetry lowering in a thermal emission process has been observed directly.

4. Uniaxial stress and the preexponential factor: The VO center

Figure 31 taken from Ref. 88 depicts the stress dependence of the Laplace DLTS peak shifts denoted as an energy shift assumed to be proportional to the term $k_B T \times \ln[e_n(P)/e_n(0)]$, where e_n is the peak frequency at a given stress and T is the measurement temperature. The slopes at high stress are the data entering in the piezospectroscopic

analysis discussed in Sec. IV D 2. Here we focus on the unique feature that the $\langle 100 \rangle$ branches with the applied stress perpendicular to the elongated Si-Si bond [see Fig. 30(a)] display a very strong bending at low stress whereas reasonable linear dependencies are found for the other stress direction and orientations of the VO defect. We can exclude that the bending reflects a genuine nonlinearity in the stress-induced level splitting. This follows from the consistency of the stress derivatives measured at low stress by alignment and at high stress by level splitting. Hence, we can maintain the first-order linear stress analysis as far as the energy shifts are concerned. Yao, Mou, and Qin¹⁰⁸ found that also the capture rate depends strongly on $\langle 100 \rangle$ stress, in this case for both orientations of the center. This strongly suggests that the explanation of the bending could be a property of the preexponential factor. At present we cannot rule out that the bending could result from a peculiar strong nonlinearity at low stress of the capture cross section itself. However, this is obviously not very likely since the physics behind it has to single out a unique nonlinearity at low stress for just one stress direction and one defect orientation.

Alternatively we may seek the explanation in the stress splitting of the conduction-band edge (see, e.g., Ref. 82). The general formula (9) indicates how the bending could arise from the splitting of the conduction band if the σ terms in $\eta_1 \sigma_1(P) m_1^*(P)$ and $\eta_2 \sigma_2(P) m_2^*(P)$ are different, but not necessarily stress dependent. For the conduction band of silicon the first term with $\eta_1=1$ refers to the band minimum labeled according to the k_z valley and the second term with $\eta_2=2$ refers to the $k_x(k_y)$ valley minima which stay degenerate for any of the stress directions indicated in Fig. 30. Inspection of Eq. (14) shows that the lifting of the conduction-band degeneracy will indeed generate a bending phenomenon at low stress not violating the concept of linear stress response.

However, when $\sigma_1(P) m_1^*(P) = \sigma_2(P) m_2^*(P)$ the bending effect for a given stress direction will be rather small and identical for each of the two nonequivalent defect orientations. Now $m_1^*(0) = m_2^*(0)$ for the conduction band and we may further assume that different k valleys displace rigidly under low stress. Hence, to explain the bending we may conjecture that capture into anisotropic centers may depend significantly on the orientation of the center relative to the cubic axes of the host material. This would imply that $\sigma_1(P)$ differs from $\sigma_2(P)$ and we may attempt an analysis neglecting possible minor direct stress dependencies of these cross-sections. Obviously, in accordance with experiment, within this scheme there should be no bending for $\langle 111 \rangle$ stress since the conduction band stays degenerate. In contrast, the strong bending at low stress in the $\langle 100 \rangle$ case arises because here the conduction band splits the largest amount. In fact a quantitative analysis with $\sigma_2(0) \sim 8\sigma_1(0)$ and the known splitting of the conduction band reproduces the bending of both branches surprisingly well. However, a detailed confirmation and analysis should await stress measurements in progress for quantitative correlations of capture rates and energy shifts.

V. ALLOY EFFECTS

Point defects in semiconductor alloys are not in unique environments. The random distribution of the alloy constituents causes the chemical nature of individual atomic bonds to vary, hence for a defect of a particular type the bond lengths and relaxation of the atoms around a defect differ throughout the alloy. The defect electronic wave functions are localized on the scale of a few bond lengths and are therefore sensitive to the details of the atomic configuration only in the close vicinity of the defect. This lack of the uniqueness of the bond chemistry, length, and angle (lattice relaxation) has the consequence that a deep-center energy level, upon alloying, tends to split into a manifold of components, i.e., to exhibit fine structure in the ionization process. The interpretation of this fine structure in terms of spatial splitting of total-energy levels is far from straightforward because, in general, both initial and final states of the process are alloy sensitive. However, as long as the alloy is macroscopically homogeneous it may be assumed, that the observation of fine structure (or line broadening) in the ionization spectra of defects is a manifestation of spatial fluctuations in the alloy composition on the microscopic scale rather than variations in bulk band-gap parameters. This is because the alloy fluctuations are well averaged for the final state of the carrier in the band. Therefore, when the fine structure of the thermal spectrum is to be interpreted in terms of “alloy splitting” of the bound-state total energy, the effective radius of the bound carrier may be regarded as the crucial parameter.

The alloy splitting, when properly quantified, can be an important source of information as far as the microscopic structure of a defect is concerned and can also reflect the way in which a defect in the crystal is created. In this chapter three different cases of the effect of crystal alloying on the defect properties are presented.

- (1) The structure observed in the Laplace DLTS spectra for the so-called DX centers in ternary alloys of $\text{Al}_x\text{Ga}_{1-x}\text{As}$ reflecting the fact that in this case the properties of the emission barrier originates predominantly from the large lattice relaxation evidenced for these defects.
- (2) The alloy structure observed for the substitutional atoms of gold and platinum in SiGe elemental alloy showing that these atoms prefer to site in the more germanium-rich regions of the alloy as a result of the kick-out mechanism governing their in-diffusion.
- (3) The structure of implanted interstitial hydrogen atoms in the SiGe alloy shows that the affinity of hydrogen towards germanium becomes extremely strong as a result of microscopic strain fluctuations in the alloy.

A. III-V alloys: The DX centers in AlGaAs

The effect of the alloy splitting for the DX states¹³⁷ has been studied for the ternary random alloys of $\text{Al}_x\text{Ga}_{1-x}\text{As}$. In this case the alloying occurs only in the Group III sites, i.e., in every second shell of atoms surrounding a given atomic site. Thus for the substitutional site on the Group III or Group V sublattice the closest mixed atom shell is in the

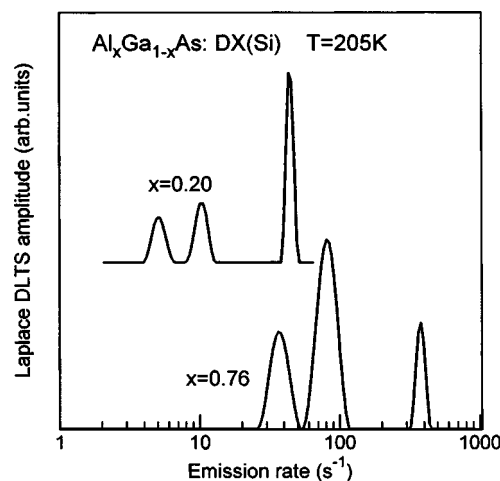


FIG. 38. The Laplace DLTS spectra of DX(Si) in $\text{Al}_x\text{Ga}_{1-x}\text{As}$ for $x=0.20$ and $x=0.76$.

second- or first-nearest neighborhood, respectively. A similar effect is observed for non equivalent interstitial sites of the zinc blend unit cell.

The silicon atom acting as a donor in $\text{Al}_x\text{Ga}_{1-x}\text{As}$ replaces the Group III element so that the first-nearest neighbor sites are four arsenic atoms. The alloying occurs in the second-nearest shell where there are 12 gallium or aluminum atoms. If the DX state had been formed by the silicon atom in the substitutional position then the alloy-split DX state should have consisted of up to 13 components. The Laplace DLTS spectra of DX(Si) have been studied in a very wide range of alloy compositions^{138,139} ($x=0.20-0.76$) and two extreme cases are presented in Fig. 38. For all alloy compositions investigated the pattern of peaks always related to DX (Si) as it consisted of three peaks. The shift on the frequency scale between the spectra in Fig. 38 reflects the variation of the band gap with the alloy composition and the pattern can be explained using the microscopic model of the mechanism leading to the DX state formation.¹³⁸

It has been observed experimentally that the energy of the DX level as measured from the bottom of the conduction band is several times smaller than the activation energy of the thermal emission process observed in the DLTS experiments (see Ref. 140, and references therein for more details). Consequently, the level position is predominantly a result of the lattice relaxation, which also is responsible for the metastability phenomena observed for the defects. The microscopic model of the DX state is based on the fact that the DX (Si) state is formed when the silicon atom breaks one of the bonds with arsenic and moves to the interstitial position [see configuration of DX in Fig. 39(a)]. This site of silicon becomes stable when the defect binds two electrons. Then when these electrons are emitted and the defect is ionized the silicon returns to the substitutional site (the d^+ configuration). In this model the emission barrier is essentially the energy necessary for silicon to push aside three arsenic atoms in order to return from the interstitial to the substitutional position. This energy should be rather insensitive to the alloying effect present only in the second-nearest neigh-

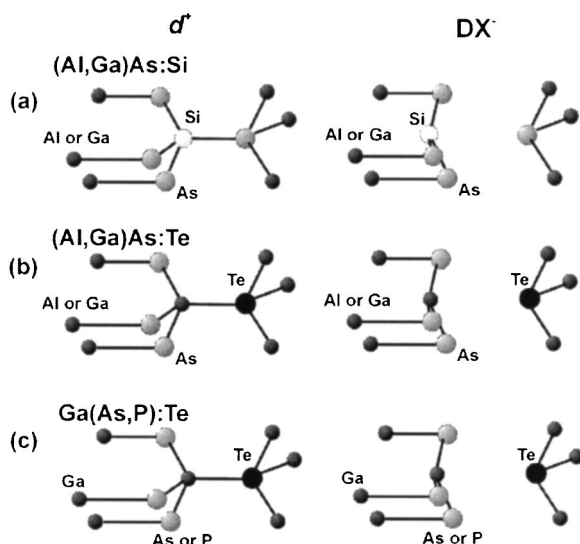


FIG. 39. The model of the DX state in the negative (DX) and positive (d^+) charge state for the silicon donor in AlGaAs (a), and tellurium in AlGaAs (b), and in GaAsP according to Ref. 140.

borhood and this seems to be the reason why the pattern of peaks observed for the DX(Si) state does not depend on the alloy composition.

As far as the fine structure is concerned, the silicon atom has one out of four bonds to break. The number of aluminum atoms found opposite this bond decides which of them is preferred and it is assumed that the silicon atom prefers to move towards the aluminum-rich site. The lifting of spatial degeneracy by bond breaking may be explained by the following example. If for a given silicon atom the most aluminum-rich direction contains two aluminum atoms opposite to a Si-As bond and if the same number of aluminum atoms are found also opposite another Si-As bond then the bond-breaking process will be twofold spatially degenerate. A detailed Arrhenius analysis showed that for the given alloy composition the activation energies of the three DX(Si) peaks are exactly the same. It is conjectured then that the peak triplet represent defects with a different spatial degeneracy of the bond-breaking process and with some difference in the electron capture cross section. The extreme right-hand peak represents a degeneracy of 1, the middle peak 2, etc.

For a random distribution of the gallium and aluminum atoms among the Group III sites in the crystal one can calculate for any alloy composition the probability of finding the DX(Si) state of a given spatial degeneracy. The result of such a simulation is shown in Fig. 40. It is seen that in the 0.20–0.76 composition range the probability of finding the degeneracy equal to 4 is low so basically only three peaks are expected. The gray bars mark the alloy compositions of the spectra shown in Fig. 38. The intersection of the bar with the line represents the relative amplitude of the peak for the given alloy composition. The ratios between the experimental peak amplitudes are almost exactly the same as those derived from the diagram. Note that for $x=0.76$ the degeneracy equal to 2 is expected to be the most abundant and this is indeed observed experimentally as depicted in Fig. 38 where for this alloy composition the middle peak in the spectrum is the highest one.

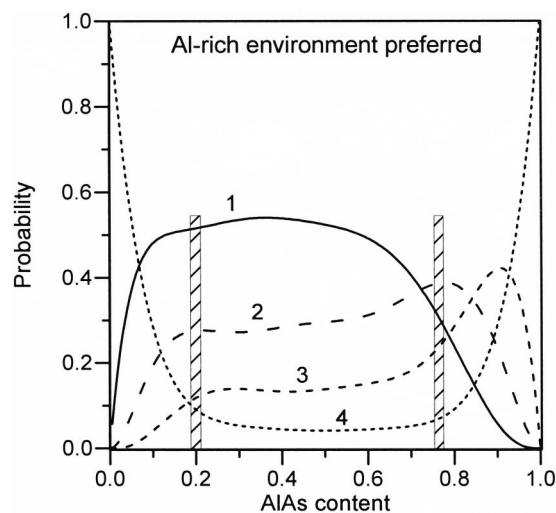


FIG. 40. The calculated concentrations of the DX state with the spatial degeneracy equal to one, two, three, and four (Ref. 139). The bars mark the alloy compositions for which the spectra in Fig. 38 are shown. From an intersect of a bar with a given line one can foresee an amplitude of a peak on the spectra shown in Fig. 38.

The situation is different for the tellurium donor in $\text{Al}_x\text{Ga}_{1-x}\text{As}$. Here Te replaces the Group V element, thus the Group III sublattice instability leading to the DX state formation means that one of the Group III elements neighboring tellurium breaks the bond and moves to the interstitial position [Fig. 39(b)]. However, because in this case the bond-breaking element can be either a gallium or aluminum atom there should be more components seen in the Laplace DLTS spectra for DX(Te) than for DX(Si). This has been confirmed experimentally. The spectra observed for DX(Te) do contain more components [Fig. 41(a)] and, moreover, the Arrhenius analysis performed shows that peaks form two groups differing in activation energy. Furthermore, the relative concentrations of these groups vary with alloy composition. From these observations it has been concluded that one group represents the DX formation process when the aluminum atom moves to the interstitial position whereas the other group corresponds to the gallium atom participating in the process (see Refs. 138 and 139 for more details).

Finally, the Laplace DLTS spectra have been observed for DX(Te) in $\text{GaAs}_{0.65}\text{P}_{0.35}$ [Fig. 41(b)]. In this case the alloying occurs for the Group V element sublattice, and despite this the substitutional-interstitial instability occurs only for a gallium atom. The emission barrier is formed by different combinations of arsenic and phosphorus atoms [see Fig. 39(c) for details of the model]. Consequently, one can expect up to four different emission barriers overlaid with spatial degeneracy effects which creates a very complex system. Hence the spectrum of DX (Te) in $\text{GaAs}_{0.65}\text{P}_{0.35}$ is very broad and becomes difficult to disentangle. Nevertheless four features can be seen which is a result in agreement with the microscopic model of the DX formation process.

To summarize, the case of the alloy effects for the DX state in the ternary alloys has turned out to be very difficult to interpret. First, there were controversies concerning the identification of the effect. A substantial ambiguity has been caused by the fact that silicon in MBE grown layers of

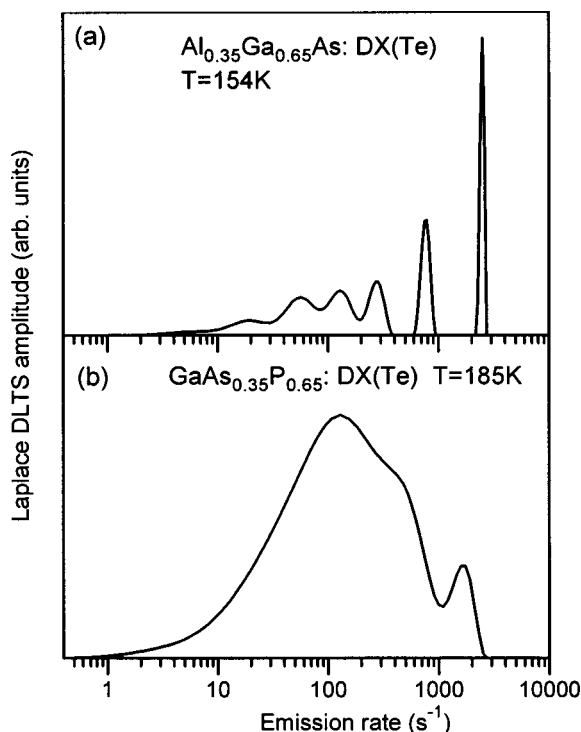


FIG. 41. The Laplace DLTS spectra of DX(Te) in (a) $\text{Al}_x\text{Ga}_{1-x}\text{As}$ for $x=0.35$, and in (b) $\text{GaAs}_{1-x}\text{P}_x$ for $x=0.35$.

AlGaAs has a tendency to agglomerate when a sample is not grown in optimal conditions. Consequently, several reports on the alloy structure have been misconceived (see Ref. 139 for more details). Secondly, the spatial fine structure as observed by Laplace DLTS involves very strong lattice relaxation effects, which depend strongly on the specific donor atom and the alloy. The DX center is far from the ideal case of an impurity atom sitting stably in a substitutional position in an alloy, where the alloy composition modifies the electronic characteristics. A much simpler case of alloying effects is presented in the following section.

B. Alloys of SiGe

In contrast to the case of the binary alloys, when Si and Ge are mixed to form a SiGe alloy the alloying occurs in every shell of atoms around a defect. Hence, even with only short-range interaction involved, one can expect that more than one shell of atoms influence the level splitting. Considering that both first- and second-shell interactions may be of importance in the elemental alloy the application of LDLTS has enabled a unique detailed mapping of environmental effects on substitution type deep centers in dilute SiGe. The alloy splittings originating from the first and second atomic shell surrounding the impurity are inequivalent. Consequently, investigations of the alloy splitting in binary alloys can be extremely informative provided the experimental technique offers sufficient resolution to discern the features originating these shells.

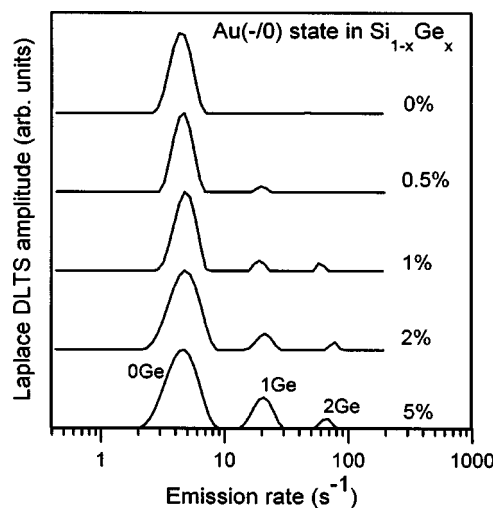


FIG. 42. The Laplace DLTS spectra of gold-diffused samples having different germanium content. For each of the spectra the main lines have been aligned and normalized to the spectrum for the 5% sample (Ref. 59).

1. Indiffused Au and Pt, the alloy splitting effect and siting preference

Using the platinum and gold acceptor states as probes Laplace DLTS spectra obtained for dilute SiGe alloys^{59,141} indeed display a fine structure that can be quantified in terms of alloy splitting. The Au and Pt defects have been studied previously in great detail for the case of pure Si (Refs. 142 and 143) and some conventional DLTS results are available also for SiGe alloys.^{144,145} The samples used in the reviewed LDLTS studies have been grown by molecular-beam epitaxy (MBE) with alloy compositions of the $4\text{ }\mu\text{m}$ thick active $\text{Si}_{1-x}\text{Ge}_x$ layers of 0, 0.5, 1, 2, or 5 at. % with compositionally graded buffer layers inserted between the active layer and the substrate in order to accommodate lattice mismatch strain and reduce the number of misfit dislocations (see Ref. 57 for details of the growth procedure). The dopant metals (either Pt or Au) were diffused into the layers at 800°C for 24 h.

Figures 42 and 43 show LDLTS spectra for the gold and platinum acceptors in the SiGe alloys with 0–5% of Ge, respectively. The spectra have been normalized in terms of the magnitude and emission rate to the line on the left-hand side of the diagram. This enables a direct comparison to be made between the various samples. See Ref. 59 for explanation of the normalization procedure.

When the germanium content in the crystal increases additional features in the Pt- and Au-related Laplace DLTS spectra appear on the high-frequency side of the main line. Clear trends are seen for both impurities which can be associated with different local configurations of the alloy in the vicinity of the metal atom. Figure 44 shows a schematic flat diagram of the random alloy (for 5% of Ge) in the first- and the second-nearest neighborhood of the defect. The light-gray bar diagram represents probabilities of finding the alloy configuration having 0, 1, or 2 out of four germanium atoms (assigned here as 0Ge, 1Ge, and 2Ge, respectively) in the first shell of atoms. When the second shell is taken into account these lines split into subsets, which are depicted by dark-gray bars. The lines in these split sets are marked by

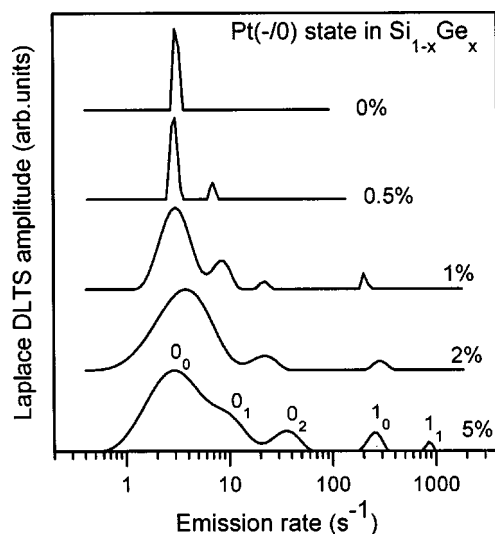


FIG. 43. Laplace DLTS spectra of platinum-diffused samples having different germanium content. For each of the spectra the main lines have been aligned and normalized to the spectrum for the 5% sample (Ref. 59).

figures with subscripts which refer to the number of germanium atoms in the first and second neighborhood, respectively.

For the case of gold a comparison of diagrams with the spectra for the corresponding alloy leads to the conclusion that the spectral structure is a manifestation of the alloying, where only the role of the first-nearest neighbors is visible. In contrast to this, the influence of both the first and second neighbors can be seen for the case of platinum. The peak assignments in Figs. 42 and 43 and in the diagram are the same. Similar bar diagrams constructed for other alloy compositions $\text{Ge} < 5\%$ also reproduce the spectral trends fairly well. For the compositions $5\% < \text{Ge} < 25\%$ the thermal emission becomes less well defined with many contributing features, which makes the numerical procedures for the calculations of the Laplace DLTS spectra unstable and inconclusive as discussed in Sec. II.

The spectra for the gold acceptor depicted in Fig. 42 clearly show that the main 0Ge line broadens with the increase of the alloy composition but never splits into components as observed for the case of platinum. In order to understand this one should remember that the energy resolution of the Laplace DLTS technique is almost inversely proportional to the temperature at which the spectrum is taken (in contrast to conventional DLTS where instrumental broadening dominates). This means that the platinum spectrum (measured at around 100 K) has been obtained with a factor of 2.5 higher emission-rate resolution than the gold spectrum (measured at around 250 K). Hence the additional splitting of the 0Ge line revealed in the platinum case is a result of much better experimental conditions. It can be concluded, however, that in both cases the alloy splitting of the energy level caused by a replacement of one silicon atom among the first-nearest neighbors the impurity is around 35 meV (see Ref. 59 for details). For the case of platinum the similar replacement in the second-nearest neighborhood results in a change in the level energy by 10 meV.

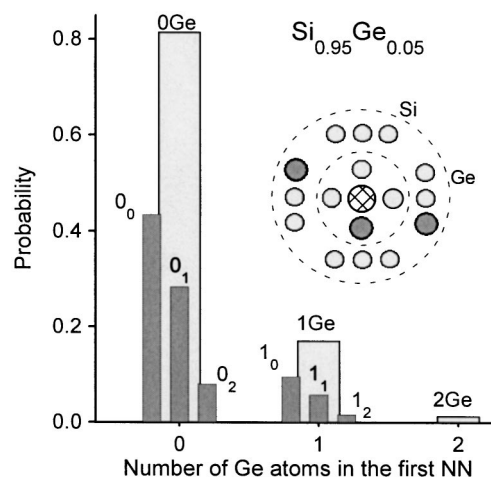


FIG. 44. Flat diagram of the SiGe alloy showing two shells of atoms surrounding the metal impurity. The light gray bar show probabilities of finding a given number of germanium atoms in the first-nearest neighborhood of the metal for the random alloy having 5% of germanium. Those lines split into subsets (dark gray bars) if one assumes that the second-nearest neighborhood plays a role. The component assignment correspond to the ones used in two previous figures (Ref. 59).

While the positions of the peaks on the emission-rate scale indicate how the alloying modifies the electronic properties of the defect, the relative amplitudes of the peaks provide data, which can be interpreted in terms of the concentration of a particular local configuration. These amplitudes, when compared to a model of a perfectly random alloy, demonstrate deviations from a random distribution of the metal impurities in the SiGe lattice.⁴⁴ The general trend is the relative amplitudes of the satellite peaks are somewhat larger than expected for a random alloy^{59,141} and these results indicate that during diffusion at 800°C both metal atoms prefer to occupy sites in the lattice next to germanium. For the case of gold the inferred relative concentration of the 1 Ge configuration is approximately twice as big as would be expected for a random siting. The site preference has been translated⁵⁹ to an estimate of the enthalpy difference between the 0Ge and 1Ge configurations of $\Delta H_{\text{conf}}^{0/1} \approx kT(@800^\circ\text{C})\ln(2) \approx 60$ meV. However for the case of platinum the overpopulation of the germanium-rich sites is seen clearly only for the second-nearest neighbor configuration. For larger alloy compositions the Laplace DLTS peaks are not well separated and consequently, although a general trend is seen, it has not been possible to obtain quantitative results.

The overpopulation of sites close to germanium may be related to details of the microscopic mechanism of the diffusion of impurity metals in silicon. It is well established that Au and Pt diffuse by a kick-out process. The driving force for the accumulation of substitutional Au or Pt is the removal of the self-interstitial atoms by sinks. It is conceivable that the kick-out accumulation proceeds more easily for silicon than for the larger germanium atom. Moreover, it would be expected that due to elastic interactions it is harder to create the pseudo-self-interstitial center (a germanium atom in the silicon host) than the self-interstitial defect (a silicon atom in the silicon host). On the other hand, it is easier for germa-

nium to break the longer and softer Ge-Si bonds during the creation of the pseudo-self interstitial defect, than it is for the corresponding process involving only silicon atoms. The interplay of these competing energy terms during diffusion would then result in a preference for the metal atoms to reside on Si-substitutional sites close to Ge.

2. Bond-centered hydrogen: Trapping in local strain

It has been shown that slightly modified and thermally stabilized versions of bond-center (BC) hydrogen can form in the vicinity of grown-in impurities in silicon such as oxygen and carbon.^{47,121,122} This tendency of hydrogen to become trapped in local strain fields of the crystal with only minor changes in the electrical properties as compared to the BC structure appears to be a rather general feature. The strain causes elongation of some Si-Si bonds (and compression of others) with the consequence that hydrogen atoms are most easily incorporated in the elongated bonds. A dilute SiGe alloy forms a system in which randomly distributed internal strain is imposed on the Si lattice in order to accommodate the incorporation of Ge atoms. This strain can play a role similar to that of the local strain in elemental silicon introduced by a carbon or an oxygen impurity. The results for elemental Si indicate that the elongation of some of the Si-Si bonds in the neighborhood of interstitial oxygen or carbon aids the outward relaxation that hydrogen needs to enter the BC-site, and therefore promotes the incorporation of hydrogen into these strained bonds. In this section we review a LDLTS study¹⁴⁶ that has demonstrated this promotion effect for the case of the SiGe alloy and lead to characterization of a Ge-strained bond-center defect, which is geometrically analogous to the C-strained bond-center defect (C-H)_I described in Ref. 47 and mentioned previously in this paper.

The results presented in Ref. 146 were obtained on samples cut and polished from a float-zone (FZ) Si_{1-x}Ge_x phosphorus doped bulk crystal with the Ge fraction $x = 0.008$ measured by secondary ion mass spectroscopy furnished with Schottky diodes and on samples prepared from as-grown Czochralski Si_{1-x}Ge_x with $x = 0.013$. As reference samples diodes made on 100 Ω cm FZ, 50 Ω cm Czochralski grown (Cz), and carbon-rich 20 Ω cm FZ silicon (C-FZ) were used. The diode structures were implanted with protons (or helium ions to provide control samples) at a temperature of 60 K with the peak of the implants close to the edge of the reverse-bias depletion width in order to minimize the electric field at the sites of the implants.

Figure 45 reproduced from Ref. 146 depicts the Laplace DLTS spectra obtained *in situ* at 86 K after implanting hydrogen at 60 K into short-circuited diodes at a dose of $\sim 10^9$ cm⁻². Prior to the implantation no signal is present in the displayed emission-rate range. The spectrum for the FZ SiGe alloy is compared to a spectrum obtained for a reference diode made from a commercial FZ Si wafer material implanted at the same temperature and measured so that the electric field at the implantation range is about the same in the two cases. No significant peaks other than those shown appear in the emission-rate range $0.05\text{--}5 \times 10^3$ s⁻¹ between 60 and 87 K. The reference spectra from the silicon samples

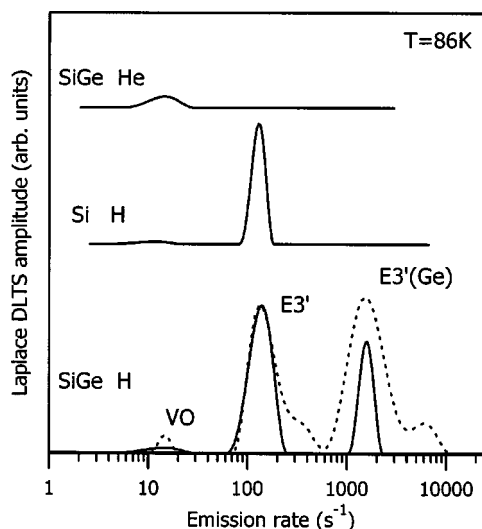


FIG. 45. Laplace DLTS spectrum measured *in situ* after implantation of hydrogen at 60 K into short circuited Schottky diodes made on FZ *n*-type SiGe alloy (0.8% Ge) reveal two donor signals E3' and E3'(Ge). Comparison with analogously H-implanted Si and He-implanted SiGe establish that E3' (Ge) originates from a hydrogen defect associated with germanium. The overlaid SiGe spectrum is obtained with Cz material (1.3% Ge) and has been normalized to E3' signal of the FZ material. The small satellites of the main peaks can be ascribed to the presence of oxygen in the Cz sample (Ref. 146).

reveal the center known as E3' in the literature¹⁴⁷ which has been ascribed previously to hydrogen at the regular bond-center site.^{118,121} Apart from a shift in emission rate due to field dependence an identical reference spectrum was taken with Si grown in the same reactor as the alloy sample. As depicted, the E3' signal is present also in the spectra from the proton-implanted SiGe together with a satellite signal denoted E3'(Ge). The reference spectrum obtained with a SiGe sample implanted with helium shows no trace of the E3' signals but does reveal the A-center signal (VO) also seen in the hydrogen-implanted samples. This demonstrates that both SiGe signals are indeed hydrogen related. Together they account for the majority ($\geq 70\%$) of the implanted protons and in accordance with previous results for pure silicon^{121,122} the remaining implants are most likely hidden in the form of negatively charged hydrogen at the tetrahedral *T* sites. The E3'(Ge) signal is about a factor 12.5 stronger than expected for a pure statistical population of Si-H-Si bond-center sites next to the Ge atoms of the alloy. The same overpopulation factor is obtained with the Cz sample containing 1.3% Ge (see the dashed overlay in Fig. 45). During annealing both E3' centers convert (for the carbon rich and oxygen lean material used) to a carbon-related bond-center defect Si-H-C identical to the (C-H)_{II} center mentioned earlier in this paper.

We summarize the interpretation and conclusions of Ref. 146, which we refer to for further details. The E3'(Ge) center is interpreted as a Si-H-Si bond-center defect sited next to an alloy Ge atom and a configuration diagram for this Ge perturbed bond-center structure is constructed. This construction relies upon the comparison of annealing-, emission-, and formation rates of the E3' and E3'(Ge) centers. It is particularly interesting to notice the sizable over-

population, which demonstrates that ultra fast migration of the implants occurs in the final stage of thermalization and allows hydrogen to become trapped near Ge. The result that the Si-H-C defect and not the analog Si-H-Ge defect forms during annealing shows that the latter defect is less stable or nonexistent. The configuration potentials of the Ge-strained structure are remarkably close to those of isolated hydrogen in elemental silicon. This indicates that hydrogen migration is only moderately affected by dilute alloying with germanium, consistent with the additional result that hydrogen interacts with carbon impurities during migration in much the same way as in elemental silicon. During this migration at low temperature a carbon analog to Ge-perturbed bond-center hydrogen forms. In the sequence Ge, Si, C the variation of the Group IV element at the neighbor site of the Si-H-Si bond center causes the donor level to deepen and the stability of the defect (in its neutral charge state) to increase.

VI. SUMMARY AND OUTLOOK

Under ideal experimental conditions Laplace DLTS provides an order of magnitude higher energy resolution than conventional DLTS techniques. A prime requirement for achieving this resolution is an excellent signal-to-noise ratio. In practice this limits the application of the measurement to cases where a significant concentration of the defect is present in the semiconductor. The ideal case is that where the defect to be studied has a concentration of between 5×10^{-4} and 5×10^{-2} of the shallow donor or acceptor concentration. However given these limitations, Laplace DLTS enables a range of measurements to be undertaken which are not practicable in any other system. In this paper we have discussed several cases that illustrate such applications of Laplace DLTS.

Perhaps the most obvious is the separation of defects which have very similar carrier emission rates. A good example of this is the separation of the gold acceptor and the acceptor level of the hydrogen-gold complex in silicon known as G4. In conventional DLTS a combination of these two states appears as a single peak near room temperature with undetectable broadening. Using Laplace DLTS at similar temperatures the emission from the two states is clearly separated with a difference of 16 meV. This example shows very clearly that even at room temperature the thermal broadening is insignificant compared to the instrumental broadening of conventional DLTS.

Laplace DLTS removes the instrumental broadening completely and hence line broadening in LDLTS is a measure of electronic or physical processes in the semiconductor. In consequence LDLTS provides a much more incisive probe into the physics of defects than is possible with the conventional technique. An example of this is the study of impurities in binary alloys. By examining gold in silicon germanium with Laplace DLTS it is possible to distinguish the electron emission from a gold acceptor surrounded by four silicon atoms from a gold atom surrounded by three silicons and a germanium atom. The energy difference in the electron binding is 35 meV. If another silicon atom is replaced by germanium a similar energy difference is noted.

An important attribute of the Laplace technique is that it is absolutely quantitative and so, in this way, the population of an impurity with specific nearest-neighbour configurations can be measured and compared with the statistically expected distribution. In the SiGe: Au case there are significant differences between the measured and expected values indicating that gold has a strong preference for a Ge rich environment. Using these data it is possible to determine the enthalpy difference between 0 and 1 Ge configurations. If the case of platinum in SiGe is considered the binding energy of the electron is smaller than that for gold and so measurement can be conducted at lower temperatures. In this case it is possible not only to see the effect of replacing silicon by germanium in the first-nearest-neighbour shell but also in the second-nearest neighbour. The difference for the first-nearest neighbour is as in the gold case 35 meV, whereas replacement of the second-nearest neighbour is 10 meV. The ability to quantify these issues and to perform spatial profiles (hence determining the impact of the proximity of surfaces and interfaces on siting) provides a unique tool for device research and process engineering. As this is a relatively simple measurement we envisage its wide application to defect and impurity studies over the next decade.

However, perhaps the most dramatic demonstration of the techniques power is when it is used in conjunction with uniaxial stress. Examples have been given in this paper where the symmetry of defects can be determined from the splitting patterns and the magnitudes of the various components. This is a much more complex and tedious measurement compared to the examples discussed above and necessitates the preparation of sample sets of different orientations. The classic study which we discussed at length in this paper is that of the vacancy-oxygen pair in silicon. This is a very good starting point for such measurements because it has been extensively studied by EPR and the characteristics of the defect are well known. However, a very significant difference is that the Laplace DLTS measurement can be performed in extremely thin regions of the semiconductor, such as a shallow ion implantation where it would be very difficult or perhaps even impossible to undertake such as study by other techniques.

In some cases the defect reorients itself under the application of uniaxial stress. If this occurs at the measurement temperature the interpretation of the results is fraught with difficulty but, in the case of VO reorientation, this occurs conveniently somewhat above the measurement temperature but in an easily accessible temperature range. In this way the reorientation of the defect can be observed by cycling the sample rapidly between the reorientation and the measurement temperature. This has been done previously for VO in the negative charged state using EPR and the Laplace DLTS results agree quite precisely. However, it is only possible to study the negative (paramagnetic) charged state using EPR. In general Laplace DLTS can also be used to study states with no magnetic activity and it has been found that the reorientation of the neutral state is about two orders of magnitude faster than the negative state.

This technique has very considerable potential in the general case in providing information about the migration

and diffusion of atomic species in semiconductors at low temperatures, which is very difficult or even impossible to determine by other methods.

Much more information about the actual structure of a defect can be obtained from piezoscopic measurements apart from the symmetry. Again in this paper there are a number of examples of this, where detailed piezospectroscopic analysis of the experimental split patterns and the magnitudes of the tensors are compared with theoretical modeling. A good example of this is discussed in the paper in relation to the reaction of hydrogen with substitutional carbon in silicon. This study involved proton implantation and *in situ* Laplace DLTS measurements. As a result the sequence of reactions leading to the formation of the carbon-hydrogen complex could be tracked.

There are a number of physical processes which lead to defect parameter homogeneous broadening effects. The main ones are local strains and electric fields. Some preliminary analysis of the latter has been demonstrated in Ref. 79. Another example of parameter broadening are defects at interfaces where defect bands are observed with a broad carrier emission parameter distribution on which are superimposed structure arising from well-defined states. In principle, the elimination of instrumental broadening in Laplace DLTS enables these effects to be investigated systematically. However it is known that application of LDLTS to the above cases is a difficult task as the Tikhonov regularization method is not as effective for them as it is for narrow lines. However, some preliminary tests with the numerical routines showed that they can be separately optimized to cope with these "broad" cases more effectively, especially where there are more peaks on the spectrum. As yet the broadening effects have not been systematically explored by the method but it is believed that they can be of particular interest when the LDLTS peak broadening is a meaningful physical defect parameter. This is particularly important when point defects are observed in very small electronic devices i.e., in an environment far from the idealized surrounding of a bulk crystal.

Finally, the Laplace-transform method of transient analysis can be applied to other experimental techniques where one deals with nonstationary processes in general. Among these are photoinduced transient spectroscopy,¹⁴⁸ photoluminescence, optical absorption, magnetic resonance decay, etc. However, it seems that in these cases besides the ability to distinguish close transient time constants, real progress in probing the physics can be made if the Laplace-transform method is able to quantify homogeneous time constant broadening effects.

In this paper we have considered a number of examples of semiconductor systems in which LDLTS has been able to provide information about the physical processes associated with defects in semiconductors. It is evident that there are many other cases where the existing technique can extend our knowledge of new and existing material systems for the advantage of the device community. Overall it seems likely that the technique of LDLTS will deliver an important new tool into the hands of semiconductor physicists and technologists which will bear fruit over the next decade.

ACKNOWLEDGMENTS

The authors would like Dr. I. D. Hawkins of UMIST Manchester and K. Gościński of IoP Warsaw, their dedicated work has been central to the development of the Laplace DLTS system. They would also like to thank members of the Copernicus team for their implementations of the Laplace transform, in particular, Professor J. Honerkamp, Dr. D. Maier, and Dr. J. Winterhalter (Freiburg), Professor A. Matulis, and Dr. Z. Kancleris (Vilnius). The interpretation of LDLTS, particularly when used in conjunction with stress, has been helped by input from many scientists in the field but, in particular, they would like to mention Professor R. Jones (Exeter) and his team. The work was funded by the European Community Grant No. CIPA-CT94-0172 in the UK by the Engineering and Science Research Council and the Royal Academy of Engineering, in Poland by the Committee for Scientific Research Grant No. 4T11B02123 and in Denmark by the Danish National Research Foundation through the Aarhus Center for Atomic Physics. Finally, they express their gratitude for the comments and suggestions that the many visitors to their laboratories had made while undertaking measurements with LDLTS and which have enabled them to make its practical implementation much more usable by the scientific community as a whole.

- ¹C. T. Sah, L. Forbes, L. L. Rosier, and A. F. Tasch, Jr., *Solid-State Electron.* **13**, 759 (1970).
- ²W. Shockley and W. T. Read, Jr., *Phys. Rev.* **87**, 835 (1952); S. M. Sze, *Physics of Semiconductor Devices* (Wiley, New York, 1969).
- ³C. H. Henry and D. V. Lang, *Phys. Rev. B* **15**, 989 (1977).
- ⁴P. Blood and J. W. Orton, *The Electrical Characterization of Semiconductors: Majority Carriers and Electron States* (Academic, London, 1992), pp. 596–648.
- ⁵D. V. Lang, *J. Appl. Phys.* **45**, 3023 (1974).
- ⁶G. L. Miller, J. V. Ramirez, and D. A. H. Robinson, *J. Appl. Phys.* **46**, 2638 (1975).
- ⁷D. S. Day, M. Y. Tsai, and B. G. Streetman, *J. Appl. Phys.* **50**, 5093 (1979).
- ⁸F. D. Auret, *Rev. Sci. Instrum.* **57**, 1597 (1986).
- ⁹J. A. Borsuck and R. M. Swanson, *IEEE Trans. Electron Devices* **27**, 2217 (1980).
- ¹⁰C. R. Crowell and S. Aliphani, *Solid-State Electron.* **24**, 25 (1981).
- ¹¹A. A. Istratov, *J. Appl. Phys.* **82**, 2965 (1997).
- ¹²G. Vincent, A. Chantre, and D. Bois, *J. Appl. Phys.* **50**, 5484 (1979).
- ¹³K. Ikossi-Anastasiou and K. P. Roenker, *J. Appl. Phys.* **61**, 182 (1987).
- ¹⁴D. D. Nolte and E. E. Haller, *J. Appl. Phys.* **62**, 900 (1987).
- ¹⁵C. Eiche, D. Maier, M. Schneider, D. Sinerius, J. Weese, K. W. Benz, and J. Honerkamp, *J. Phys.: Condens. Matter* **4**, 6131 (1992).
- ¹⁶A. A. Istratov and O. F. Vyvenko, *Rev. Sci. Instrum.* **70**, 1233 (1999).
- ¹⁷S. Misrachi, A. R. Peaker, and B. Hamilton, *J. Phys. E* **13**, 1055 (1980).
- ¹⁸N. Ostrowsky, D. Sornette, P. Parker, and E. R. Pike, *Opt. Acta* **28**, 1059 (1981).
- ¹⁹M. Bertero, P. Boccacci, and E. R. Pike, *Proc. R. Soc. London, Ser. A* **383**, 15 (1982).
- ²⁰C. W. Groetsch, *The Theory of Tikhonov Regularisation for Fredholm Equations of the First Kind* (Pitman, London, 1984).
- ²¹S. W. Provencher, *Comput. Phys. Commun.* **27**, 213 (1982).
- ²²The Computer Physics Communication (CPC) Program Library at the Queen's University of Belfast (<http://www.cps.cs.qub.ac.uk>).
- ²³J. Weese, *Comput. Phys. Commun.* **69**, 99 (1991); *ibid.* **77**, 429 (1993).
- ²⁴A. Matulis (unpublished).
- ²⁵Z. Kancleris (unpublished).
- ²⁶K. Tittelbach-Helmrich, *Meas. Sci. Technol.* **4**, 1323 (1993).
- ²⁷L. Dobaczewski, P. Kaczor, I. D. Hawkins, and A. R. Peaker, *J. Appl. Phys.* **76**, 194 (1994).
- ²⁸J. W. Chen and A. G. Milnes, in *Annual Review of Material Science*, edited by R. A. Huggins, R. H. Bube, and D. A. Vermilyea (Annual Re-

- views, Palo Alto, 1980), Vol. 10, p. 157.
- ²⁹A. G. Milnes, in *Advances in Electronics and Electron Physics*, edited by P. W. Hawkes (Academic, Orlando, 1983), Vol. 61, p. 63.
 - ³⁰G. M. Martin, A. Mitonneau, and A. Mircea, *Electron. Lett.* **13**, 191 (1977).
 - ³¹A. Mitonneau, G. M. Martin, and A. Mircea, *Electron. Lett.* **13**, 666 (1977).
 - ³²N. M. Johnson, C. Doland, F. Ponce, J. Walker, and G. Anderson, *Physica B* **170**, 3 (1991).
 - ³³*Hydrogen in Silicon, Semiconductors and Semimetals*, Vol. 34, edited by J. I. Pankove and N. M. Johnson (Academic, San Diego, 1991).
 - ³⁴E. Ö. Sveinbjörnsson and O. Engström, *Phys. Rev. B* **52**, 4884 (1995).
 - ³⁵J. A. Davidson and J. H. Evans, *Semicond. Sci. Technol.* **11**, 1704 (1996).
 - ³⁶A. Resende, J. Goss, P. R. Briddon, S. Öberg, and R. Jones, *Mater. Sci. Forum* **258-263**, 295 (1997).
 - ³⁷P. Deixler *et al.*, *Appl. Phys. Lett.* **73**, 3126 (1998).
 - ³⁸R. H. Wu and A. R. Peaker, *Solid-State Electron.* **25**, 643 (1982).
 - ³⁹S. D. Brotherton and J. Bicknell, *J. Appl. Phys.* **49**, 667 (1978).
 - ⁴⁰A. Mesli, E. Courcelle, T. Zundel, and P. Siffert, *Phys. Rev. B* **36**, 8049 (1987).
 - ⁴¹D. V. Lang, H. C. Grimmeiss, E. Meijer and M. Jaros, *Phys. Rev. B* **22**, 3917 (1980).
 - ⁴²B. Bech Nielsen, P. Johannesen, P. Stallings, K. Bonde Nielsen, and J. R. Byberg, *Phys. Rev. Lett.* **79**, 1507 (1997).
 - ⁴³P. Stallings, P. Johannesen, S. Herström, K. Bonde Nielsen, B. Bech Nielsen, and J. R. Byberg, *Phys. Rev. B* **58**, 3842 (1998).
 - ⁴⁴K. Bonde Nielsen, L. Dobaczewski, K. Gościński, R. Bendesen, O. Andersen, and B. Bech Nielsen, *Physica B* **273-274**, 167 (1999).
 - ⁴⁵O. Andersen, Ph. D. thesis, University of Manchester Institute of Science and Technology, Manchester, UK, 2003.
 - ⁴⁶L. Dobaczewski, K. Bonde Nielsen, A. Mesli, and A. Nylandsted Larsen (unpublished).
 - ⁴⁷O. Andersen, A. R. Peaker, L. Dobaczewski, K. Bonde Nielsen, B. Hourahine, R. Jones, P. R. Briddon, and S. Öberg, *Phys. Rev. B* **66**, 235205 (2002).
 - ⁴⁸V. P. Markevich, A. R. Peaker, S. B. Lastovskii, L. I. Murin, and J. L. Lindström, *J. Phys.: Condens. Matter* **15**, S2779 (2003).
 - ⁴⁹B. Hamilton, A. R. Peaker, and D. R. Wight, *J. Appl. Phys.* **50**, 6373 (1979).
 - ⁵⁰R. Brunwin, B. Hamilton, P. Jordan, and A. R. Peaker, *Electron. Lett.* **15**, 349 (1979).
 - ⁵¹P. Deixler (private communication).
 - ⁵²M. A. Gad and J. H. Evans-Freeman, *J. Appl. Phys.* **92**, 5252 (2002).
 - ⁵³Y. Shreter, J. H. Evans, B. Hamilton, A. R. Peaker, C. Hill, D. R. Boys, C. D. Meekison, and G. R. Booker, *Appl. Surf. Sci.* **63**, 227 (1993).
 - ⁵⁴S. Solmi, M. Bersani, M. Sbeti, J. Lundsgaard Hansen, and A. Nylandsted Larsen, *J. Appl. Phys.* **88**, 4547 (2000).
 - ⁵⁵N. Abdelgader and J. H. Evans-Freeman, *J. Appl. Phys.* **93**, 5118 (2003).
 - ⁵⁶E. Anastassakis and M. Cardona, *Semicond. Semimetals* **55**, 117 (1998).
 - ⁵⁷A. Nylandsted Larsen, *Mater. Sci. Forum* **258-263**, 83 (1997).
 - ⁵⁸K. Gościński, L. Dobaczewski, K. Bonde Nielsen, and A. Nylandsted Larsen (unpublished).
 - ⁵⁹K. Gościński, L. Dobaczewski, K. Bonde Nielsen, A. Nylandsted Larsen, and A. R. Peaker, *Phys. Rev. B* **63**, 235309 (2001).
 - ⁶⁰G. A. Samara and C. E. Barnes, *Phys. Rev. B* **35**, 7575 (1987).
 - ⁶¹J. F. Nye, *Physical Properties of Crystals, Their Representation by Tensor and Matrices* (Clarendon, Oxford, 1957).
 - ⁶²L. Dobaczewski, A. Mesli, K. Bonde Nielsen, and A. Nylandsted Larsen (unpublished).
 - ⁶³G. E. Jellison, *J. Appl. Phys.* **53**, 5715 (1982).
 - ⁶⁴L. W. Song, X. D. Zhan, B. W. Benson, and G. D. Watkins, *Phys. Rev. B* **42**, 5765 (1990).
 - ⁶⁵T. P. Leervad Pedersen, A. Nylandsted Larsen, and A. Mesli, *Appl. Phys. Lett.* **75**, 4085 (1990).
 - ⁶⁶J. Frenkel, *Phys. Rev.* **54**, 647 (1938).
 - ⁶⁷J. L. Hartke, *J. Appl. Phys.* **39**, 4871 (1968).
 - ⁶⁸P. A. Martin, B. G. Streetman, and K. Hess, *J. Appl. Phys.* **52**, 7409 (1981).
 - ⁶⁹S. D. Ganichev, E. Ziemann, W. Prettl, I. N. Yassievich, A. A. Istratov, and E. R. Weber, *Phys. Rev. B* **61**, 10361 (2000).
 - ⁷⁰I. Izpura, E. Munoz, F. Garcia, E. Calleja, A. L. Powell, P. I. Rockett, C. C. Button, and J. S. Roberts, *Appl. Phys. Lett.* **58**, 735 (1991).
 - ⁷¹S. Makram-Ebeid and M. Lannoo, *Phys. Rev. Lett.* **48**, 1281 (1982); *Phys. Rev. B* **25**, 6406 (1982).
 - ⁷²R. D. Harris, J. L. Newton, and G. D. Watkins, *Phys. Rev. B* **36**, 1094 (1987).
 - ⁷³F. D. Aurret and L. Dobaczewski (unpublished).
 - ⁷⁴F. D. Aurret, R. M. Erasmus, S. A. Goodman, and W. E. Meyer, *Phys. Rev. B* **51**, 17521 (1995).
 - ⁷⁵W. E. Meyer, F. D. Aurret, and S. A. Goodman, *Jpn. J. Appl. Phys., Part 2* **35**, L1 (1996).
 - ⁷⁶J. Lagowski, D. G. Lin, H. C. Gatos, J. M. Parsey, Jr., and M. Kaminska, *Appl. Phys. Lett.* **45**, 89 (1984).
 - ⁷⁷L. Dobaczewski, *Mater. Sci. Forum* **38-41**, 113 (1988).
 - ⁷⁸L. Dobaczewski, K. Bonde Nielsen, N. Zangenberg, B. Bech Nielsen, A. R. Peaker, and V. Markevich, *Phys. Rev. B* **70**, 079901 (2004).
 - ⁷⁹K. Bonde Nielsen and L. Dobaczewski, *Mater. Sci. Forum* **258-263**, 331 (1997).
 - ⁸⁰J. A. van Vechten and C. D. Thurmond, *Phys. Rev. B* **14**, 3539 (1976).
 - ⁸¹O. Engström and A. Alm, *Solid-State Electron.* **21**, 1571 (1978).
 - ⁸²A. K. Ramdas and S. Rodrigues, *Semicond. Semimetals* **36**, 137 (1992).
 - ⁸³A. A. Kaplyanskii, *Opt. Spectrosc.* **16**, 329 (1964).
 - ⁸⁴G. D. Watkins and J. W. Corbett, *Phys. Rev.* **121**, 1001 (1961).
 - ⁸⁵J. W. Corbett, G. D. Watkins, R. M. Chernko, and R. S. McDonald, *Phys. Rev.* **121**, 1015 (1961).
 - ⁸⁶G. A. Samara, *Phys. Rev. B* **36**, 4841 (1987).
 - ⁸⁷J. M. Meese, J. W. Farmer, and G. D. Lamp, *Phys. Rev. Lett.* **51**, 1286 (1983).
 - ⁸⁸L. Dobaczewski, O. Andersen, L. Rubaldo, K. Gościński, V. P. Markevich, A. R. Peaker, and K. Bonde Nielsen, *Phys. Rev. B* **67**, 195204 (2003).
 - ⁸⁹B. K. Ridley, *J. Phys. C* **11**, 2323 (1978).
 - ⁹⁰D. D. Nolte and E. E. Haller, *Phys. Rev. B* **38**, 9857 (1988).
 - ⁹¹W. Jantsch, K. Wünnstall, O. Kumagai, and P. Vogl, *Phys. Rev. B* **25**, 5515 (1982).
 - ⁹²G. A. Samara and C. E. Barnes, *Phys. Rev. Lett.* **57**, 2069 (1986).
 - ⁹³W. W. Keller, *J. Appl. Phys.* **55**, 3471 (1984).
 - ⁹⁴M. Li, J. Chen, Y. Yao, and G. Bai, *J. Appl. Phys.* **58**, 2599 (1985).
 - ⁹⁵W. Stöffer and J. Weber, *Phys. Rev. B* **33**, 8892 (1986).
 - ⁹⁶D. D. Nolte, W. Walukiewicz, and E. E. Haller, *Phys. Rev. Lett.* **59**, 501 (1987).
 - ⁹⁷M. J. Caldas, A. Fazzio, and A. Zunger, *Appl. Phys. Lett.* **45**, 671 (1984).
 - ⁹⁸J. M. Langer and H. Heinrich, *Phys. Rev. Lett.* **55**, 1414 (1985).
 - ⁹⁹C. G. Van de Walle and R. M. Martin, *Phys. Rev. B* **35**, 8154 (1987).
 - ¹⁰⁰M. Hamera, W. Walukiewicz, D. D. Nolte, and E. E. Haller, *Phys. Rev. B* **39**, 10114 (1989).
 - ¹⁰¹D. D. Nolte, W. Walukiewicz, and E. E. Haller, *Phys. Rev. B* **36**, 9374 (1987).
 - ¹⁰²D. E. Bliss, D. D. Nolte, W. Walukiewicz, and E. E. Haller, *Appl. Phys. Lett.* **56**, 1143 (1990).
 - ¹⁰³L. Dobaczewski and A. Sienkiewicz, *Acta Phys. Pol. A* **71**, 341 (1987).
 - ¹⁰⁴P. Dreszner and M. Baj, *Acta Phys. Pol. A* **73**, 219 (1987).
 - ¹⁰⁵H. Hasagawa, *Phys. Rev.* **129**, 1029 (1963).
 - ¹⁰⁶I. Balslev, *Phys. Rev.* **143**, 636 (1966).
 - ¹⁰⁷L. L. Laude, F. H. Pollak, and M. Cardona, *Phys. Rev. B* **3**, 2623 (1971).
 - ¹⁰⁸X.-C. Yao, J. X. Mou, and G.-G. Qin, *Phys. Rev. B* **35**, 5734 (1987).
 - ¹⁰⁹J.-X. Mou, X.-C. Yao, and G.-G. Qin, *Mater. Sci. Forum* **10-12**, 481 (1986).
 - ¹¹⁰P. M. Henry, J. W. Farmer, and J. M. Meese, *Appl. Phys. Lett.* **45**, 454 (1984).
 - ¹¹¹L. C. Kimerling, in *Oxygen, Carbon, Hydrogen, and Nitrogen in Crystalline Silicon*, edited by J. C. Mikkelsen, Jr., S. J. Pearton, J. W. Corbett, and J. C. Pennycook (Materials Research Society, Pittsburgh, 1986), p. 83.
 - ¹¹²M. Stavola, *Physica B & C* **146**, 187 (1987).
 - ¹¹³P. Wagner, H. Gottschalk, J. Trombetta, and G. D. Watkins, *J. Appl. Phys.* **61**, 346 (1987).
 - ¹¹⁴M. Stavola, in *Early Stages of Oxygen Precipitation in Silicon, Advanced Studies Institute, Series C: Mathematical and Physical Sciences, NATO* edited by R. Jones (Kluwer Academic Publishers, Dordrecht, 1996) Vol. 17, p. 223.
 - ¹¹⁵S. J. Hartnett and D. W. Palmer, *Mater. Sci. Forum* **258-263**, 1027 (1997).
 - ¹¹⁶D. Pons, P. M. Mooney, and J. C. Bourgoin, *J. Appl. Phys.* **51**, 2038 (1980); D. Stievenard, X. Boddaert, J. C. Bourgoin, and H. J. von Bardeleben, *Phys. Rev. B* **41**, 5271 (1990).
 - ¹¹⁷S. Yang and C. D. Lamp, *Phys. Rev. B* **49**, 1690 (1994).
 - ¹¹⁸B. Holm, K. Bonde Nielsen, and B. Bech Nielsen, *Phys. Rev. Lett.* **66**, 2360 (1991).

- ¹¹⁹Y. V. Gorelkinskii and N. N. Nevynnyi, Sov. Tech. Phys. Lett. **13**, 45 (1987); Physica B **170**, 155 (1991).
- ¹²⁰B. Bech Nielsen, K. Bonde Nielsen, and J. R. Byberg, Mater. Sci. Forum **143-147**, 909 (1994).
- ¹²¹K. Bonde Nielsen, B. Bech Nielsen, J. Hansen, E. Andersen, and J. U. Andersen, Phys. Rev. B **60**, 1716 (1999).
- ¹²²K. Bonde Nielsen, L. Dobaczewski, S. Søgård, and B. Bech Nielsen, Physica B **308-310**, 134 (2001); Phys. Rev. B **65**, 075205 (2002).
- ¹²³C. Herring, N. M. Johnson, and C. G. Van de Walle, Phys. Rev. B **64**, 125209 (2001).
- ¹²⁴A. Endrös, Phys. Rev. Lett. **63**, 70 (1989).
- ¹²⁵Y. Kamiura, M. Yoneta, Y. Nishiyama, and F. Hashimoto, J. Appl. Phys. **72**, 3394 (1992).
- ¹²⁶Y. Kamiura, N. Ishiga, and Y. Yamashita, Jpn. J. Appl. Phys., Part 1 **36**, L1419 (1997).
- ¹²⁷K. Fukuda, Y. Kamiura, and Y. Yamashita, Physica B **273-274**, 184 (1999).
- ¹²⁸Y. Kamiura, K. Fukuda, Y. Yamashita, and T. Ishiyama, Phys. Rev. B **65**, 113205 (2002).
- ¹²⁹O. Andersen, L. Dobaczewski, A. R. Peaker, K. Bonde Nielsen, B. Hourahine, R. Jones, P. R. Briddon, and S. Öberg, Physica B **308-310**, 139 (2001).
- ¹³⁰J. Coutinho, O. Andersen, L. Dobaczewski, K. Bonde Nielsen, A. R. Peaker, R. Jones, S. Öberg, and P. Briddon, Phys. Rev. B **68**, 184106 (2003).
- ¹³¹P. Johannesen, B. Bech Nielsen, and J. R. Byberg, Phys. Rev. B **61**, 4659 (2000).
- ¹³²J. Coutinho, R. Jones, P. Briddon, and S. Öberg, Phys. Rev. B **62**, 10824 (2000).
- ¹³³L. Dobaczewski, K. Bonde Nielsen, O. Andersen, L. Rubaldo, K. Gościński, and A. R. Peaker, in *Proceedings of the 25th Conference on the Physics of Semiconductors*, edited by N. Miura and T. Ando (Springer Proceedings in Physics, New York, 2001), p. 1427.
- ¹³⁴G. D. Watkins and J. W. Corbett, Phys. Rev. **138**, A543 (1965).
- ¹³⁵M. Stavola and L. C. Kimerling, J. Appl. Phys. **54**, 3897 (1983).
- ¹³⁶L. Dobaczewski, K. Gościński, Z. R. Zykwicz, K. Bonde Nielsen, L. Rubaldo, O. Andersen, and A. R. Peaker, Phys. Rev. B **65**, 113203 (2002).
- ¹³⁷See the review article, P. M. Mooney, J. Appl. Phys. **67**, R1 (1990).
- ¹³⁸L. Dobaczewski, P. Kaczor, M. Missous, A. R. Peaker, and Z. R. Zytewicz, Phys. Rev. Lett. **68**, 2508 (1992).
- ¹³⁹L. Dobaczewski, P. Kaczor, M. Missous, A. R. Peaker, and Z. R. Zytewicz, J. Appl. Phys. **78**, 2468 (1995).
- ¹⁴⁰D. J. Chadi and K. J. Chang, Phys. Rev. Lett. **61**, 873 (1988); Phys. Rev. B **39**, 10063 (1989).
- ¹⁴¹L. Dobaczewski, K. Gościński, K. Bonde Nielsen, A. Nylandsted Larsen, J. Lundsgaard Hansen, and A. R. Peaker, Phys. Rev. Lett. **83**, 4582 (1999).
- ¹⁴²G. D. Watkins, M. Kleverman, A. Thilderkvist, and H. G. Grimmeiss, Phys. Rev. Lett. **67**, 1149 (1991).
- ¹⁴³F. G. Anderson, R. F. Milligan, and G. D. Watkins, Phys. Rev. B **45**, 3279 (1992).
- ¹⁴⁴F. Nikolajsen, P. Kringhøj, and A. Nylandsted Larsen, Appl. Phys. Lett. **69**, 1743 (1996).
- ¹⁴⁵A. Mesli and A. Nylandsted Larsen, Mater. Res. Soc. Symp. Proc. **510**, 89 (1989).
- ¹⁴⁶K. Bonde Nielsen, L. Dobaczewski, A. R. Peaker, and N. V. Abrosimov, Phys. Rev. B **68**, 045204 (2003).
- ¹⁴⁷K. Irmsher, H. Klose, and K. Maass, J. Phys. C **17**, 6317 (1984).
- ¹⁴⁸C. Hurtes, M. Boulou, A. Mitonneau, and D. Bois, Appl. Phys. Lett. **32**, 821 (1978).